X-RAY DICHROISM
OF
RARE EARTH MATERIALS

Jeroen Goedkoop

X-RAY DICHROISM
OF
RARE EARTH MATERIALS

X-RAY DICHROISM
OF
RARE EARTH MATERIALS

Een wetenschappelijke proeve op het gebied van de

NATUURWETENSCHAPPEN

Proefschrift

ter verkrijging van de graad van doctor
aan de Katholieke Universiteit te Nijmegen,
volgens besluit van het College van Decanen
in het openbaar te verdedigen op
maandag 11 december 1989
des namiddags te 3.30 uur

door

Jeroen Björn Goedkoop
geboren op 28 februari 1959 te Oslo

Druk : Krips Repro, Meppel

1989

Promotor: Prof. Dr. J.C. Fuggle, MSc.

Co-promotor: Prof. Dr. G.A. Sawatzky

This investigation was supported by the Netherlands Foundation for Chemical Research **SON** with financial aid from the Netherlands Organisation for the Advancement of Research **NWO**.

ISBN 90-9003127-8

Voor mijn ouders
Voor Dieuke en Maaike

Contents

1 INTRODUCTION 7

1.1 Scope of the work 9

2 X-RAY ABSORPTION AND X-RAY DICHROISM: A PERSPECTIVE 12

2.1 Introduction 12

2.2 Generation of Polarized X-rays 12

2.3 X-ray Absorption Spectroscopy (XAS) 13

2.3.1 Nomenclature 15

2.3.2 The core-hole spin-orbit splitting 16

2.3.3 Golden Rule description 17

2.3.4 *N*-particle description 19

2.4 Polarization Phenomena in the Visible 20

2.4.1 Magnetic Circular Dichroism 23

2.5 X-ray Polarization Effects in Solids 25

2.5.1 Anomalous x-ray scattering and birefringence 25

2.6 X-ray Dichroism 27

2.6.1 3d-Magnetic X-ray Dichroism 27

2.6.2 Crystal field effects 29

2.7 Review of X-ray Dichroism Experiments 30

2.7.1 Natural X-ray Dichroism experiments 31

2.7.2 Magnetic X-ray Dichroism experiments 32

2.8 Conclusion 35

3 THEORY OF 3d X-RAY DICHROISM OF RARE EARTH MATERIALS 37

3.1 Introduction 37

3.2 The Atomic Description of 3d-XAS of Rare Earth Materials . 38

3.2.1 Calculation of atomic spectra 39

3.2.2 Calculated 3d-XAS spectra 40
3.3 3d X-ray Dichroism of Rare Earths 48
3.3.1 Magnetic X-ray Dichroism, MXD 48
3.3.2 Angular dependence 50
3.3.3 Linear Magnetic X-ray Dichroism 52
3.3.4 Circular Magnetic X-ray Dichroism 54
3.4 Crystal-field X-ray Dichroism 55
3.5 Linear MXD Spectra of Non-collinear Magnetic Moments . . . 57
3.6 Discussion 59
3.7 Conclusion 60

4 MXD IN HIGH MAGNETIC FIELDS 62
4.1 Introduction 62
4.2 Circular polarization filters in the soft x-ray range 63
4.2.1 Introduction 63
4.2.2 Theory and example of MXD 63
4.2.3 Performance of polarization filter 65
4.2.4 Discussion 68
4.2.5 Conclusion 68
4.3 An X-ray Absorption Microscope 70

5 EXPERIMENTAL ASPECTS OF SOFT X-RAY ABSORPTION SPECTROSCOPY 71
5.1 Introduction 71
5.2 A Windowless UHV Double Crystal Monochromator Beamline for Soft X-ray Absorption Studies 73
5.2.1 Introduction 73
5.2.2 Layout of the beamline 73
5.2.3 Monochomator control and data acquisition 77
5.2.4 Performance 79
5.3 The Dutch Experimental Surface Science system at LURE . . 81
5.3.1 General description 81
5.3.2 Preparation chamber 81
5.3.3 Analysis chamber 81
5.4 Multilayer/crystal monochromators for soft x-rays 86
5.5 A high resolution soft x-ray monochromator for synchrotron radiation based on a multilayer/crystal combination 87

5.5.1 Introduction 87
5.5.2 Concepts and basic facts 88
5.5.3 Experimental details 88
5.5.4 Multilayer/KAP throughput 89
5.5.5 Resolution 89
5.5.6 Applications 90
5.5.7 Appraisal of other monochromator devices 91
5.5.8 Conclusions 92
5.6 Experimental resolution in soft x-ray monochromators 94
5.6.1 Introduction 94
5.6.2 Simulation of the experimental broadening 95
5.6.3 Experimental 97
5.6.4 Comparison with experiment 97
5.6.5 Discussion 99

6 X-RAY DICHROISM OF Tb IRON GARNET 101
6.1 Introduction 101
6.2 Experimental proof of magnetic x-ray dichroism 103
6.3 Addendum 106
6.3.1 Experimental details 106
6.3.2 Results and Discussion 106
6.3.3 Conclusion 108

7 AN XAS STUDY OF Tb—Ni INTERMETALLIC COMPOUNDS AND THE Tb/Ni(110) OVERLAYER SYSTEM 111
7.1 Introduction 111
7.2 Experimental 112
7.3 Results and Discussion 114
7.3.1 Bulk compounds 114
7.3.2 Concentration dependence of signal strength 115
7.3.3 Tb/Ni overlayers 116
7.4 Conclusion 117

8 X-RAY DICHROISM AS A PROBE OF THE SYMMETRY OF ULTRA-THIN RARE EARTH OVERLAYERS 124
8.1 Introduction 124
8.2 Experimental 127

8.3 Results 129
    8.3.1 Interface structure and kinetics 129
    8.3.2 Dichroism of as-deposited layers 131
    8.3.3 Dichroism of annealed layers 132
8.4 Atomic model analysis 133
8.5 Discussion 134
    8.5.1 Free-ion Interpretation: Two-domain Model 134
    8.5.2 Crystal field interpretation 136
8.6 Comparison 137
8.7 Conclusion 138

Chapter 1

INTRODUCTION

After having been dormant for the greater part of a century since the discovery by Barkla[1] of the polarized nature of x-rays, the field of polarized x-ray research is being shaken to life rather abruptly by the boom in the production of synchrotron radiation. Polarized x-rays form now a challenging new experimental probe useful for the broad range of sciences covering atomic- and solid state spectroscopy, coordination chemistry and protein structure research. This boom is a result of the increasing availability of polarized x-rays, which are produced with high intensity by electron and positron storage rings.

This thesis deals with one particular kind of x-ray polarization effect, known as *dichroism*, or *the polarization dependence of the absorption spectrum.*

Colours exist because different materials absorb different parts of the spectrum of white light. However, if the light is polarized, some substances show even two colours, and they are said to be dichroic. Dichroism was first described by Biot (1815), who found the colour of crystal platelets of the darkly coloured mineral Tourmaline changed when he varied their orientation with respect to the polarization direction of the light. Indeed, even more coulours are possible, for which one uses the term *pleochromism.*

Dichroism occurs when the electronic structure of the absorbing system is anisotropic. For instance, the electrons of a linear molecule like CO_2 have different resonant frequencies along the axis of the molecule compared to normal to the axis. As a result, the absorption by such a molecule of light that is polarized along the axis differs from the absorption if the polarization is normal to it.

Quite often also solids have an anisotropic electronic structure, like the Tourmaline of Biot. In everyday life, dichroism can be found on the nose of owners of polaroid sunglasses. In such glasses light-absorbing polymer chains have been oriented vertically by stretching the material. As a result, the plastic filters out the horizontally polarized reflections from car roofs and water surfaces.

The second half of the title of this thesis mentions the rare earth elements. This group of 14 elements encompasses the fourth transition series of the periodic table, in which the 4f shell is filled. The rare earth distinguish themselves through the behaviour of the 4f electrons, which in many respects are atomic-like even in solids.

The atomic nature of the 4f shell is certianly apparent in the x-ray excited transitions involving the 4f shell. In particular this is true for the 3d→4f absorption lines, which have been found to exhibit atomic-like multiplet structures that can be simulated quite accurately with atomic model calculations. However, on close inspection it turns out that often the shape of the spectra is not completely atomic, but reflects influences from the surrounding solid. In fact, it is possible to use these modified spectra as fingerprints of these influences. Indeed, the subject of this thesis is the study the dichroism of such spectra, which is the fingerprint of local anisotropies in the surroundings of rare earth ions.

The starting point of this thesis was the prediction by Thole *et al.* [2] of a strong *Magnetic X-ray Dichroism* (MXD) in the 3d→4f spectra of rare earth materials. These predictions were based on the excellent correspondence found between the experimental 3d→4f spectra of poly-crystalline samples and atomic model calculations. However, in the course of the work it was realized that the purely atomic picture in most cases has to be extended to include the symmetry lowering effects of crystal electric fields.

The aim of the work described in this thesis is to answer the question: How can we measure, describe, and use the dichroism present in the x-ray absorption spectra of localized materials, as represented *par excellence* by the rare earth elements. However, to realize this aim it proved to be necessary to spent a quite large amount on the development of experimental techniques. As a result, about half the work presented in this booklet concerns experimental aspects of x-ray absorption in the soft x-ray range.

1.1 Scope of the work

The structure of this thesis is as follows:

Chapter 2 aims to provide a perspective to the different aspects covered by this thesis for the non-expert. It gives an introduction to x-ray absorption spectroscopy and explores polarization effects, both the long-known effects in the visible as well as those in the x-ray range, which have been discovered only quite recently. Furthermore, an intuitive description of the physical ideas underlying MXD. The chapter is concluded with a review of the work on x-ray dichroism so far.

Chapter 3 treats the atomic description of x-ray absorption and MXD of the 3d→4f transition in more detail. Predictions for the linear and circular MXD spectra are presented for all magnetic trivalent rare earth ions. Also crystal field effects are discussed. Finally, since often the magnetic ordering of rare earth materials is very complex, a simplified description of the MXD of non-collinear spin systems is given.

Chapter 4 contains a feasibility-study of the application of the MXD effect to the construction of an x-ray polarization filter or analyzer. In addition we comment on the possibility to use the super-conducting magnet used in such a device as an x-ray absorption microscope. Such a microscope would allow one to perform both elemental mapping of inhomogenous samples and, in combination with MXD, mapping of the domain structure in ferromagnetic materials.

Chapter 5 combines a number of papers dealing with experimental aspects of XAS.

- Chapter 5.1 describes a UHV double crystal monochromator, constructed by our group at the Super-ACO storage ring at LURE, Orsay, France, and used in part of the measurements described here.
- In Chapter 5.2 the UHV experimental system used in the experiments described in later chapters is discussed. Also the different ways of measuring x-ray absorption are discussed.

- In Chapter 5.3 we reprint a paper dealing with the first realization of the long-standing idea to use radiation-sensitive organic crystals as monochromating elements in a double crystal monochromator by protecting them from most of the heatload and x-ray intensity from the storage ring by prefiltering the radiation beam with a synthetic metallic multilayer. We present tests and operating experience with such a monochromator, with the emphasis on spectroscopic applications.
- For many purposes, *e. g.* the characterization of the organic-crystal/multilayer monochromator or the theoretical simulation of x-ray absorption spectra, it is necessary to posses a reproducible method for the characterization of the resolution of soft x-ray monochromators. The article reprinted in Chapter 5.4 describes such a method.

Chapter 6 describes the first experimental confirmation of MXD according to the predictions by Thole *et al.* . The chapter consists of two parts: a reprint of a publication on the first spectra of Tb iron garnet ($TB_3Fe_5O_{12}$), followed an Addendum presenting newer data as well as a reviewed interpretation thereof.

Chapter 7 presents a detailed x-ray absorption study of the Tb—Ni intermetallic compound system and the Tb/Ni(110) overlayer system. Although the study was conceived as a backup-study to the MXD experiment described in the last chapter, it yielded some striking results concerning the probing depth and sensitivity of the measurement technique used: the *total electron yield* method.

Chapter 8 describes the observed X-ray Dichroism effects of the system Tb/Ni(110). This system was selected for a number of reasons: the same system is or was studied by several other groups using different methods, amongst whom colleagues in Nijmegen using spin-resolved inverse photoemission. Also both materials have magnetically interesting edges which are accessible with high resolution by a single monochromator. This has allowed studies of the alloying properties of the overlayer by comparison with the absorption edges of the bulk rare earth—Ni compounds. The results prove X-ray Dichroism measurements on rare earth elements allow the study of the symmetry and magnetism of films of submonolayer thicknesses.

Chapter 2

X-RAY ABSORPTION AND X-RAY DICHROISM: A PERSPECTIVE

2.1 Introduction

Polarized x-ray research is a new field of science. Therefore, probably few readers of this thesis will be acquainted with both parent subjects: *polarization dependent effects in the visible* and *x-ray absorption spectroscopy* (XAS). In this chapter we will discuss both.

The structure of the chapter is as follows: We first give a brief account of the availability of polarized x-ray radiation for spectroscopic purposes. Then the *single particle description* of x-ray absorption is discussed in a fairly didactical way, introducing the nomenclature of x-ray spectroscopy. Later the *atomic description*, which is more relevant for the rest of the thesis, is introduced. The reader familiar with x-ray absorption spectroscopy might skip these first sections.

The second half of the chapter is devoted to polarization dependent phenomena, which are first discussed for the visible and then for the x-ray range. Finally we turn to x-ray dichroism itself, presenting a simple picture for the magnetic x-ray dichroism of the 3d-XAS spectra of rare earth elements that is the main subject of this thesis. The chapter is concluded with a review of x-ray dichroism experiments.

2.2 Generation of Polarized X-rays

The polarization properties of x-rays have hardly been exploited until very recently. This situation was due to the difficulty of generating and manipulating polarized x-rays. A major development was the advent of *electron storage rings* dedicated to the production of synchrotron radiation. When the relativistic electrons (or positrons) in the ring are deflected by the bending magnets that keep them in a closed circular orbit, they emit highly intense beams of linearly polarized x-rays in the plane of the electron orbit. Exactly in the orbital plane the polarization is linear, while slightly above and below the plane the polarization is elliptical, with a degree of circular polarization which increases rapidly with the out-of-plane angle[3]. However, the intensity drops even more rapidly with this angle. As a result, at the moment linearly polarized x-rays are abundantly available, but there have been only few experiments with circularly polarized synchrotron radiation (CPSR), and none in the soft x-ray range. Currently a number of alternative sources for CPSR are under development. The most notable are so-called insertion devices like helical wigglers and crossed undulators[4, 5, 6, 7, 8, 9, 10], which are complex arrays of magnets with which the electrons in a storage ring are made to oscillate in two directions perpendicular to their propagation direction, with the result that they emit circularly polarized x-rays. Alternatively, in the hard x-ray range CPSR can be generated with devices similar to $\lambda/4$ plates used in the visible, but know based on the anomalous scattering properties of perfect crystals[11, 12].

2.3 X-ray Absorption Spectroscopy (XAS)

The absorption of a photon by a solid is an extremely complex phenomenon, and in simulating the spectrum one has to make very drastic approximations. In this chapter we discuss two extreme approaches: the *single-particle approximation* and the *atomic model approximation.*

In the single particle approximation the absorption is viewed as the excitation of a single electron: one electron absorbs the photon and is excited into a higher orbital as a result. Because this model is easy to visualize, and because it was and still is widely applied to describe XAS in free electron-like systems, we will use it to illustrate our introduction to x-ray absorption.

To be specific we will use the 'simple' element aluminium to illustrate some basic notions. In Fig. 2.1, (left), its single-particle electronic structure is represented schematically. It consists of three core-levels, 1s, 2s, and 2p, and a valence band structure which is build up of partial density-of-states with s, p, d, f,$\cdots$ symmetry. The structure of these subbands is due to the scattering and interference of the electron wavefunction on the crystal lattice.

In the single-particle picture, the absorption of visible and ultra-violet

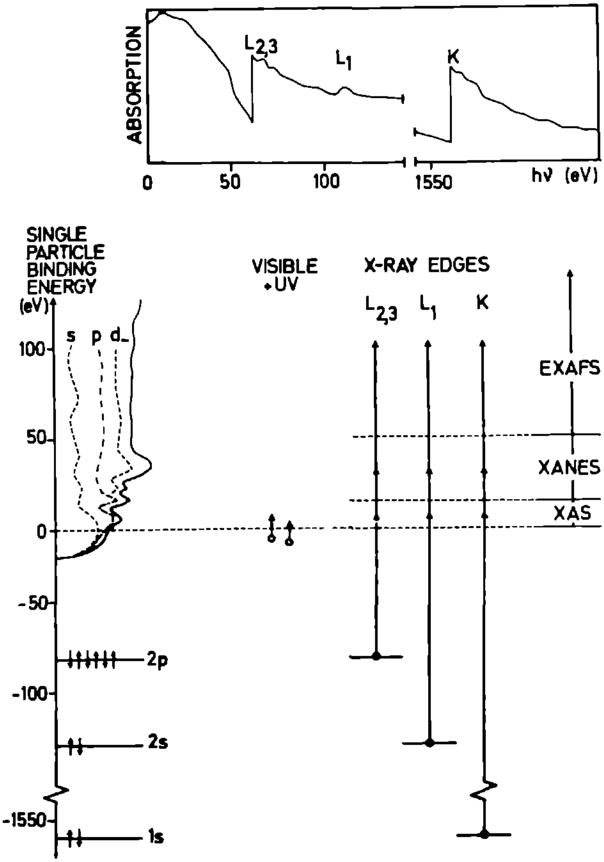

Figure 2.1: Schematic single-particle description of visible, ultra-violet (UV), and x-ray absorption transitions. Top panel: schematical representation of the absorption spectrum of aluminium. Left: single-particle energy scheme, consisting of three core levels (1s, 2s, 2p) and a valence band with contributions of s, p, d, f, ⋯. partial densities-of states. States below the Fermi level ($E = 0$) are filled. Midle: visible and UV intra-band transitions. Right: x-ray transitions. The x-ray spectrum can be divided in regions as denoted on the far right.

light ($\hbar\omega$ = 1–10 eV) involves intra-band transitions of electrons from occupied to unoccupied states, as depicted schematically in the middle of Fig. 2.1. Crudely said, the visible absorption spectrum is a continuum given by the convolution of the occupied with the unoccupied bands. In a more precise picture however, one has to include the impuls-selection rule $\Delta\vec{k} = \vec{0}$ and possibly to allow for phonon assisted transitions[13]. As a result, the interpretation of optical spectra is often prohibitively difficult.

In the x-ray range the spectrum is characterized by a series of sharp steps, or *edges*, that are followed by structured tails (Fig. 2.1, inset). Each edge corresponds to the opening of a core-level absorption channel, and the edges are identified by labels derived from the core-level designation: K, L, M, N$\cdots$ for core levels with principal quantumnumber $n = 1, 2, 3, 4 \cdots$. Subscripts to these labels number consecutive edges and will be discussed more completely below. In Fig. 2.1 (inset) the L_2 and L_3 edges lie too near to each other to be drawn separately.

2.3.1 Nomenclature

The x-ray absorption spectrum from a particular edge, *e. g.* the K edge in Fig. 2.1 are divided in three to four regions:

- In the *pre-edge* region the absorption is due to the rather structureless tails of the occupied valence electrons and the shallower edges (*e. g.* the $L_{1,2,3}$ in Fig. 2.1).

- At the edge the absorption intensity suddenly rises and often shows pronounced structure. The 50 eV wide interval above the edge is the *XANES* (x-ray absorption near edge structure) region which is dominated by *multiple scattering* effects of the excited photoelectron in the cluster of atoms surrounding the absorbing site.

- In the *EXAFS (extended x-ray absorption fine-structure)* region, extending from 50 eV above the edge until the next edge the spectrum shows slow oscillations with energy. The initial amplitude of the fine-structure oscillations can be 5–10% of the mean absorption, and decreases slowly over the next 500–1000 eV. These oscillations arise because the excited photoelectron is partially reflected back by the first few shells of atoms around the absorbing atom. At kinetic energies greater than 50 eV the wavelength of the outgoing spherical wave of the excited photoelectron becomes comparable to the atomic spacing and, going to higher energies, the wave will interfere alternatingly constructively and destructively with itself.

The structure in the EXAFS region can be well described with *single scattering* theory. EXAFS oscillations are widely studied because from a Fourier analysis of the oscillations one can obtain the bond lengths and coordination numbers of the absorbing atom, *i. e.* the local geometry[14].

- Often the denotation *XAS* is used for the first 15 eV of the XANES region. This region in general shows the sharpest features and is studied with high resolution monochromators.

Spectroscopically the most interesting XAS edges are in general the K, $L_{2,3}$ and $M_{4,5}$. This is mainly because these edges have the highest cross-sections, *e. g.* in Al the L_1 is about 10 times weaker than the $L_{2,3}$ or K edges[15]. Also L_1 and $M_{1,2,3}$ edges often lie superposed on the EXAFS of the $L_{2,3}$ and $M_{4,5}$ edges (see Fig. 2.1). Finally, edges from the same shell have a lifetime broadening that decreases with increasing orbital momentum of the hole state[16, 17].

2.3.2 The core-hole spin-orbit splitting

The spin of the hole left in the core-level can be either parallel or antiparallel to the hole's orbital angular momentum l, leading to two possible final core states with $j_\pm = l \pm 1/2$, which differ in energy by the spin-orbit interaction of the core-level. The XAS spectra from core levels with $l \neq 0$ are therefore split in two parts, labelled as $L_{2,3}$ ($2p_{1/2}$, $2p_{3/2}$), $M_{2,3}$ ($3p_{1/2}$, $3p_{3/2}$), $M_{4,5}$ ($3d_{3/2}$, $3d_{5/2}$) etc. . All have the shape of the partial density-of-states. To a first approximation the intensity ratio between the $j_- = l - 1/2$ and the $j_+ = l + 1/2$ states is $(2j_- + 1)/(2j_+ + 1)$, or 1 : 2 for $L_{2,3}$ and $M_{2,3}$ edges and 2 : 3 for the $M_{4,5}$ edges. In the presence of the atomic correlations discussed below, the spin-orbit splitting of the final state can change these ratios drastically[18].

For the Al example in Fig. 2.1 the spin-orbit splitting is only ~0.4 eV and is too small to be resolved. For deeper core levels the splitting increases

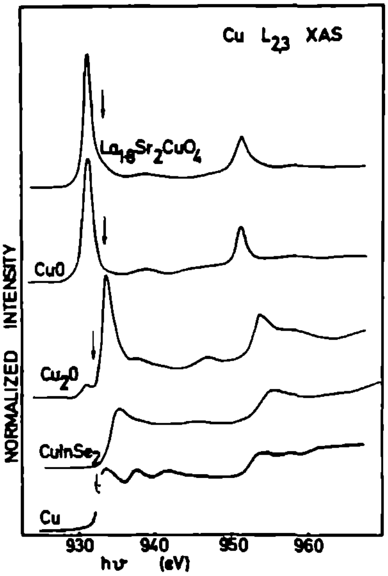

Figure 2.2: The 2p-XAS spectra of Cu compounds with different valencies, showing the splitting into L_2 ($2p_{1/2}$) and L_3 ($2p_{3/2}$) edges due to the strong spin-orbit coupling of the 2p core level[19].

rapidly. This is illustrated in Fig. 2.2 which shows the $L_{2,3}$ spectra of a number of Cu compounds of different valencies. This figure also illustrates nicely the different edge shapes observed in practice. Cu metal has a step-like edge followed by two broad features. The spectrum of Cu_2O on the other hand shows sharp resonances, called *white lines* because of their appearance on the photographic films used in the early days of XAS.

2.3.3 Golden Rule description

The earliest approach to the description of x-ray absorption spectra, and one which is still widely used, employs the single-electron model as a starting point. In this picture, the core-electron is excited in the unoccupied continuum states of the system. According to Fermi's Golden Rule the transition probability per unit time from a bound state to a continuum state can be written as

$$w = \frac{2\pi}{\hbar} \left|\langle k|P|c\rangle\right|^2 \rho_f(\hbar\omega - E_c) \tag{2.1}$$

where $|\langle k|P|c\rangle|$ is the matrix element of the electromagnetic field operator P between the core-electron state $|c\rangle$ and the valence state $|k\rangle$, $\rho_f(E)$ is the density of valence states at the energy E above the Fermi level and E_c is the core-electron binding energy.

The operator P can be written as[20]

$$P = e^{i\frac{\omega}{c}\hat{\mathbf{n}}\,\mathbf{r}}\mathbf{p}.\hat{\mathbf{e}} \tag{2.2}$$

where $\hat{\mathbf{n}}$ is the light propagation vector, $\hat{\mathbf{e}}$ the polarization vector, and $\mathbf{r}$ and $\mathbf{p}$ are the electron position and momentum operators. It is customary, and usually valid, to make the electronic dipole approximation, wherein the exponential is replaced by unity, giving

$$|\langle k|P|c\rangle| \approx |\langle k|\mathbf{p}.\hat{\mathbf{e}}|c\rangle| \tag{2.3}$$

Since the electric dipole operator is odd, and acts on the radial part of the electronic wavefunction only, transitions can be made only between states which have opposite parity and differ in angular momentum by one: $\Delta l = \pm 1$, with $\Delta s = 0$, the *dipole selection rules.* For instance, in Fig. 2.1 the K and L_1 edges have p final states and the $L_{2,3}$ edges s and d final states. Since the core state $|c\rangle$ is strongly localized on the nucleus, the matrix element is also local to the atom[21]. A somewhat loose formulation of the above states that: *x-ray absorption spectra give the site- and symmetry-selected unoccupied electronic levels of the absorbing atom.*

The usefulness of the golden rule approach to XAS is illustrated in Fig. 2.3, left, where the experimental Si K-edge spectrum of $NiSi_2$ is compared with the unoccupied Si p-DOS [22]. Although some peak positions are right, large discrepancies occur near the Fermi level. On the right it is shown that inclusion of the energy dependence of the matrixelement does not improve the situation much[22].

This example clearly indicates the limitations of the single electron picture. The poor agreement really is not very suprising in view of the complete neglect, first, of the dynamics of the transition and, second, of the relaxation of the electron system to the new charge distribution in the presence of the core hole. With the advent of both more reliable band structure calculations

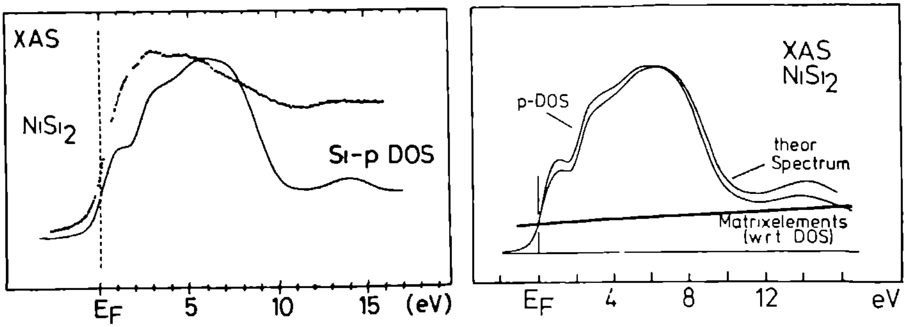

Figure 2.3: Left: Si K edge (1s→*unoccupied p states*) of $NiSi_2$ compared with unoccupied Si p-partial density-of-states (DOS). Right: comparison of Si p-DOS with theoretical spectrum which includes the energy dependence of the Golden Rule matrix element (also shown).

and improved experimental technique the deficiencies of this model are increasingly felt. Several attempts have been made to improve the description by going to the other extreme of the single particle description, wherein the spectrum is compared with the unoccupied states of the final state charge distribution, *i. e.* the solid is allowed to relax completely around the core-ionized atom[23, 24, 25]. At the moment it is still a subject of discussion as to if and where the final state description indeed is better than the simpler initial state description.

However, the real problem of the core hole is the importance of atomic-like many-body interactions between the multipole moments of the core hole and those of the valence levels. Our understanding of such interactions is still in its infancy, although important progress know is being made[26].

2.3.4 N-particle description

Absorption edges involving a localized final state, like for instance the transitions 1s→2p in O, N, F; 2p→3d in the 3d transition metals; and 3d→4f in the rare earth elements, are more naturally described in terms of a local model-Hamiltonian, *e. g.* atomic[27, 28, 29, 2] impurity[30, 31, 32, 33, 34], crystal field[35, 36] or cluster models[37, 38]. In such a description one sacrifices a large amount of the properties of the solid in order to be able to perform a many-body calculation on the remaining electron system.

In the atomic model the transition is viewed as taking place between the ground-state and excited state of the complete atom. The situation is illustrated in Fig. 2.4 for the $4f^N \rightarrow 3d^9 4f^{N+1}$ x-ray absorption transition of the rare earth elements. The description involves calculation of the discrete energy levels of the initial- and final state N- particle wavefunctions (multiplets). Each multiplet state has a definite atomic angular momentum quantum number J. In this description the dipole selection rules are $\Delta J = 0, \pm 1$. The spectrum is formed by the superposition of all the selection-rule allowed transitions from the ground state to the levels of the final state multiplet. An important consequence is that while in delocalized electronic systems the core-hole problem seriously hampers the interpretation of XAS spectra, it has been shown that it can be succesfully taken into account in an atomic-like picture[27, 28, 29].

Notably for transitions involving the 4f shell of the rare earth elements the match between the measured spectra and calculations based on the aotmic picture is almost perfect. This is illustrated in Fig. 2.5[2], where the experimental M_5 spectrum of Dy metal is compared with the calculated spectrum of a trivalent Dy ion (ground-state $^6H_{J=15/2}$). For later reference we remark here that the theoretical spectrum consists of three contributions with $\Delta J =$ 1, 0 and -1, which appear in well separated groups, as is shown in the lower three panels of Fig. 2.5.

2.4 Polarization Phenomena in the Visible

Before turning to polarization phenomena in the x-ray range, it is worthwhile to consider briefly the visible light absorption phenomena.

As was already mentioned in Chapter 1, *dichroism* is the dependence of the absorption of light on the polarization state of the light. Well known examples of dichroic materials in the visible are tourmaline, which changes its colour from blue to green when it is turned in linearly polarized white light, and polaroid sunglasses. In these cases the asymmetry in the charge distribution leading to dichroism is due to respectively the low symmetry crystal structure and stress in the polymer film. Below we will see also magnetic fields can give rise to dichroism.

Simple symmetry considerations imply that dichroism can not occur in systems which have cubic or higher symmetry, *i. e.* where the three Cartesian

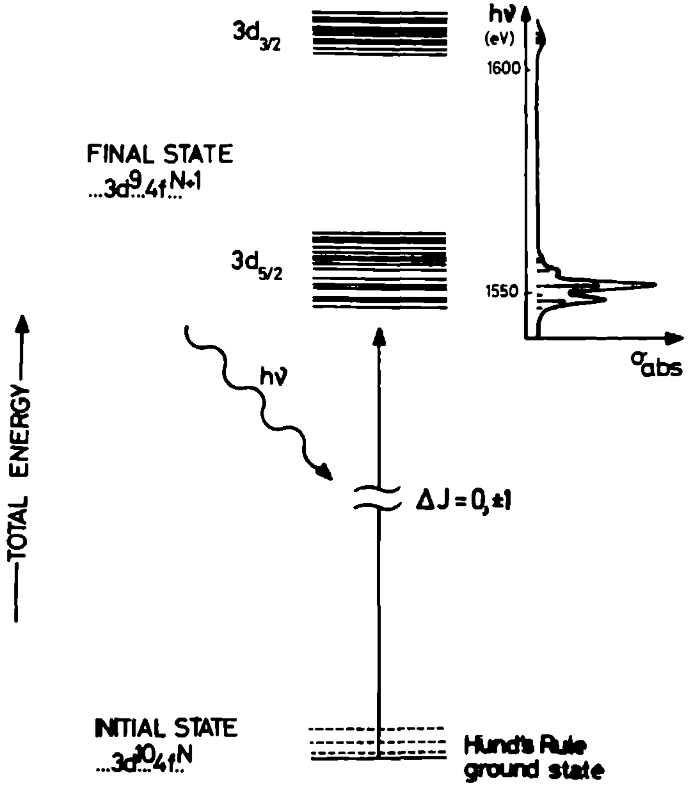

Figure 2.4: Atomic description of 3d-x-ray absorption transitions of rare earth ions. The initial multiplet ($4f^N$, $N = 0$–14 is the 4f occupation number) is 1 to 5 eV wide, with only the lowest state, given by Hund's rules, occupied. The final state multiplet $3d^9 4f^{N+1}$ is split in two parts by the 3d spin-orbit interaction and, depending on N, consists of two lines for ytterbium to several thousands for gadolinium. The dipole selection rules $\Delta J = 0, \pm 1$, allow only a part of these lines to be reached from the initial state.
Inset: Sticks: the matrix elements of the allowed lines. Full curve: line spectrum broadened with lifetime and experimental resolution contributions, corresponding to the observed spectrum.

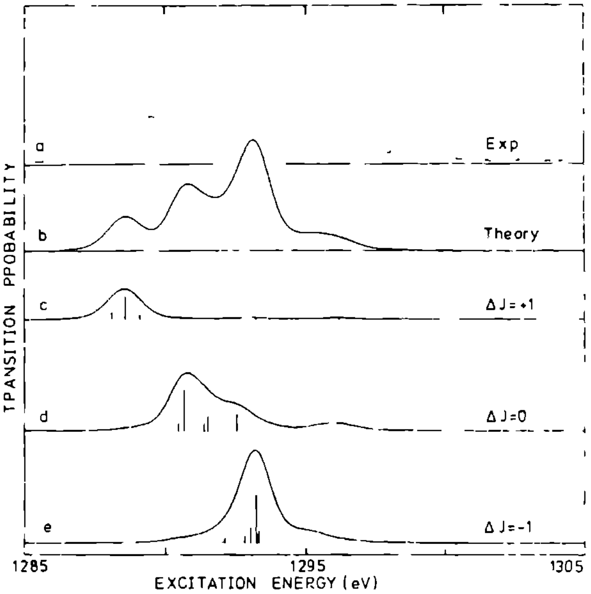

Figure 2.5: (a) Experimental and (b) theoretical M_5 XAS spectra for Dy^{3+} ($4f^9$) in a non-magnetic ground-state. The separate contributions with $\Delta J = 1, 0, -1$ of this spectrum are shown in (c), (d), and (e), respectively.

directions are equivalent[39] (point groups $T, T_h, T_d, O, O_h, I, I_l$). Similarly, circular dichroism, meaning different absorption for left and right-handed circularly polarized rays, can occur only when the point group of the system does not contain a plane or a center of symmetry.

Dichroic materials are also *double refractive (birefringent)*: a ray of unpolarized light which is incident on a transparant material is, upon refraction at the surface, split in two conjugately polarized rays that travel in different directions. Expressed less concisely, the refractive index in such materials varies with direction and polarization. Double refraction is easiest observed in the transparent regions away from the dichroic absorption bands, like in the well-known examples Icelandic spar, quartz, mica, and the highly stressed windshields of cars. The occurence of polarization dependent effects at wavelengths other than that of the dichroic absorption bands is due to the fact that there the electrons of a solid act as strongly damped anisotropic oscillators interacting with the photon radiation field (see also below).

2.4.1 Magnetic Circular Dichroism

Obviously polarization dependent measurements can give information on the symmetry of the absorbing atoms, and therefore in the visible such techniques form standard extentions of absorption experiments. The one most used is magnetic dichroism (MD), where the absorption spectrum of a sample in an applied magnetic field is measured as a function of temperature.

Magnetic dichroism was discovered by Zeeman in 1886 in his famous experiments on the emission and absorption by ions of sodium and other elements in a magnetized flame[40]. Initially he found the light emitted normal to the field direction consisted of a triplet. The two outer lines proved to be linearly polarized normal to the plane containing the field and light directions (σ polarization) while the center line was polarized in this plane (π polarization), see Fig. 2.6. Soon after this discovery Lorentz was able to explain these observations with his model of the electron as an oscillating charge in the atom[41], and even could predict that light emitted along the field direction consists of a doublet of circularly polarized components with opposite senses of rotations. This was soon afterwards confirmed by Zeeman. Later, in addition to these 'normal' Zeeman patterns also 'anomalous' splittings, consisting of more than three components, were observed, which could not be explained until the discovery of the electron spin in 1925. This points to the essential role of spin-orbit coupling for a detailed understanding of magneto-optical effects, as will be evident from the discussion of x-ray dichroism effects given below.

Magnetic dichroism is the absorptive counterpart of the Zeeman emission effect, and indeed is sometimes called the *inverse Zeeman effect*. It turns out that the experimentally most convenient geometry for magnetic dichroism studies is that wherein an alternatingly left- and right circularly polarized beam travels along the direction of the magnetic field. Also it yields all the information derivable from the use of other geometries or linear polarizations. This form is known as *magnetic circular dichroism* (MCD). The theory of MCD spectra in the visible has been given by Stephens[42].

An important class of materials amendable to MCD measurements is formed by the transparent insulating 3d transition metal compounds. In these materials the optical transitions involve the narrow crystal field levels of the 3d shell. 3d→3d transitions are both spin- and parity-forbidden but can acquire intensity by exchange, spin-orbit and vibrational interactions[42, 43].

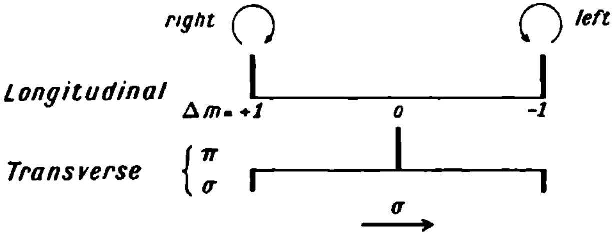

Figure 2.6: Normal Zeeman splitting of the emission from a magnetized radiation source. Top: circularly polarized doublet as observed along the light direction.
Bottom: π and σ polarized linearly polarized triplet as observed perpendicular to the field direction.

This makes the interpretation of MCD spectra quite involved, but it is possible to obtain information on these interactions[42], as well as information on the *symmetry, magnetic moments* and *wavefunctions* of both the initial and final states of the absorbing atom[44, 43].

Related to the MCD effect are the *Faraday effect*: the rotation of the polarization vector of light travelling through magnetized materials, and the *magneto-optical Kerr effect* (MOKE): the rotation of the polarization on reflection.

MOKE derives its practical importance from the fact that important classes of magnetic materials are non-transparent, making them unsuitable for Faraday and MCD measurements. In the last two decades MOKE studies received extra impetus from the possibility of using the effect in high-density magneto-optical storage systems[45, 46]. However, the theoretical description of the MOKE of non-transparant materials (and indeed any other magneto-optical effect in the visible) is enormously complicated, because both the initial- and the final-state lie within the electron bandstructure, so that one has to evaluate all $\Delta\vec{k} = 0$ transitions between all occupied and all unoccupied bands[47, 48, 49, 50]. Also, because of the importance of spin-orbit coupling, a proper description of magneto-optical effects in band-like ferromagnetic materials involves relativistic spin-polarized bandstructure calculations and is therefore both mathematically and computationally less tractable. These problems have been one of the motivations for studying magnetic *x-ray* dichroism, because in x-ray absorption the initial state is a simple core state[51].

2.5 X-ray Polarization Effects in Solids

Optics in the x-ray range differs in important respects from visible optics. First of all, hard x-rays have great penetrating power, often allowing absorption measurements on materials not transparent to visible light. Furthermore, with x-rays the wavelength is comparable to the size of atoms and their spacings, giving rise to strong interference which leads to the diffraction effects which have long dominated x-ray research. Also the short wavelength makes a description of light-matter interaction in terms of a quasi-continuous dielectric tensor, as is used in the visible, less appropriate. A more natural description is in terms of the atomic scattering factors, $f = f_1 + if_2$. f_1 and f_2 are interrelated by the Kramers-Kronig relations, and have been tabulated for the x-ray range by Henke *et al.* [52]. The complex refractive index is related to f_1 and f_2 by $n = n_1 + in_2 = 1 - Kf_1 - iKf_2$, with K a material and wavelength dependent constant[52].

As we saw in Fig. 2.1, in the x-ray range the absorption edges are fairly widely spaced, and in light materials like Al even absent at high photon energies. Thus, according to the Kramers-Kronig relations, away from absorption edges f_1 is small, so that the real part of the refractive index, $n_1 = 1 - Kf_1$, is close to unity in most of the x-ray range. Consequently in general no strong polarization mixing effects can occur in the x-ray range. Some authors even have claimed such effects would be absent[53]. Nevertheless, as we will see below, x-ray polarization effects now appear to be abundant. Such effects can be divided in a group of pure scattering effects arising purely from geometrical conditions, and in a group of dichroism related effects. We will give a short review of scattering effects before turning to x-ray dichroism itself.

2.5.1 Anomalous x-ray scattering and birefringence

Transmission through perfect crystals, *i. e.* crystals without mosaic spread, is described by dynamical diffraction theory[54]. According to this theory, when an x-ray beam enters a perfect crystal under the Bragg condition, it forms four wavefields: two with π polarization (polarization parallel to the scattering plane) and two with σ polarization (perpendicular to the plane). Both the π and the σ pairs are further divided in a wavefield component which has its wave nodes in between the atoms (α-branch) and one which has its nodes on the atoms (β-branch), see Fig. 2.7. Because of the greater over-

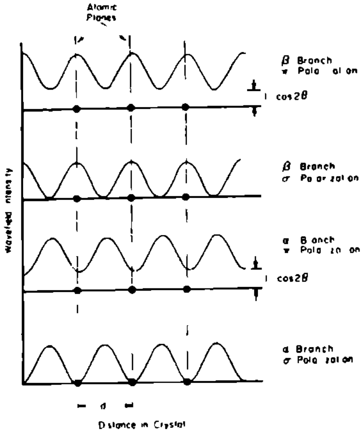

Figure 2.7: Standing x-ray wavefields at the Bragg condition of the transmitted beam in a perfect crystal. Taken from Mills[11].

lap with the electronic wavefunctions, β-branches are anomalously absorbed *Borrmann effect.* Thus an unpolarized beam upon transmission through a thin crystal platelet becomes linearly polarized, or, if the thickness is chosen judiciously, even circularly polarized, because of a thickness dependent phase shift between the α_π and α_σ-branches[55, 56]. On the basis of this effect practical polarization filters acting as $\lambda/4$ plates for 10–100 keV synchrotron radiation have been constructed recently[12, 11].

As was shown by Templeton and Templeton[57, 58, 59], also crystals with mosaic spread can display birefringence. In these cases however the birefringence results from the polarization dependencies of f_1 and f_2 caused by dichroic effects in nearby absorption edges, and we will discuss some of these data in more detail below.

Other polarization dependent x-ray scattering effects involve magnetism. The scattering cross section of x-rays also contains terms which depend on the electron spin- and angular-momentum densities[60, 61]. Although these terms give only a low cross-section this problem is more than compensated by the intensity of synchrotron radiation sources. Near absorption edges larger effects have been observed[62] that arise from magnetic x-ray dichroism and the Kramers-Kronig relations (resonance scattering). Magnetic x-ray scattering offers several possibilities complementary to magnetic neutron scattering, such as the possibility to measure the spin and angular contributions to the magnetic field separately, and the possibility of thin film experiments. Although this technique is still in an early stage of development it promises to be exceedingly powerful.

Another term in the x-ray scattering cross section is the magnetic Compton scattering contribution. Measurements with circularly polarized synchrotron radiation of 30 to 100 keV have yielded the momentum distribution of the magnetic electrons in ferromagnetic materials[63, 64, 65].

2.6 X-ray Dichroism

In this penultimate section we turn to a discussion of pure x-ray dichroism effects. We start by presenting a simple model for the magnetic and crystal field dichroism of the 3d-XAS spectra of rare earth studied in this thesis. For this we return to the atomistic description of XAS and the Dy example given earlier. Subsequently a review of other x-ray dichroism effects is presented.

2.6.1 3d-Magnetic X-ray Dichroism

To explain the mechanism of MXD we turn first to the very simple example of trivalent Yb, which has a 3d-XAS spectrum ($3d^{10}4f^{13} \rightarrow 3d^{9}4f^{14}$), as illustrated in Fig. 2.8. In the field-free ion spin-orbit interaction leads to splitting of both the initial and the final states into $^2F_{7/2}$, $^2F_{5/2}$ ($\zeta_{SO} = 0.366$eV) and $^2D_{5/2}$, $^2D_{3/2}$ ($\zeta_{SO} = 19.4$eV) respectively. The $^2F_{7/2}$ is the Hund's rules ground state. The only allowed transition is $^2F_{7/2} \rightarrow {}^2D_{5/2}$ with $\Delta J = -1$ (see Fig. 2.8, left), while the transition to $^2D_{3/2}$, which would constitute the M_4 line, is dipole forbidden.

When the spherical symmetry is broken by a magnetic field the $\Delta J = -1$ line is split into 18 lines divided over three groups with different ΔM. Lower in the figure the division of the linestrength over these lines (given by the squared 3-j symbol, see next chapter) is indicated and, at the bottom, the polarization state pertinent to the different ΔM transitions: left and right circularly polarized for $\Delta M = \pm 1$, and parallel linearly polarized for $\Delta M = 0$.

At sufficiently high temperatures all the levels remain populated and as the splitting is much smaller than the experimental resolution it has no effect on the spectrum. However, the occupancy of the levels is governed by

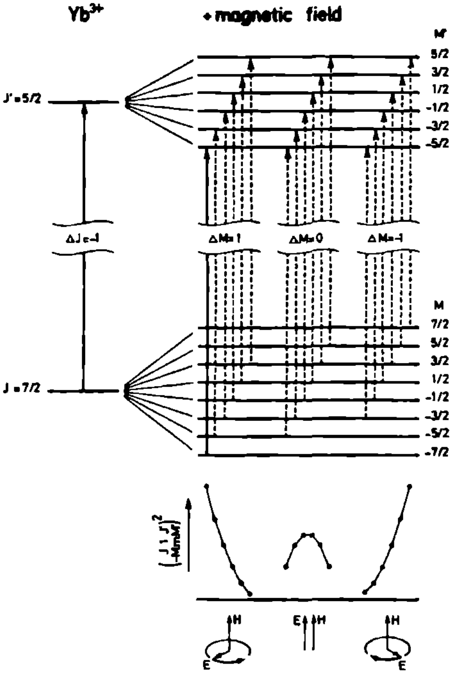

Figure 2.8: Energy diagram of the $3d^{10}4f^{13} \rightarrow 3d^{9}4f^{14}$ transition of Yb^{3+} without (left) and with (right) a magnetic field. The vertical arrows indicate the dipole selection rule allowed transitions $|\alpha J\rangle \rightarrow |\alpha' J'\rangle$. Their relative intensities are given by the dots. The required polarization state is indicated at the bottom.

Boltzmann statistics so that when the magnetic field splitting $g\mu_{Bohr}H$ is sufficiently large relative to the thermal energy k_bT, the upper levels are less occupied, and this has an effect on the observed absorption cross section. From the figure it can be seen that in the limit of 0 K only the lowest level is occupied. Then absorption will take place only if the light has a left circularly polarized component. At intermediate angles or temperatures the absorption intensity of the $\Delta J = -1$ line varies between 0 and the field-free value.

The case of Yb^{3+} is exceptional in that a single $\Delta J = -1$ line composes the whole spectrum. For other elements the spectrum contains also components due to $\Delta J = 0$ and $+1$ transitions (*cf.* Dy in Fig. 2.5). As discussed in more detail in the next chapter, the temperature and field dependencies of these components have cross sections which, though subject to the same mechanism as the $\Delta J = -1$, have strongly different dependencies on field, temperature and polarization. The net effect of this is illustrated in Fig. 2.9[2], where the unpolarized spectrum is compared with the predicted $T = 0$ linear polarization spectra with the polarization parallel and perpendicular to the field. As an example of experimental dichroism spectra we show in Fig. 2.10 the spectra of a Dy monolayer on a Ni(110) surface, taken at 70 K with the polarization vector making an angle of 0° and 70° respectively with the surface $[1\bar{1}1]$ direction. Large dichroic effects in accordance with the theoretical predictions are evident, although the effect is of course smaller than the $T = 0$ K predictions. A complete discussion of similar experiments on Tb overlayers on Ni(110) is given in Chapter 8.

2.6.2 Crystal field effects

Although the crystal field interactions acting on the rare earth 4f levels are small, they may very well be comparable to the spin-orbit interactions. The initial predictions by Thole *et al.* [2], were based on the observed good correspondence between experimental data and the atomic predictions[29]. The experimental 3d-XAS spectra that were used for the comparison were however all taken on polycrystalline samples. Possible crystal field induced dichroism effects in these spectra are obscured by the angular averaging in the polycrystalline material. To illustrate this point we will briefly touch on crystal field induced dichroism in the 3d-XAS spectra.

In Fig. 2.11 we show the effect of a crystal field of axial symmetry on the Yb^{3+} spectrum. (The field is assumed to be represented by the O_2^0 *equivalent operator*[66, 67] As shown in the figure, in such a field the initial and final states split up into a series of Kramers doublets $|\pm M\rangle$. Like in the magnetic case the $\Delta J = -1$ line splits into three ΔM groups, but now each group has four components with different energies instead of six (*cf.* Fig. 2.8). The consequences for the dichroism are easily seen from the $T = 0$ K situation: now both circular polarized transitions remain possible. Also it can be seen that the temperature dependence of the cross section is different from the magnetic case.

In this particular case no intermixing of the magnetic substates occurs.

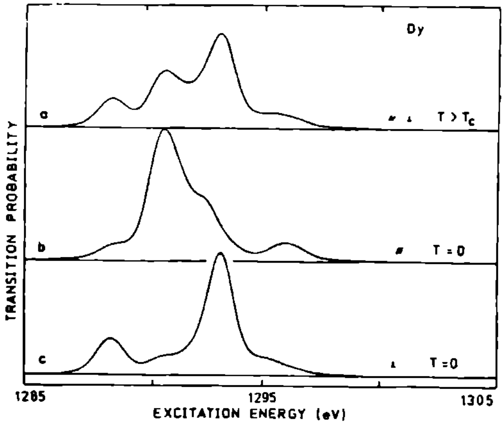

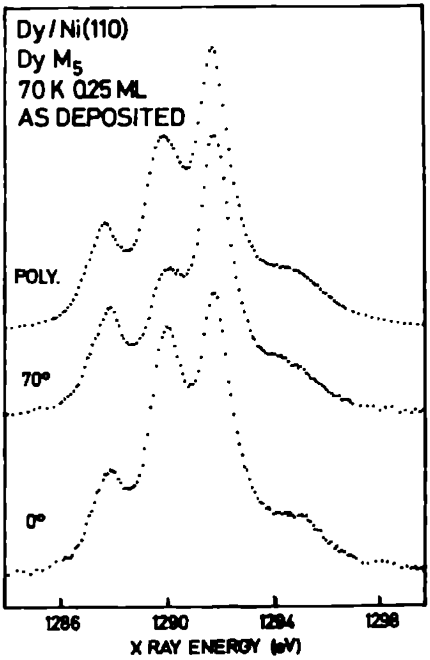

Figure 2.9: (a) The calculated 3d-XAS spectra of Dy^{3+} for disordered atomic moments (a) and for magnetically aligned ions at $T = 0$ K with linear polarization parallel (b) and normal (c) to the magnetization.

Figure 2.10: Lower two curves: Dy M_5 XAS spectra of a 0.25 ML Dy film on Ni(110), measured at 70 K, with the polarization vector $\mathbf{E}$ making an angle of 0° and 70° respectively with the $[1\bar{1}1]$ direction. Top curve: Spectrum of a thick polycrystalline film.

However, if the field has lower symmetry this is no longer true; the crystal field levels are formed by a linear combination of different atomic sub-states $|M\rangle$. In some cases the lowest crystal field level can contain contributions from all states $|M\rangle$ with the result that even at $T = 0$ K some transitions are always possible for any polarization, resulting in a reduction of the dichroism.

2.7 Review of X-ray Dichroism Experiments

We will conclude this chapter with a review of x-ray dichroism experiments by other groups. For work in the 10–100 eV range, we refer to Ref.[68]. Natural dichroism experiments are discussed prior to magnetic experiments.

2.7.1 Natural X-ray Dichroism experiments

Large linear dichroic effects have been found in the XAS spectra of layered compounds ($TaSe_2$[35], TiS_2[69]), molecular solids (Cu^{II}, metal-organic complexes[70, 71]), surfaces[72, 73], and high-T_c superconductors[74]. If at all, the data were always interpreted in the single-particle model; either only qualitatively in terms of unoccupied crystal field orbitals[42, 71], or quantitatively by comparison to local-density bandstructure[69] or cluster calculations[70]. As remarked in Chapter 1, because of the spherical symmetry of the core hole in such a description the dichroism arises from final state asymmetry only.

In a series of studies devoted to anomalous diffraction effects caused by diffraction of absorption edges, Templeton and Templeton[57, 58, 59] found strong dichroic effects in systems which were known to be dichroic in the visible. Unfortunately these authors do no interpret these spectra in detail. A particularly intriguing example of their work is reproduced in Fig. 2.12[58], showing the linear dichroism of the U L_1 (2s→np) edge of $RbUO_2(NO_3)_3$. Large dichroic effects are visible, as well as a large apparent shift in edge position of ~13 eV between the two polarizations. The dichroism can easily be understood from the structure of the uranyl ion, UO_2^{2+}, which has a linear O—U -O configuration, with contributions to the bonding from the U 7s, 7p, 6d, and 5f orbitals[75]. However, it is unlikely that the 7p density of states in the U—O bond direction is suppressed over an interval of 13 eV from the Fermi level for one polarization, and it is therefore likely that we have here a case where the screening orbital that can be reached by the dipolar transitions is different for the two polarizations of the light. The size of the effect would require the two final states to have very strongly differing *radial* distributions, possibly through different mixing of p and f states in the two directions. Similar effects are also found in the Uranyl L_3 and Bromate K spectra[57, 58].

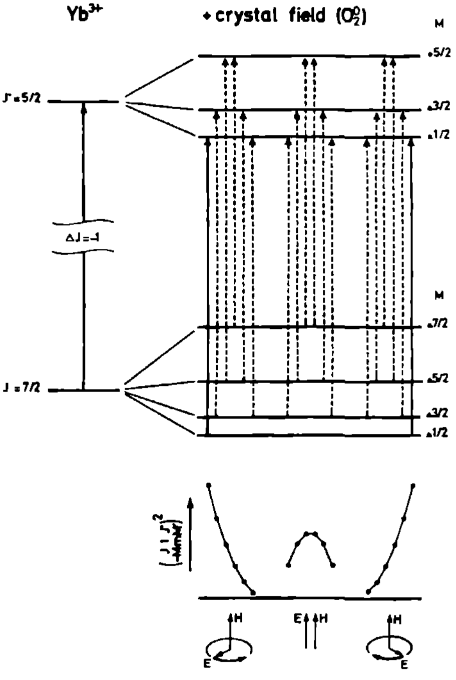

Figure 2.11: Energy diagram of the $3d^{10}4f^{13} \rightarrow 3d^9 4f^{14}$ transition of Yb^{3+} Left: free-ion spectrum. Right: weak axial crystal field O_0^2. Compare with Fig. 2.8.

2.7.2 Magnetic X-ray Dichroism experiments

Prior to the prediction by Thole *et al.* [2] of the strong MXD described in this thesis little work had been done in the field of x-ray magneto-optics.

The first work seems to be the calculation by Erskine and Stern[47] of the MOKE in the $M_{2,3}$ (3p→3d) region of Ni ($\hbar\omega = 64$ eV). A substantial change (~10%) in the reflection of π-polarized light was predicted, due to magnetic dichroism in the edge. These authors noted that although the magneto-optical effects involving transitions from s-core states to p-conductionband states would be much smaller, *e. g.* $10^{-3}\%$, they would allow one to measure the exchange splitting of the unoccupied p states, which is difficult to measure with other techniques.

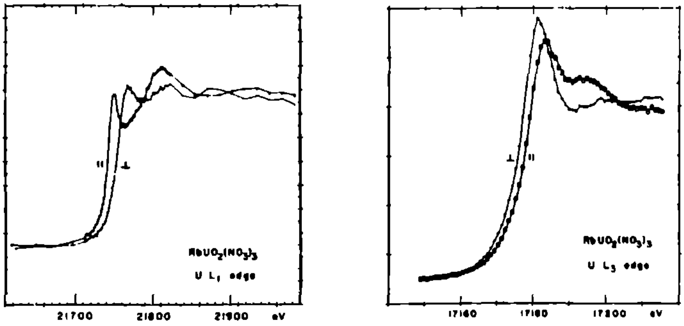

Figure 2.12: Linear dichroism of the L$_1$ edge of the uranyl ion, showing a difference in edge position of 12 eV. Figure taken from Templeton and Templeton[58]

Subsequently a search was made for circular dichroism in the Gd L$_3$ edge (2p→5d, $\hbar\omega$ = 7243 eV) of a foil of an amorphous GdFe alloy by Keller and Stern[76]. These authors used the out-of-plane CPSR (see page 13) in the MCD (see page 23 transmission geometry, employing a small electromagnet to orient the magnetic domains in the sample. An upper limit of 0.02 % was established for the dichroism.

Recently a more sophisticated form of this experiment has been developed by Schütz *et al.* . With their setup these authors measured the magnetic dichroism spectra of a whole range of ferromagnetic materials, including elements (Fe[77], Ni[78], Gd and Tb[79]), oxides, intermetallic compounds and impurity systems[78]. The effects are of the order of 0.05–1% of the total cross section, with the exception of the impurity systems, where ~ 25% effects were observed. As an example we show in Fig. 2.13 the results for the Fe K edge, compared with relativistic spin-polarized bandstructure calculations[51, 80]. The agreement between the measured and calculated dichroism is remarkable, especially considering the large discrepancies between the measured and calculated total cross section, which are of the order of 10%.

A simple picture used by Schütz *et al.* to explain their data splits up the single particle description in two steps. In the first step the CPSR excites a spin-polarized electron from the unpolarized core hole. This electron is then

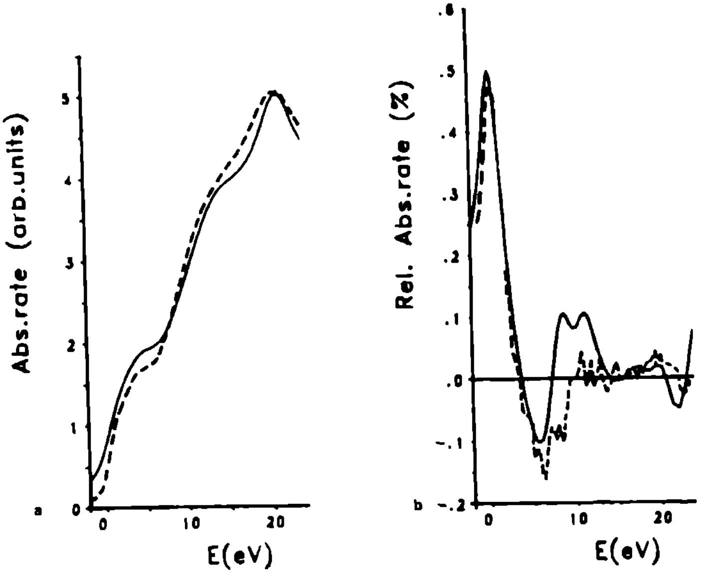

Figure 2.13: Dashed lines: Direct and magnetic circular x-ray dichroism spectra of the K-edge of iron compared with spin-polarized relativistic band-structure calculations (full curve). Figure taken from Schütz *et al.* [77].

thought to drop into the exchange-split unoccupied density of states.

In the K edge experiments the polarization dependence can be understood from spin-orbit interaction induced differences in the *radial part* of the matrix elements from the 1s to the $p_{1/2}$ and $p_{3/2}$ final states of free atoms, as discussed by Fano[81] (see also Delone *et al.* [82]. In this case the effects are rather small because the net electron polarization of this internal source of spin-polarized electrons is small for most edges. Much larger effects are found in the L edge since there the *angular part* of the dipole matrix elements leads to much bigger electron polarizations[83]. Indeed, as discussed in Chapter 3, in describing the 3d-dichroism of the rare earths, we use solely the angular part.

Finally, very recently more theoretical work has appeared. Jo and Imada have presented impurity calculations that include 4f hybridization effects for the magnetic dichroism of the 4d and 3d edges[34, 84] of Ce compounds. Furthermore, Carra and Altarelli have presented a systemetical analysis of the magnetic terms of the electric multipole expansion. They derive a general formulation for linear and circular dichroism, and show that quadrupole terms may in some cases contribute importantly[85].

2.8 Conclusion

In this chapter we have tried to give a background to x-ray absorption and x-ray polarization phenomena with which one can read the rest of this thesis.

We have given an introduction to XAS based on the single particle and the atomic limits. Also we have discussed a few of the many polarization dependent effects known in the visible, in particular magnetic circular dichroism (MCD) and the magneto-optical Kerr effect (MOKE), and most of the less abundant effects in the x-ray range.

Magnetic x-ray dichroism was introduced using the very simple case of the 3d→4f absorption line of trivalent Yb. A review of x-ray dichroism experiments, including both natural and magnetic dichroism was given.

It is evident from the material in this chapter that many new experiments are possible with polarized x-rays. This is reflected also in the number of beamlines with special polarization characteristics planned or under construction at a large number of synchrotron radiation centres[4, 5, 6, 7, 8, 9]. This is in part due to the fact that polarized x-rays offer advantages over, or complementary to, visible light. Firstly, within the validity of the single-particle picture, the description of magnetic dichroism spectra is simplified in that the initial state is a core level instead of an occupied valence state, making testing of relativistic bandstructure calculations much more straightforward. Secondly, the greater penetration of x-rays allow dichroism experiments on materials not transparent in the visible.

For magnetism, the most important orbitals are the 3d and 4f orbitals. Since MCD spectra are proportional to the magentic moment[42, 86] these orbitals preferentially should be probed with CPSR. However, the edges that do directly involve these orbitals lie in the soft x-ray range, where a number of experimental problems (notably the polarizing characteristics of crystal monochromators) make the out-of-plane CPSR hard to use.

Since no other circularly polarized x-ray sources exist to date, the experiments described in this thesis had to be performed with linearly polarized x-rays. As the results show, even then very interesting experiments are possible, but a full deployment of the possibilities of soft x-ray magnetic dichroism has to await the construction of insertion devices producing x-rays with any degree of ellipticity.

Chapter 3

THEORY OF 3d X-RAY DICHROISM OF RARE EARTH MATERIALS

3.1 Introduction

As was shown in the previous chapter, x-ray dichroism, in particular magnetic x-ray dichroism, has been found in systems which have electronic structures that cover the range between fairly itinerant (Fe) and completely localized (rare earths). For the description of dichroism one has the choice from many different theoretical approaches.

The atomic model approach has been quite succesful in describing the 3d XAS spectra of rare earths and other localized systems, as has been shown in many studies performed over the past two decades[27, 87, 88, 89, 90, 91, 92, 29]. Analysis of spectra with this model has been used succesfully to study a diversity of ground state effects, such as the relative population of spin-orbit-split ground-state levels of Ce[93] and determination of the occurence of the valencies of Tb in corrosion protection layers. Extentions of the atomic model to impurity models that allow the description of hybridization effects have been very succesful for Ce, Ce compounds and other mixed valent compounds[31, 94, 95, 96, 97, 98, 33, 99].

In this chapter the atomic description of the 3d→4f x-ray absorption spectra is discussed briefly with emphasis on details relevant for dichroism effects. The results of atomic calculations for the $T = 0$ K linear- and circular magnetic dichroism spectra for all ions of the rare earth series are presented, along with predictions for the temperature, magnetization and polarization angle dependencies. Part of the material on linear magnetic dichroism has been published elsewhere[100]

Crystal fields also can lead to dichroism, or, in magnetically ordered materials, influence the magnetic dichroism. We briefly investigate the more complicated description in this case. In many cases a complete prediction of the spectra from crystal field calculations is impossible. In the last section a simple semi-empirical model is presented which allows a partial interpretation for such cases.

Since the start of this work two different approaches have been described. The single particle bandstructure picture was used by Ebert *et al.* [51, 80], using a relativistic bandstructure program, to account for the dichroism found in the L edge XAS spectra of Fe[77] and Pt dissolved in Fe. Very recently Jo and Imida[34, 84] have presented calculations of the dichroism of the 3d and 4d edges of Ce compounds based on a single site Anderson impurity model[33, 99]. Furthermore, Carra and Altarelli have presented a general formulation of linear and circular dichroism in the absorption of x-rays in magnetically ordered systems, concentrating on the operator part of the transition matrix elements.

3.2 The Atomic Description of 3d-XAS of Rare Earth Materials

In the atomic picture the 3d→4f absorption process involves the electronic excitation $3d^{10}4f^{N} \rightarrow 3d^{9}4f^{N+1}$, where all other shells of the atom are either filled or empty. As discussed in connection with Fig. 2.4 both the initial- and the final configuration are split in multiplets of states with energies $E_{\alpha J}$ and wavefunctions denoted by $|\alpha JM\rangle$ (α labels all other quantum numbers aside from J and M needed to completely specify the state). The final-state configuration $3d^{9}4f^{N+1}$ contains two open shells and consequently its multiplet is more complicated and in some cases consists of several thousands of levels $|\alpha' J' M'\rangle$ (primes indicate final-state quantumnumbers). The strongest final-state multiplet interaction is the spin-orbit coupling of the 3d-hole, which splits the multiplet in two parts, which to a first approximation may be labeled $3d_{3/2}$ and $3d_{5/2}$ (or M_4 and M_5 respectively). In the x-ray absorption spectrum only those states of the excited multiplet are present that can be reached from the Hund's rule ground-state $|\alpha JM\rangle$ under the optical selection rules $\Delta J = 0, \pm 1$.

Transitions to the unoccupied np-continuum states are also allowed but have much smaller cross section compared to the 4f resonance, and lie at higher photon energies. The $3d_{5/2} \rightarrow n$p edge is visible in the spectra of the heavier rare earth as a weak step in between the $3d_{5/2} \rightarrow$4f and $3d_{3/2} \rightarrow$4f edges[29]. The difference in excitation energy between the 4f resonance and the continuum edge results from the very efficient screening of the hole by the $4f^{N+1}$ final state[28].

3.2.1 Calculation of atomic spectra

The theory of atomic spectra is quite involved, and it is impossible to give more than a rough outline of the procedure, which is discussed more completely in the books of Cowan[101] and Condon and Shortley[102]. We concentrate here on the angular part of the dipole matrix element that give rise to the dichroic effects

In the dipole approximation the absorption cross section of the transition from state $|\alpha JM\rangle$ of the ground-state level αJ to a state $|\alpha' J' M'\rangle$ of the level $\alpha' J'$ is given by

$$\sigma_{\alpha JM\to\alpha' J' M'}(\omega) = 4\pi^2\alpha_0\hbar\omega \sum_q \left|\left\langle \alpha JM \left| \mathsf{P}_q^{(1)} \right| \alpha' J' M' \right\rangle\right|^2 \delta(E_{\alpha J} - E_{\alpha' J'} + \hbar\omega) \tag{3.1}$$

where $\mathsf{P}_q^{(1)}$ is the q-th component of the classical dipole moment. The total spectrum is obtained by summing over all possible final states $\alpha' J'$. Application of the Wigner-Eckart theorem allows separation of the angular and radial parts of the matrix element of eq. (3.1), giving for the transition rate [101, 2]

$$\sigma_{\alpha JM\to\alpha' J' M'}(\omega) = 4\pi^2\alpha_0\hbar\omega \mathsf{S}_{\alpha J\alpha' J'} \sum_q \begin{pmatrix} J & 1 & J' \\ -M & q & M' \end{pmatrix}^2 , \tag{3.2}$$

where $\mathsf{S}_{\alpha J\alpha' J'} = |\langle \alpha J \| \mathbf{P} \| \alpha' J' \rangle|^2$ is the square of the reduced matrix element of the dipole operator $\mathbf{P}$, also known as the *linestrength* of the transition.

The term between the big brackets is the square of the Wigner 3-j symbol which dictates the distribution of the linestrength of the $\alpha J \to \alpha' J'$ line over its different $M \to M'$ components. The 3-j symbol is non-zero only if $\Delta J = 0, \pm 1$ ($J = J' = 0$ excluded) and if $q = -\Delta M \equiv M - M' = 0, \pm 1$. Transitions with $q = 0$ can be excited only by radiation that has a linearly polarized component along the z-axis (*i. e.* the quantization axis) of the atom— and $q = \pm 1$ transitions only by components that are left-, respectively right-handed circularly polarized in the xy-plane[102].

The 3-j symbols are subject to a number of sum rules; for instance summing eq. (3.2) over the $2J+1$ degenerate levels gives $|\alpha JM\rangle$

$$\sigma_{\alpha J\rightarrow\alpha' J'}(\omega) = 4\pi^2\alpha_0\hbar\omega\frac{1}{2J+1}S_{\alpha J\alpha' J'} \tag{3.3}$$

The calculations of the atomic multiplets were performed with a computer program by R.C. Cowan, which is described in his book[101] and article[104]. The program employs Hartree-Fock theory with relativistic corrections. Configuration interaction and solid state effects were included by reducing the Hartree-Fock values for the Slater electronic and exchange integrals to 80% of their calculated value. These reductions were found to give good agreement with experimental 3d-XAS data of the early rare earths[29]. For the second half of the series they give slightly too wide spectra, although the general shape is is obtained quite well. Numerical values of the HF parameters can be found in Table I of Thole *et al.* [29].

3.2.2 Calculated 3d-XAS spectra

In Fig. 3.1 we give the calculated 3d spectra of the $J=0$ ions La^{3+} and Eu^{3+}, as were obtained by Thole *et al.* [29]. The sticks give the relative sizes of the linestrengths of each $\alpha J \rightarrow \alpha' J'$ dipole transition. They have been broadened with Gaussian and Lorentzian curves simulating the instrumental resolution and the 3d core-hole lifetime to yield the full curve. As was proven by Thole *et al.* [29] such calculations match the experimental spectra exceedingly well for all the trivalent rare earth. The most notable exception is Sm^{3+}. This is thought to be due to the small splitting of the ground state to the first excited state in the multiplet, which allows them to be mixed by crystal field interactions[105].

In Fig. 3.2, top panel, we reproduce the calculated spectra for all trivalent rare earth ions with non-$J=0$ ground-states. Instead of the stick spectra we now show the decomposition of the spectra into the contributions from the three possible values of $\Delta J = 0, \pm 1$. Note that each group forms a readily distinguishable contribution to the total spectra; in the first half of the rare earth period especially in the M_4 part (right), and in the second half in the M_5 part (left). Clear exceptions are the $J=0$ La^{3+} and Eu^{3+} ions, where $\Delta J = 1$ is the only available channel. In Gd^{3+}, an f^7 ion, the splitting between the ΔJ components is small, due to the orbital singlet

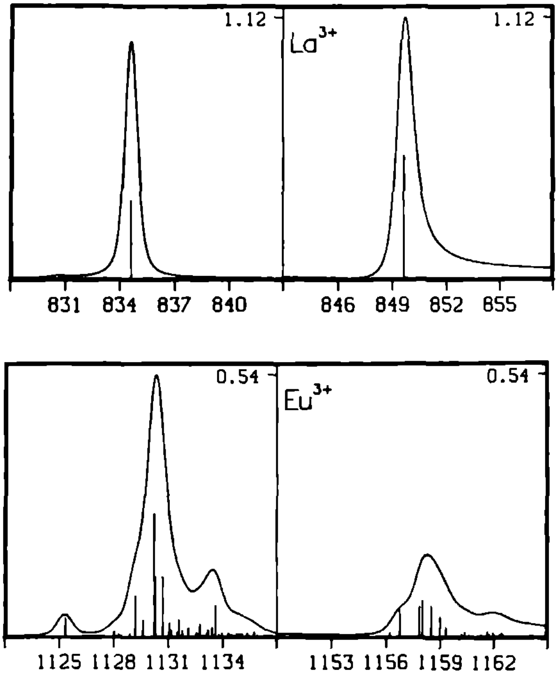

Figure 3.1: Atomic calculations of spectra of the $3d_{5/2}$ (left) and $3d_{3/2}$ x-ray absorption edges of the $J = 0$ ions La^{3+} and Eu^{3+}. The sticks represent the relative strengths of the allowed dipole transitions ($\Delta J = 1$ only). The full curve is the lifetime and resolution broadened spectrum. The indicated maximum cross section is in Å^2.

($L = 0$) ground- state, and as a result especially the linear dichroism effects are correspondingly small.

In the other elements it is because of this distinguishability of the ΔJ partial spectra that dichroic effects can be observed, because, as will be shown below, each ΔJ group turns out to have its own dependence on temperature and polarization.

Since the shape of the multiplets is dependent only on the total number of f-electrons, spectra like the above can also be calculated for other valencies, *i. e.* the spectra of Eu^{2+} and Tb^{4+} have roughly the same shape as Gd^{3+}, although they appear of course at a different photon energy[106].

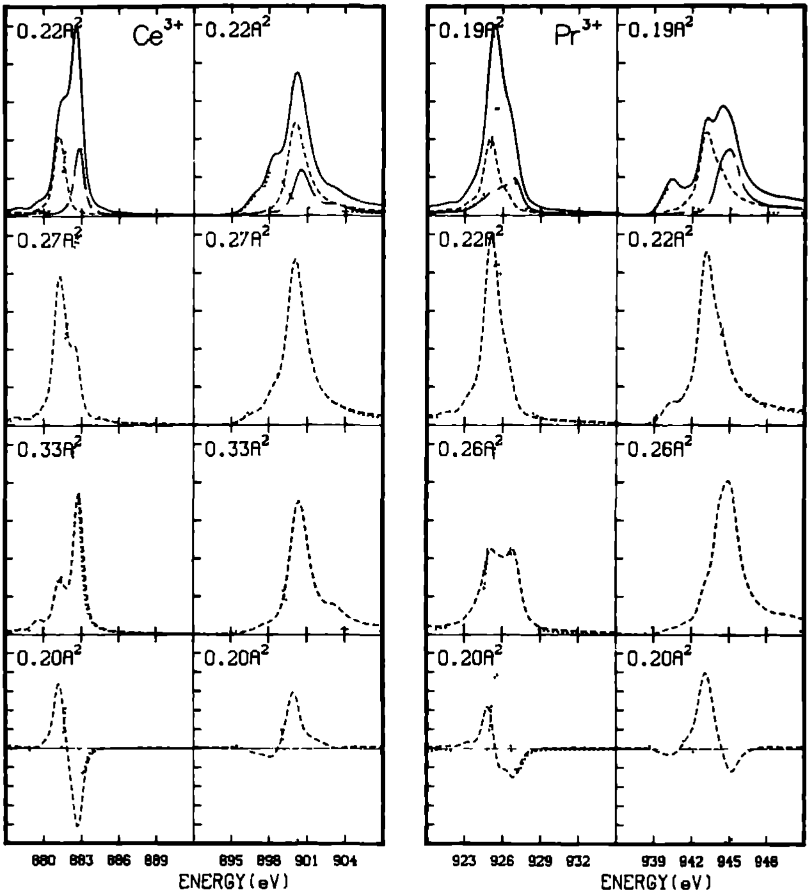

Figure 3.2: Atomic calculations of the $3d_{5/2}$ (left) and $3d_{3/2}$ x-ray absorption edges of trivalent rare earth ions.
Top panel: the unpolarized spectrum and the partial spectra with $\Delta J = -1$ (dash-dot), 0 (dashes) and 1 (dots). All cross sections in $Å^2$.
Second panel: Predicted linear magnetic dichroism spectra at $T = 0$ K for parallel (dash) and perpendicular (dots) polarizations.
Third panel: Same for left (dots) and right (dash) circular polarizations.
Bottom panel: Difference spectra of the curves in the second (dash) and third (dots) panels

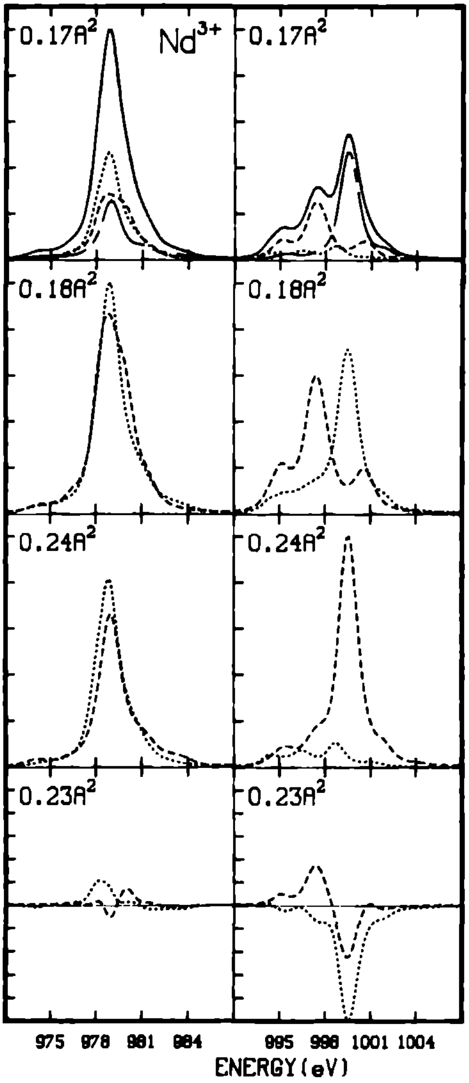
0.17A^2
Nd^{3+}
0.17A^2
0.18A^2
0.18A^2
0.24A^2
0.24A^2
0.23A^2
0.23A^2
975
978
981
984
995
998
1001
1004
ENERGY(eV)

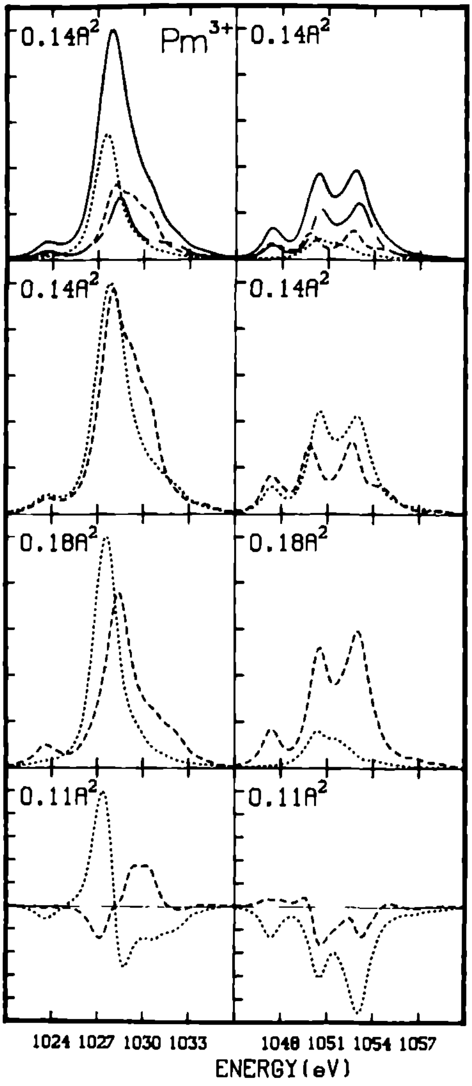
0.14A^2
Pm^{3+}
0.14A^2
0.14A^2
0.14A^2
0.18A^2
0.18A^2
0.11A^2
0.11A^2
1024
1027
1030
1033
1048
1051
1054
1057
ENERGY(eV)

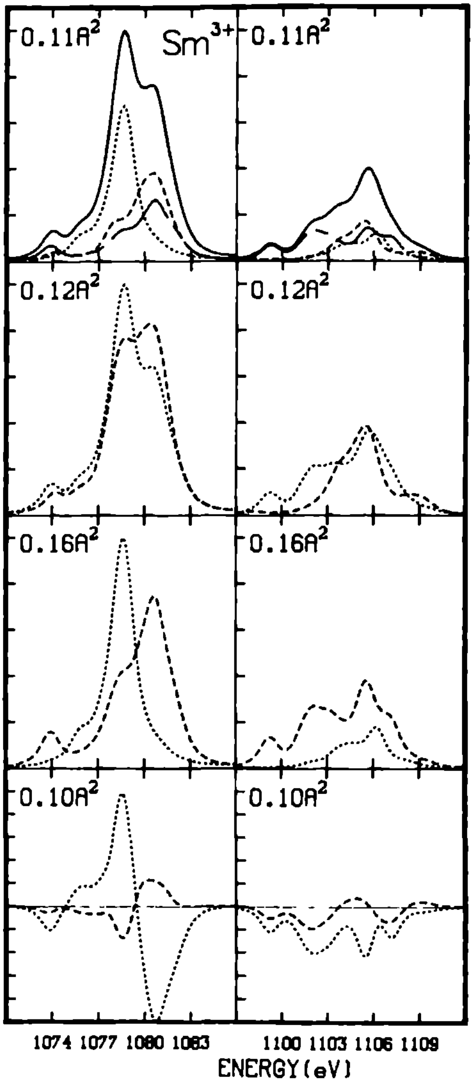
Sm^{3+}
0.11Å^2
0.11Å^2
0.12Å^2
0.12Å^2
0.16Å^2
0.16Å^2
0.10Å^2
0.10Å^2
1074 1077 1080 1083
1100 1103 1106 1109
ENERGY(eV)

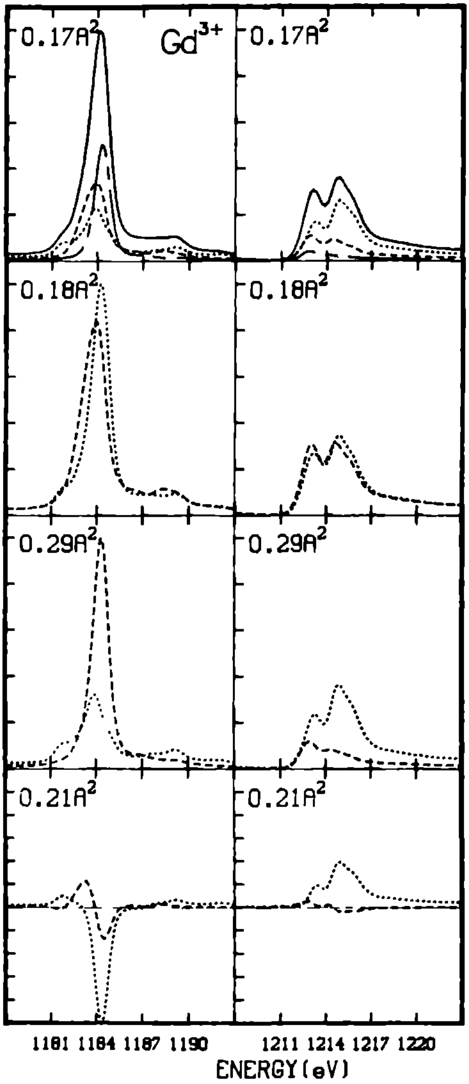
Gd^{3+}
0.17Å^2
0.17Å^2
0.18Å^2
0.18Å^2
0.29Å^2
0.29Å^2
0.21Å^2
0.21Å^2
1181 1184 1187 1190
1211 1214 1217 1220
ENERGY(eV)

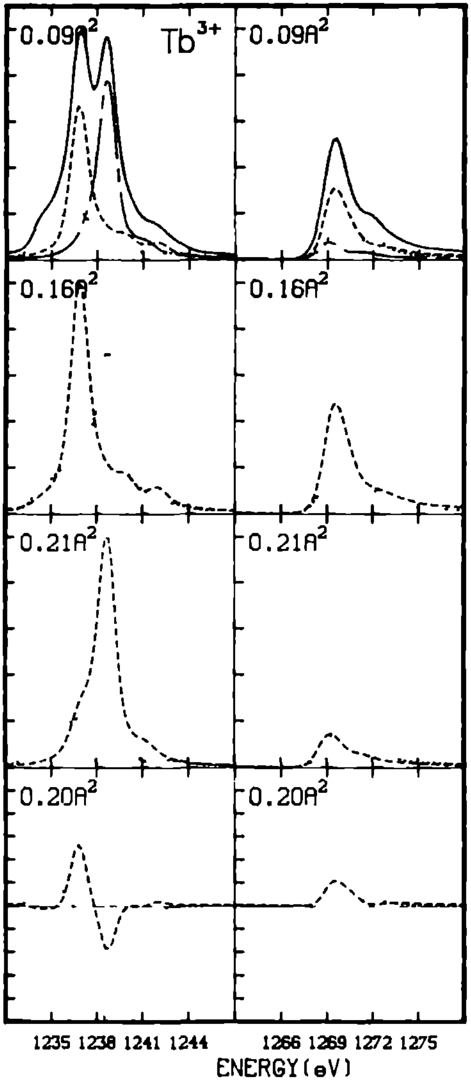
Tb^{3+}
0.09Å^2
0.09Å^2
0.16Å^2
0.16Å^2
0.21Å^2
0.21Å^2
0.20Å^2
0.20Å^2
1235 1238 1241 1244
1266 1269 1272 1275
ENERGY(eV)

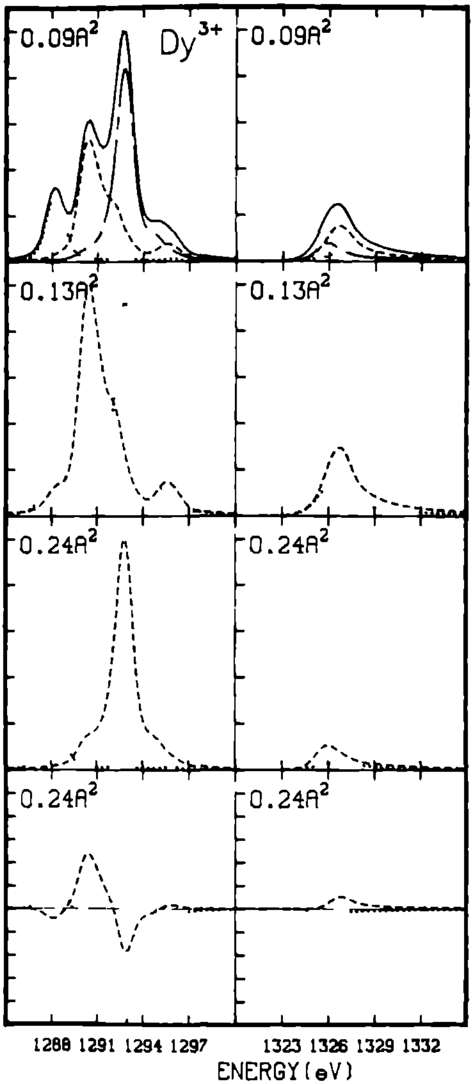
Dy^{3+}
0.09Å^2
0.09Å^2
0.13Å^2
0.13Å^2
0.24Å^2
0.24Å^2
0.24Å^2
0.24Å^2
1288 1291 1294 1297
1323 1326 1329 1332
ENERGY(eV)

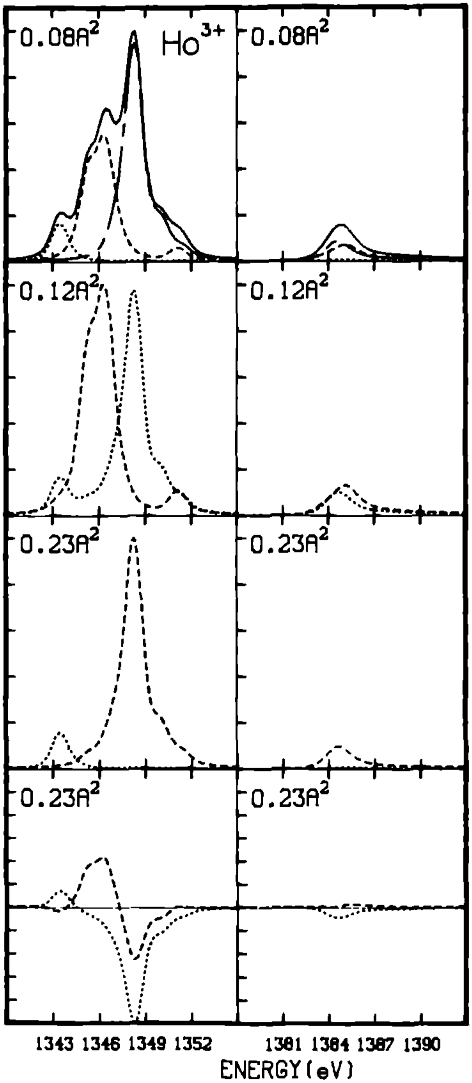
0.08A²
Ho³⁺
0.08A²
0.12A²
0.12A²
0.23A²
0.23A²
0.23A²
0.23A²
1343 1346 1349 1352
1381 1384 1387 1390
ENERGY(eV)

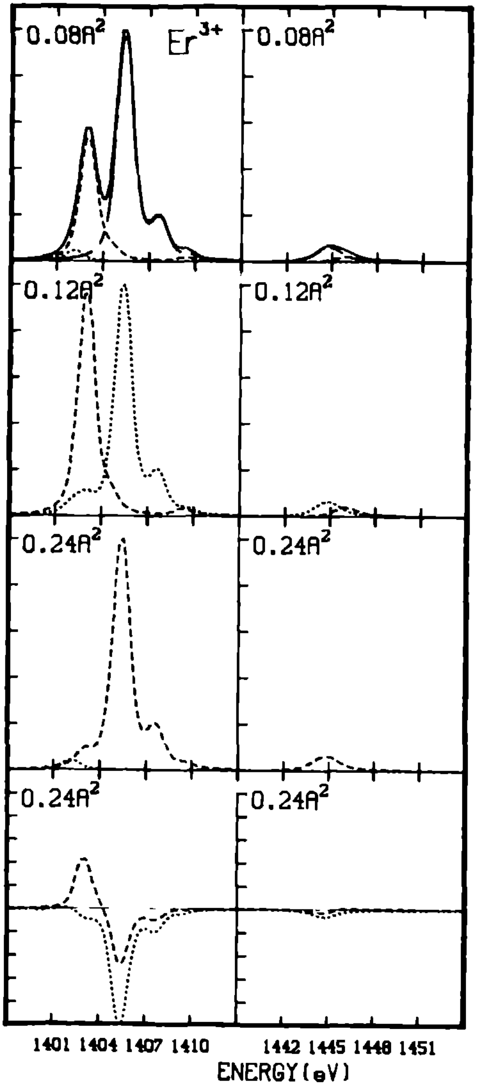
0.08A²
Er³⁺
0.08A²
0.12A²
0.12A²
0.24A²
0.24A²
0.24A²
0.24A²
1401 1404 1407 1410
1442 1445 1448 1451
ENERGY(eV)

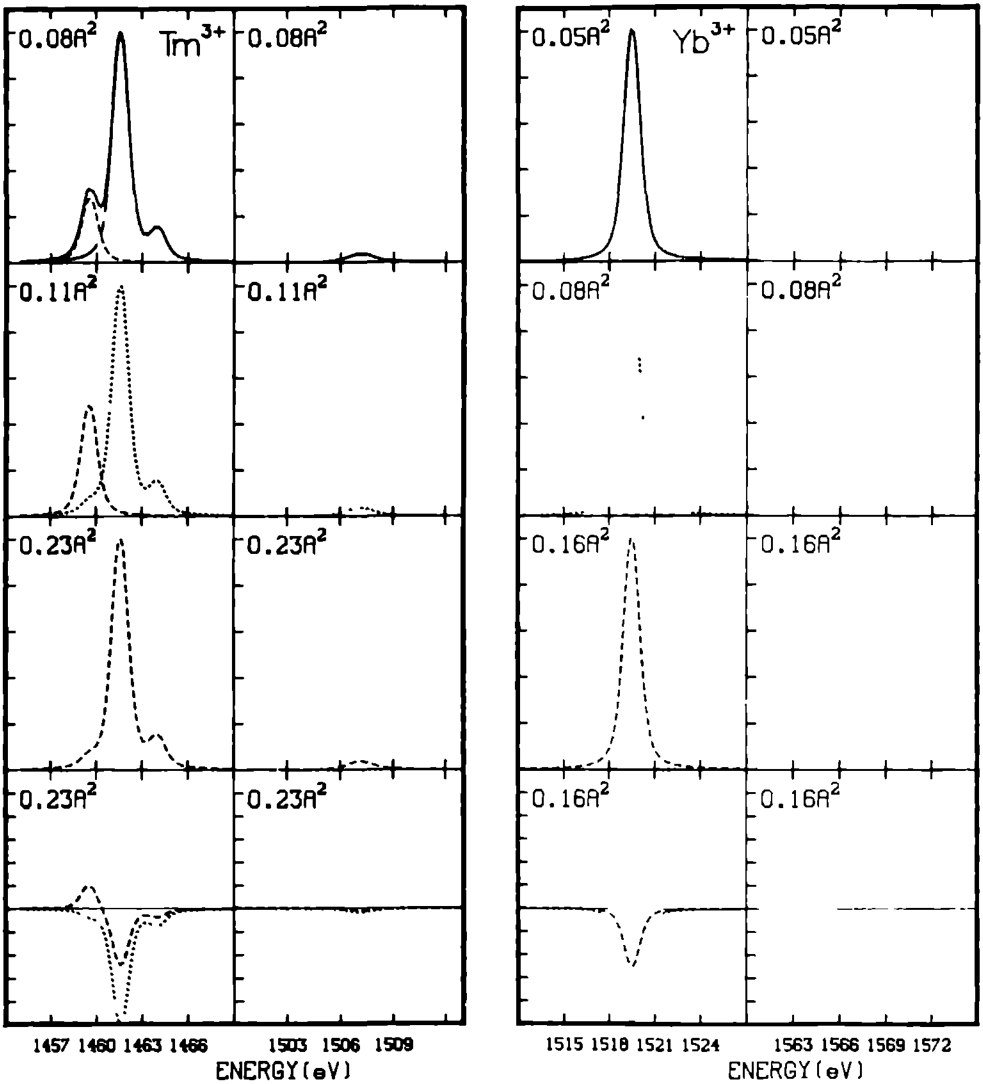
0.08A²
Tm³⁺
0.08A²
0.11A²
0.11A²
0.23A²
0.23A²
0.23A²
0.23A²
1457 1460 1463 1466
1503 1506 1509
ENERGY(eV)
0.05A²
Yb³⁺
0.05A²
0.08A²
0.08A²
0.16A²
0.16A²
0.16A²
0.16A²
1515 1518 1521 1524
1563 1566 1569 1572
ENERGY(eV)

3.3 3d X-ray Dichroism of Rare Earths

Dichroism occurs in atomic spectra when the spherical symmetry of the free atom is broken. For rare earth ions in solids the symmetry breaking field can be *magnetic* or *electric* in origin, and can be *applied* or *internal* to the solid, (*e. g.* molecular magnetic fields or crystalline electric fields). Whatever the origin of the field may be, the result is invariably a partial lifting of the degeneracy of the 4f sublevels $|\alpha JM\rangle$, since the electron orbits adapt themselves to the new potential. The net effect is a change of the shape of the 4f electron cloud, for instance in the case of a magnetic field, the spherical cloud is either compressed or elongated in the direction of the field. In the case of crystal fields the deformation can be much more complicated.

The 4f levels of the rare earth elements have small expectation radii and are well screened by the surrounding valence electrons. To a first approximation therefore, crystal fields may often be neglected. Moreover, the ions with a $L = 0$ configuration, Eu^{2+}, Gd^{3+} and Tb^{4+}, are never strongly affected by crystal fields since the crystal field potential does not act on the spin part of the electronic wavefunctions. In the following section we will first assume crystal fields can be neglected completely. As we will see, in this approximation the size and direction of the magnetic moment can be obtained from the measured dichroism spectra. In section 3.4 we will show this is no longer true when crystal field effects are important, unless certain assumptions are made.

3.3.1 Magnetic X-ray Dichroism, MXD

In a magnetic field $\mathbf{H}$ the states $|\alpha JM\rangle$ of both the initial- and final levels shift from their non-perturbed positions by an energy

$$E_M = \mu \mathbf{H} \cdot \langle \alpha JM \, | \mathbf{L} + g_0 \mathbf{S} | \, \alpha' J' M' \rangle \,, \tag{3.4}$$

where g_0 is the electronic splitting factor, and the matrix element is the atomic moment of the sublevel $|\alpha JM\rangle$. Application of the Wigner-Eckhart theorem gives the well-known Zeeman energies

$$E_M = -\mu g_{\alpha J} \mathbf{H} M, \tag{3.5}$$

where $g_{\alpha J}$ is the intermediate-coupling spectroscopic splitting factor[107, 101].

	$q=0$	$q=\pm1$
A^q_{JJ+1}	$\frac{(J+1)^2-\langle M^2\rangle}{(2J+3)(J+1)(2J+1)}$	$\frac{(J+1)(J+1)\mp(2J+3)\langle M^2\rangle+\langle M^2\rangle}{2(2J+3)(J+1)(2J+1)}$
A^q_{JJ}	$\frac{\langle M^2\rangle}{J(J+1)(2J+1)}$	$\frac{J(J+1)\pm\langle M\rangle-\langle M^2\rangle}{2J(J+1)(2J+1)}$
A^q_{JJ-1}	$\frac{J^2-\langle M^2\rangle}{J(2J-1)(2J+1)}$	$\frac{J(J-1)\pm(2J-1)\langle M\rangle+\langle M^2\rangle}{2J(2J-1)(2J+1)}$

Table 3.1: The expressions for the factors $A^q_{JJ'}$ giving the intensity of $\Delta J = 0, \pm 1$ transitions for different values of $q \equiv M' - M$.

The primary effect on the spectrum is that each transition $|\alpha J M\rangle \rightarrow |\alpha' J' M'\rangle$ will be shifted in energy by a small amount $\mu(g_{\alpha J} - g_{\alpha' J'})$. The maximum observed Zeeman splittings, such as occur in ferromagnetic materials, are of the order of 10 meV. Such splittings are two orders of magnitude smaller than the lifetime and experimental linewidths and thus not directly observable.

However, a second effect of the magnetic splitting is that the occupation of the Zeeman levels will be temperature dependent. This can be included by taking the Boltzmann weighted average of eq. (3 2), giving

$$\sigma_{\alpha J \rightarrow \alpha' J'}(\omega) = 4\pi^2 \alpha_0 \hbar\omega S_{\alpha J \alpha' J'} \sum_q A^q_{JJ'}, \tag{3.6}$$

with

$$A^q_{JJ'} = \frac{\sum\limits_M \begin{pmatrix} J & 1 & J' \\ -M & q & M' \end{pmatrix}^2 e^{-M/\Theta}}{\sum\limits_M e^{-M/\Theta}} \tag{3.7}$$

where $\Theta = kT/\mu g_{\alpha J} H$ is the reduced temperature.

The $A^q_{JJ'}$ give the temperature dependence of the absorption strength for each of the nine combinations of ΔJ and q. By writing out the 3-j symbols in their analytic form[108, 101] the $A^q_{JJ'}$ can be written in terms of the expectation values $\langle M\rangle$ and $\langle M^2\rangle$. The resulting expressions are given in Table 3.1.

$\langle M\rangle$ is related to the magnetic moment $\mathbf{M}$ of the ion by $\langle M\rangle = |\mathbf{M}|/\mu g_{\alpha J}$. By evaluating the thermal average of the matrix element in eq. (3.4) one obtains

$$\langle M\rangle = \frac{\sum_M M e^{-M/\Theta}}{\sum_M e^{-M/\Theta}} = -J B_J(J/\Theta), \tag{3.8}$$

where $B_J(J/\Theta)$ is the Brillouin function[107] and likewise

$$\langle M^2 \rangle = \frac{\sum_M M^2 e^{\;M/\Theta}}{\sum_M e^{-M/\Theta}} = J(J+1) + \langle M \rangle \coth \frac{1}{2\Theta}. \tag{3.9}$$

The $A^q_{J\,J+\Delta J}$ can be conveniently plotted as a function of the reduced temperature. For the trivalent rare earth ions we need to consider only ground-states with $J = 5/2$, $7/2$, 4, $9/2$, 6, $15/2$ and 8. For these values the $(2J+1)A^q_{JJ'}$ are plotted in Fig. 3.3 for all q. It is evident from these curves that each $J \rightarrow J'$ transition has an unique dependence on polarization (q) and effective temperature (Θ). From Fig. 3.3 one sees that at $\Theta = 0$ the matrix $A^q_{JJ'}$ is triangular in q and J, and becomes almost diagonal for large J, i. e. a transition with a particular ΔJ has approximately $\Delta M = \Delta J$. On the other hand, for $\Theta \rightarrow \infty$ the intensity of each of the ΔJ channels approach the statistical value $1/3(2J+1)$ and we retrieve the unpolarized spectrum.

In order to give an impression of the size of the maximum magnetic dichroism effect we give in Fig. 3.2, second panel, the normalized $\Theta = 0$ spectra for parallel and normal linear polarizations. In the third panel the left- and right circularly polarized spectra are given. The bottom panel gives the difference curves for both cases.

With the above formula the magnetic dichroism can be predicted extremely simply. For instance, with right circularly polarized x-rays, incident along the direction of the magnetic field, only transitions with $q = -1$ are possible. The spectrum then is obtained by adding the three ΔJ components given in Fig. 3.3 top panel, weighted by the factors $A^1_{J\,J+\Delta J}(\Theta)$. The only input required is the effective temperature Θ and the J-value of the groundstate.

3.3.2 Angular dependence

In order to obtain the spectrum at any angle we take a closer look at the matrix element in eq. (3.1). In the coordinate representation the matrix element of the dipole operator can be written as[20]

$$\langle \alpha J \,|\mathbf{r} \cdot \mathbf{e}|\, \alpha' J' \rangle = \frac{4\pi}{3} \sum_q (-1)^q \langle \alpha J \,| r Y_1^q(\mathbf{r}) |\, \alpha' J' \rangle \, Y_1^{-q}(\mathbf{e}), \tag{3.10}$$

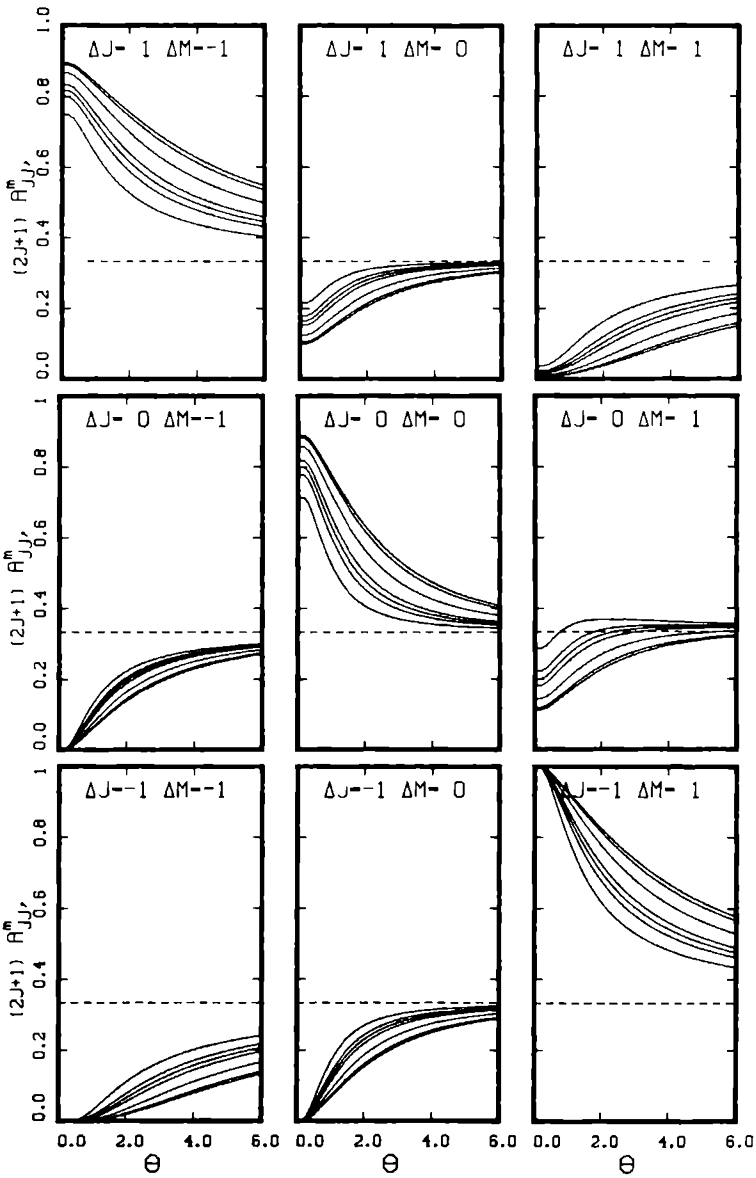

Figure 3.3: The dependence of the cross section of the three partial spectra $\Delta J = 0, \pm 1$ on the effective temperature $\Theta = kT/\mu g_{\alpha J} H$ for $q \equiv -\Delta M = 1, 0, -1$ transitions. At high Θ all curves converge to 1/3 (dashed horizontal line). From that line outward one finds the curves for the Hund's rules ground-states $J = \frac{5}{2}, \frac{7}{2}, 4, \frac{9}{2}, 6, \frac{15}{2}$ and 8.

$F_q(\mathbf{e})$	$q = 0$	$q = \pm 1$
linear, $\mathbf{e} = \mathbf{x}$	$\cos^2\phi \sin^2\theta$	$\cos^2\phi \cos^2\theta + \sin^2\phi$
circular, $\mathbf{e} = 1/\sqrt{2}(\mathbf{x} \pm i\mathbf{y})$	$\frac{1}{2}\sin^2\theta$	$\frac{1}{2}(1 \pm \cos^2\theta)$

Table 3.2: Angular dependence of the absorption cross section of $q = 0$ and $q = \pm 1$ transitions for linear and circular polarized light. The x-rays propagate along the z-axis. The direction of the polarization vector is given by the unit vector $\mathbf{e}$. θ and ϕ are the polar- and azimuthal angles of the field direction in the laboratory frame.

where $\mathbf{r}$ is the position operator, $\mathbf{e}$ is the (complex) polarization vector and Y_l^m are spherical harmonics. For arbitrary polarization therefore an extra factor $F_q(\mathbf{e})$ has to be included in the summation over q in eq. (3.7), given by

$$\begin{aligned} F_q(\mathbf{e}) &= \tfrac{4\pi}{3}\left|Y_1^{-q}\right|^2 \\ &= \cos^2\alpha \qquad q = 0 \\ &= \tfrac{1}{2}\sin^2\alpha \qquad q = \pm 1. \end{aligned} \tag{3.11}$$

where α is the polar angle of the polarization vector $\mathbf{e}$ in the spherical coordinate frame of the atom. In practice it is easier to use laboratory-frame coordinates, for which the F_q are given in Table 3.2.

3.3.3 Linear Magnetic X-ray Dichroism

For the edges discussed here only linearly polarized x-rays are experimentally available. In this case the expressions for the factors $A^q_{JJ'}$ can be substantially simplified. If we choose α to be the angle between the z-axis and the polarization direction, then the angular dependence of the spectrum is given by

$$A^0_{JJ'}\cos^2\alpha + \frac{1}{2}\left(A^1_{JJ'} + A^{-1}_{JJ'}\right)\sin^2\alpha. \tag{3.12}$$

From the orthogonality relations of the Wigner 3-j symbols[101], we have

$$A^1_{JJ'} + A^0_{JJ'} + A^{-1}_{JJ'} = \frac{1}{2J+1}, \tag{3.13}$$

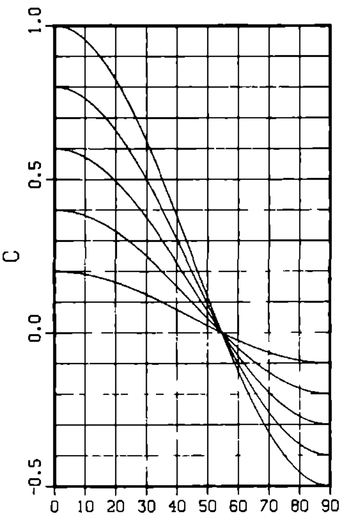

Figure 3.4: Angular dependence of the dichroism parameter C for $C_M = 0.2, 0.4, \cdots 1.0$.

so that the total angular- and temperature dependence of the spectrum can be written in terms of $A^0_{JJ'}$ only:

$$A^\alpha_{JJ'} = \frac{(1 + [3(2J+1)A^0_{JJ'} - 1]\, C_\alpha)}{3(2J+1)} \tag{3.14}$$

with

$$C_\alpha = \frac{3}{2}\cos^2\alpha - \frac{1}{2} \tag{3.15}$$

An important consequence is that with *linear* polarized x-rays, measurement of the dichroism does not give information on the *sign* of the magnetization, since from Table 3.1 we see the $A^0_{JJ'}$ do not contain terms proportional to $\langle M \rangle$.

The angular factor C_α, plotted in Fig. 3.4, vanishes at the magic angle 54.7°, so that the right-hand side of eq. (3.14) reverts to the statistical value $1/3(2J+1)$ and we recover the unpolarized spectrum.

From the expressions for $A^0_{JJ'}$ given in Table 3.1 we find

$$A^\alpha_{JJ+1} = \frac{1}{3(2J+1)}\left(1 - \frac{J(2J-1)}{(J+1)(2J+3)}C\right) \tag{3.16}$$

$$A^{\alpha}_{JJ} = \frac{1}{3(2J+1)}\left(1 - \frac{2J-1}{J+1}C\right) \tag{3.17}$$

$$A^{\alpha}_{JJ-1} = \frac{1}{3(2J+1)}(1+C) \tag{3.18}$$

where $C = C_{\alpha}C_M$, with

$$C_M = \frac{\langle M^2\rangle - \frac{1}{3}J(J+1)}{J^2 - \frac{1}{3}J(J+1)}. \tag{3.19}$$

Thus we see that the linear magnetic dichroism spectra are simply linearly dependent on a single parameter C, called the *linear dichroism parameter*, which is the product of factors that describe the angular dependence and the temperature- and magnetic field dependence. C_{α} varies between -0.5 and 1, and C_M between 0 and 1, so that also C varies between -0.5 and 1.

3.3.4 Circular Magnetic X-ray Dichroism

For completeness we give here the equations for the magnetic circular dichroism (MCD), defined as the difference in absorption of left and right circularly polarized beams. For a single line $J \to J'$

$$\Delta A_{JJ'} \equiv A^{1}_{JJ'} - A^{-1}_{JJ'} \tag{3.20}$$

From Table 3.1 we find

$$\Delta A_{J,J+1} = \frac{\langle M\rangle}{(J+1)(2J+1)} \tag{3.21}$$

$$\Delta A_{J,J} = \frac{\langle M\rangle}{J(J+1)(2J+1)} \tag{3.22}$$

$$\Delta A_{J,J-1} = \frac{\langle M\rangle}{J(J-1)(2J+1)} \tag{3.23}$$

These equation show the important result that, under the assumption that crystal fields can be neglected, the magnetic dichroism signal is directly proportional to the magnetic moment of the ion. The MCD spectra for saturation magnetization at $T = 0$ K, where $\langle M\rangle = -J$, are given the bottom panels of Fig. 3.2.

Note that an alternative method to obtain the MCD signal consists of alternating the direction of magnetization instead of the sense of the polarization. In this way it is even possible to measure the MCD signal with elliptically polarized light since the linear polarized part in the absorption cancels out.

3.4 Crystal-field X-ray Dichroism

For the rare earth 4f, electrons spin-orbit interaction is in the majority of cases stronger than the crystal field since the potential of the surrounding electrons is efficiently shielded by the more diffuse 5d and 6p orbitals (see *e. g.* Elliot[109]). Also the overlap between the 4f electrons and the surrounding atoms is negligible. Hence it is sufficient to treat the crystal field effects in the weak field limit of the point charge model[110, 67]. In this case one can disregard mixing of different atomic levels αJ by the crystal field interaction (J-mixing).

In the crystal field potential the atomic energy level αJ splits up in states which transform as irreducible representations Γ of the point group symmetry. The crystal field level scheme consists of states with energies $E_\imath$ and wavefunctions $|\alpha J\Gamma\imath\rangle$ ($\imath$ labels different states that belong to the same irreducible representation) that can be written as linear combinations of the atomic wavefunctions $|\alpha J, M\rangle$:

$$|\alpha J\Gamma\imath\rangle = \sum_{M} c_\imath(J, M)\,|\alpha JM\rangle\,, \tag{3.24}$$

with coefficients $c_\imath(JM)$ satisfying the normalization condition

$$\sum_{M} |c_\imath(JM)|^2 = 1. \tag{3.25}$$

The coefficients $c_\imath(JM)$ are independent of α, *ı. e.* all terms with the same J split up in the same irreducible representations of the point group and have the same crystal field expansion coefficients.

To obtain the crystal field spectrum the atomic wavefunctions $|\alpha JM\rangle$ in eq. (3.1) have to be replaced by the crystal field wavefunctions of eq. (3.24). By expanding the latter as in eq. (3.24) we obtain

$$\left|\left\langle \alpha J\Gamma\jmath \left| \mathsf{P}_q^{(1)} \right| \alpha' J'\Gamma'\imath \right\rangle\right|^2 \tag{3.26}$$

$$= \sum_{M,M'} |c_i^\star(JM)c_j(J'M')|^2 \left|\left\langle \alpha JM \left| \mathsf{P}_q^{(1)} \right| \alpha' J'M' \right\rangle\right|^2 \tag{3.27}$$

$$= \mathsf{S}_{\alpha J\alpha' J'} \sum_{M,M'} |c_i^\star(JM)c_j(J'M')|^2 \begin{pmatrix} J & 1 & J' \\ -M & q & M' \end{pmatrix}^2 \tag{3.28}$$

where in the last step again the Wigner-Eckhart theorem has been used. In the weak crystal field limit, the splitting of the free-atom spectral lines is again too small to be observed directly, and is expressed only as a temperature and polarization depependence of the cross section of these lines. Taking as before the Boltzmann weighted average over all crystal field levels originating from the atomic level αJ, and summing over all crystal field levels originating from the final level $\alpha' J'$ we obtain

$$\sigma_{\alpha J\to\alpha' J'}(\omega) = 4\pi^2\alpha_0\hbar\omega \mathsf{S}_{\alpha J\alpha' J'} \sum_q B^q_{JJ'}(T), \tag{3.29}$$

where

$$B^q_{JJ'}(T) = \frac{\sum\limits_{i,j,M,M'} |c_i^\star(JM)c_j(J'M')|^2 \begin{pmatrix} J & 1 & J' \\ -M & q & M' \end{pmatrix}^2 e^{-E_i/kT}}{\sum\limits_{i,j,M,M'} |c_i^\star(JM)c_j(J'M')|^2 e^{-E_i/kT}}. \tag{3.30}$$

Since the crystal field splitting of a term depends on J only, all terms $\alpha' J'$ split up in the same way. Thus completely analogous to the magnetic case discussed above, all $J \to J'$ transition have the same temperature dependence. Again the 3-j symbol can be substituted by the analytical forms, yielding exactly the same equations as given in Table 3.1; however, the terms $\langle M\rangle$ and $\langle M^2\rangle$ now have to be replaced by

$$\langle M^p\rangle = \frac{\sum\limits_{i,j,M,M'} M^p |c_i^\star(JM)c_j(J'M')|^2 e^{-E_i/kT}}{\sum\limits_{i,j,M,M'} |c_i^\star(JM)c_j(J'M')|^2 e^{-E_i/kT}} \quad (p = 1, 2) \tag{3.31}$$

The simulation of the crystal field dichroism spectra involves the evaluation of the matrix $|c_i^\star(JM)c_j(J'M')|^2$. In cases of sufficiently high symmetry this matrix is completely determined by the point group symmetry, *i. e.* no knowledge of the strength of the crystal field is necessary. In cases where the point group is known to fullfill this condition it is in principle possible to obtain information on the crystal field energies E_i from measurements of the temperature dependence of the dichroic spectra. By least-squares fitting the three ΔJ components to the measured dichroism spectra the temperature dependence of the $B^q_{JJ'}$ can be obtained, from which in turn the energy splittings E_i can be obtained by fitting those curves with eq. (3.30). As a trivial example one could obtain the $10D_q$ splitting of the 3d orbitals of transition metals in a cubic field (O_h-symmetry).

In general however, it will be very difficult to extract information on the crystal structure without making important simplifications. One possible simplification is the neglect of the final state crystal field splitting. In that case the final state crystal field coefficient matrix $c_j(J'M')$ would reduce to $\delta_{j,M'}$, so that the expressions eq. (3.31) would contain only initial state crystal field parameters. The resulting $\langle M \rangle$ is just the magnetic moment in a crystalline field and can be obtained directly from the MCD without knowing the details of the crystal field splittings. At this point it is unclear whether the above assumption is valid.

We conclude this section by remarking that in general the Hamiltonian of magnetic materials will contain both crystal field and magnetic perturbations. In such cases the splitting of the sublevels will be more difficult to calculate, but the crystal field formulae given above remain valid.

3.5 Linear MXD Spectra of Non-collinear Magnetic Moments

Many ordered magnetic systems, especially those containing rare earth elements, exhibit non-collinear spin structures, *i. e.* spiral- or umbrella structures[111]. The occurence of such structures indicates crystal fields and/or anisotropic exchange may be important[109]. However. as discussed in the previous section, a description in terms of a Hamiltonian including these effects is often quasi-impossible.

In such cases, to a first approximation the dichroism spectra can often be described in terms of a collection of atomic-like moments with artificially fixed directions. The necessary information has to be obtained from other sources, for instance neutron scattering, or by assuming some model distribution. In this section we will analyze the interpretation of MXD spectra in terms of this model, and we derive values of the linear dichroism parameter for a number of modeled canted magnetic structures, with the objective to gain insight into the possibilities to characterize them with MXD.

We will work in a polar coordinate system which has its z-axis along a main symmetry axis of the system, *e. g.* the direction of the macroscopic magnetization **M**. Let (θ_0, ϕ_0) be the direction of the linear polarization vector **e** with respect to this coordinate system and (θ_i, ϕ_i) the direction of the moment $\mathbf{m}_i$ ($|\mathbf{m}_i| = g\mu\langle M\rangle$) of the ion i, and let $N(\theta_i, \phi_i)$ be the normalized angular distribution function of the moments. Then the magnetization is given by

$$\mathbf{M} = \sum_i N(\theta_i, \phi_i) m_i \cos\theta_i \tag{3.32}$$

Furthermore, let $\alpha_0 \equiv \theta_0$ be the angle between **e** and **M**, and let α_i be the angle between **e** and $\mathbf{m}_i$, with

$$\cos\alpha_i = \sin\theta_0 \sin\theta_i \cos(\phi_0 - \phi_i) + \cos\theta_0 \cos\theta_i, \tag{3.33}$$

The contribution to the spectrum by each moment then is given by eq. (3.16) using the angular factor C_{α_i}. The total spectrum therefore is given by the same equations, except that C_α has to be replaced by the angular averaged value

$$C(\mathbf{e}) = \sum_i C_{\alpha_i} N(\theta_i, \phi_i). \tag{3.34}$$

Often the magnetization is a direction of axial symmetry and the contribution to the spectra of the components of the magnetic moments normal to the magnetization are averaged out, so that we obtain

$$C(\mathbf{e}) = C_\alpha C_N, \tag{3.35}$$

where

$$C_\alpha = \frac{3}{2}\cos^2\alpha - \frac{1}{2}, \tag{3.36}$$

and

$$C_N = \frac{3}{2}\sum_i C_{\alpha_i} N(\theta_i, \phi_i) - \frac{1}{2}. \tag{3.37}$$

The linearly polarized spectrum of the collection of moments is therefore given by a linear dichroism parameter C composed of three factors: $C = C_M C_\alpha C_N$. The first two factors are the same as for a single ion as discussed in section 3.3.3, while the last factor gives the size of the effective moment of the system , ranging form 0 for a completely isotropical distribution to 1 for a (anti)ferromagnetically ordered system. We will consider some special distributions in more detail.

- Umbrella structure
  This structure is found in a large number of rare earth systems. The atomic monents lie on a cone arround the direction of magnetization, with $\theta_i = \beta$, $\phi_i = i\frac{\pi}{N}$ $(i = 1 \cdots N)$, and thus

  $$C_N \equiv C_\beta = \frac{3}{2}\cos^2\beta - \frac{1}{2}, \tag{3.38}$$

  In chapter 6 this model is app[lied to the MXD of Tb iron garnets.

- Continuous distributions of spin directions
  This class of models is used to describe the magnetic structure of amorphous rare earth-transition metal alloys[112, 113]. Here the transition metal is assumed to be ferromagnetically ordered while the rare earth moments have some distribution of spin directions that yields a net magnetic moment along the ordering axis of the transition metal. We consider three cases:

Isotropical hemisphere distr.:	$N(\theta) = \frac{2}{\pi}$	$(0 \leq \theta < \frac{\pi}{2})$	$C_N = \frac{1}{4}$
Cosine distr.:	$N(\theta) = \cos\theta$	$(0 \leq \theta < \frac{\pi}{2})$	$C_N = \frac{1}{2}$
Cosine square distr.:	$N(\theta) = \frac{4}{\pi}\cos^2\theta$	$(0 \leq \theta < \frac{\pi}{2})$	$C_N = \frac{5}{8}$

From a comparison of the range of C_β-values that is possible with the umbrella structure we see that it may not be possible to distinguish this structure from the continuous models with the same C. On the other hand, the results show linear MXD measurements can distinguish between different continuous models.

3.6 Discussion

We conclude this chapter with some remarks on the accuracy of the approach used here and the approximations made in it.

Spin-orbit coupling is in origin a relativistic effect, and the fullest description of atomic structure would involve solving the Dirac equation. However, in most practical atomic problems, and in the calculations used here, relativistic effects are treated as perturbations to the non-relativistic Schrödinger equation. Specifically, instead of the spin- dependent radial wave functions $P_{nlj}(r)$, the functions $P_{nl}(r)$ of the non-relativistic solution are used.

This has direct bearing on the calculation of dichroic effects. As was predicted by Fano[81], photoelectrons with circularly polarized light excited from s levels of free atoms into the unoccupied p states can be highly polarized, with a degree of polarization that depends on their kinetic energy. This phenomenon, which is the basis for the explanation of magnetic x-ray dichroism in the picture of Schütz *et al.* , (see Chapter 2) is a direct consequence or the difference in the radial parts $P_{1p,j=1/2}(r)$ and $P_{1p,j=3/2}(r)$ of the wavefunctions.

If, as in our calculations, these differences are neglected, it is impossible to predict the small polarizations effects in K, L_1 etc. edges were the initial state is an L=0 core state, for instance as in the K-edge of Fe[81, 77].

Secondly, we have assumed that the energy separation between the ground state and the next excited state in the multiplet is sufficiently large to neglect mixing between them (J-mixing). This is true for most of the free rare earth ions, but in the solid state substantial mixing can occur by crystal fields or exchange fields, especially in the cases of Eu and Sm[105].

Furthermore the Born-Oppenheimer and Franck-Condon approximations are assumed to be valid so that the eigenfunctions can be separated into an electronic and a vibrational part. The latter part is neglected completely in this thesis, although it is realized that vibrational and also exchange interactions play a vital role in the occurence of dichroic phenomena in the visible[42, 43]. However, the vibrational contribution to the line width is at the moment is still much smaller than the experimental resolution, and can be neglected here.

3.7 Conclusion

In this chapter we have presented the theory, calulated spectra, temperature and angular dependence which are necessary to analyse experimental x-ray dichroism spectra of the 3d absorption transition of rare earth materials. The emphasis has been on the pure magnetic case, *i. e.* with the neglect of crystal field interactions, since such interactions often to a first approximation can be neglected. Furthermore, in the special cases of the L=0 ions Eu^{2+}, Gd^{3+} and Tb^{4+} crystal field effects are always negligible.

It was shown that in this limit the linear dichroism spectra are dependent on a single parameter C, dubbed the linear dichroism parameter, which is the product of an angular and a temperature and field dependent factor. The temperature dependent factor basically shows a free-ion Brillouin type dependence. By fitting experimental spectra to computer generated spectra one can obtain the linear dichroism parameter from the experiment, and by measuring the angular and temperature dependence of C one can obtain the local magnetic field on the ion. Also one can test for deviations of the free ion behaviour. Observation of deviations indicate crystal field effects are important.

Crystal field interactions were investigated to some extend. In the weak field case presented here the spectra are not expected to deviate appreciably from the atomic multiplet. It was shown that in cases where the field has not too low symmetry, the x-ray dichroism can provide information on the size of the crystal field level splittings. For cases of lower symmetry it was shown that useful data on the angular distribution of momenta might be obtained from the linear dichoism parameter.

Furthermore it was shown that circular dichroism spectra are proportional to the ionic magnetic moment. It is expected that circularly polarized soft x-rays will become available within the next decade. They will provide an important extra tool in x-ray measurements since they will allow one to distinguish between crystal field and magnetic effects.

Chapter 4

MXD IN HIGH MAGNETIC FIELDS

4.1 Introduction

In this chapter we describe a device in which the magnetic dichroism effect is applied to the generation of circularly polarized soft x-rays. Alternatively it might be used as a polarization filter. The heart of the device consists of a very thin layer of a rare earth compound supported on a highly transparent foil. This foil is placed in the centre of a superconducting solenoid with a field strength of several Tesla. The filter foil is cooled to 4.2 K by the cryostat He bath (see Fig. 4.1).

At the time of writing of this article it was not fully realized how large the magneto-crystalline anisotropy energies of rare earth ions can be. These anisotropies will hamper the alignment of the rare earth ions in the magnetic field, and therefore the presented performance specifications for the different elements are in most cases too optimistic. However, for the ions with a $L = 0$ groundstate, *i. e.* Eu^{2+}, Gd^{3+} and Tb^{4+}, the given numbers should be quite realistic.

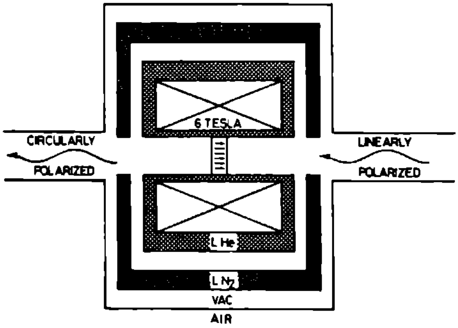

Figure 4.1: Schematical layout of the circular polarization line filter.

Nuclear Instruments and Methods in Physics Research A273 (1988) 429–435
North Holland, Amsterdam

CIRCULARLY POLARIZATION LINE FILTERS IN THE SOFT X-RAY RANGE

J.B. GOEDKOOP and J.C. FUGGLE

Research Institute of Materials, University of Nijmegen, Toernooiveld, 6525 ED Nijmegen, The Netherlands

B.T. THOLE, G. VAN DER LAAN and G.A. SAWATZKY

Materials Science Centre, University of Groningen, Nijenborgh 18, 9747 AG Groningen, The Netherlands

Received 31 May 1988

A feasibility study of the application of the recently discovered strong magnetic X-ray dichroism of rare earth materials to the production of circularly polarized X-rays is reported. A device is described that can be inserted downstream from a high resolution double beryl crystal monochromator. Calculations show that 45% transmission can be obtained with filters that yield 99% circular polarization in the energy range 950–1500 eV. Advantages of the proposed device are the low costs, the ease of installation and the high product of transmission × polarization.

1. Introduction

Linearly polarized X-rays are presently available over the full spectrum and with high intensities from electron storage rings. At the moment the situation for circular polarization is very much less favorable [1], although a number of sources are presently under investigation, such as the out-of-plane radiation from storage rings. Presumably this lag will be alleviated in the near future by the appearance of insertion devices such as the recently proposed crossed undulators [2] and asymmetrical wigglers [3–5]. Besides approaching the characteristics of their linearly polarized counterparts they will offer the possibility of switching between left and right polarizations at very short timescales (~ 1 kHz). However, these devices are still in an early stage of development [6]. Moreover, they work only on low emittance storage rings. Lastly, they will be rather costly to construct and installation will necessitate opening the storage ring.

Considering this, we think it useful to present a relatively cheap device with which it may be possible to obtain circularly polarized light at a number of discrete energies distributed over the photon energy range 850–1500 eV. Applications for such a line source could be found in e.g. photoemission, phase contrast microscopy and X-ray scattering of magnetically ordered materials. Also the device could be applied to the analysis of the polarization of other sources of circularly polarized X-rays.

The action of the filter is based on the recently established strong magnetic X-ray dichroism (MXD) of the 3d → 4f absorption spectra of magnetically ordered rare earth materials [7–9]. The filter consists of the thin foil of a rare earth material that selectively absorbs one of the two circularly polarized components of the linearly polarized synchrotron radiation and is inserted in the beamline downstream from a double beryl crystal monochromator or any other monochromator with comparable resolution.

In the present work we will first give a short review of the MXD effect in rare earth materials. On that basis we present calculations of the performance of the filter. The expected flux and the filter material are discussed and a comparison is made to alternative sources of circularly polarized X-rays.

2. Theory and example of MXD

It is well established that the 3d → 4f spectra of rare earth materials are predicted to a high degree of accuracy by atomic calculations [10–12]. In such calculations one obtains the line spectrum of all the transitions from the Hund's rule ground state of the initial $3d^{10}4f^{n}$ configuration, denoted by $|\alpha J M\rangle$, to the many possible states $|\alpha' J' M'\rangle$ of the $3d^{9}4f^{n+1}$ final configuration [13] (α denotes all other quantum numbers necessary to specify the state). This final state multiplet is divided in a $3d_{5/2}$ and a $3d_{3/2}$ part as a result of the large 3d hole spin–orbit interaction. As a typical example we reproduce in fig. 1, top panel, the calculated spectrum [13] of Ho^{3+}, obtained from the line spectrum by broadening with core hole lifetime and experimental resolution contributions [12]. With the presently attainable resolution

0168-9002/88/$03.50 © Elsevier Science Publishers B.V.
(North Holland Physics Publishing Division)

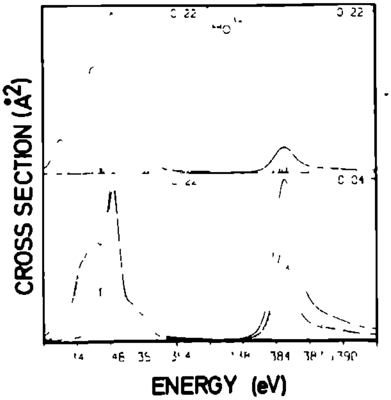

Fig 1 Upper panel Calculated 3d → 4f X-ray absorption spectrum of Ho^{3+} The full curves denote the absorption cross section of the $3d_{5/2}$ (left) and $3d_{3/2}$ (right) groups in units of Å^2 They were derived from the oscillator strengths (vertical bars) by convolution with Lorentzian and Gaussian curves representing the lifetime and instrumental broadening (see ref [9]) Bottom panel The same curves with the vertical scale of the $3d_{3/2}$ part expanded, showing the contributions of each ΔJ group to the total spectrum - $\Delta J = -1$, - $\Delta J = 0$ $\Delta J = +1$

of a double beryl crystal monochromator (varying from 0 3 to 0 4 eV) a large amount of structure is found

For our purpose it is important to note that, due to the dipole selection rules governing the absorption transition, the spectrum consists of three groups of lines with $\Delta J = -1$, 0 or 1 In the bottom panel of fig 1 the individual contributions are presented, and it is clear that each ΔJ group has an identifiable contribution to the total spectrum

The general expression for the absorption coefficient is given by [14]

$$\mu_{JJ'} = \text{constant} \times \sum_{M=-J}^{J} \sum_{q=-1}^{1} \begin{pmatrix} J & 1 & J' \\ -M & q & M' \end{pmatrix}^2$$

$$\times |\langle \alpha JM | C^{(1q)} | \alpha' J' M' \rangle|^2, \qquad (1)$$

where the $3j$ symbol gives the distribution of the line-strength of a given transition $|\alpha J\rangle \rightarrow |\alpha' J'\rangle$ over the allowed $M \rightarrow M'$ lines It also expresses a second selection rule limiting $\Delta M = M' - M = q$ to 0 or ± 1 The former transitions can be excited only by radiation that is linearly polarized parallel to the magnetic moment of the ion, the latter two only by circularly polarized radiation incident along the axis of magnetization

The physical meaning of eq (1) is best explained by looking at the level scheme of the ion in a magnetic field, where the degeneracy of the magnetic sublevels is lifted In fig 2 such a level scheme is given for the very simple case of the Yb^{3+} ($4f^{13}$) ion Here we have just one allowed final state and the spectrum consists of just one $\Delta J = -1$ line In the presence of a magnetic field this line is split into 18 lines divided over three groups with different ΔM Lower in the figure the division of the line strength over these lines as given by the squared $3j$ symbol is indicated and, at the bottom, the polarization state pertinent to the different ΔM transitions

At room temperature the magnetic splitting goes unnoticed as all the levels are equally populated and as it is much smaller than the experimental resolution However, the occupancy of the levels is governed by Boltzmann statistics so that when the field splitting $g\mu_B H$ is sufficiently large relative to the thermal energy $k_B T$, the upper levels are less occupied From the figure it can be seen that in the limit of 0 K only the lowest level is occupied so that absorption will take place only if the light has a left circularly polarized component.

In other rare earth ions there are also $\Delta J = 0$ and $+1$ transitions whose intensities, though subject to the

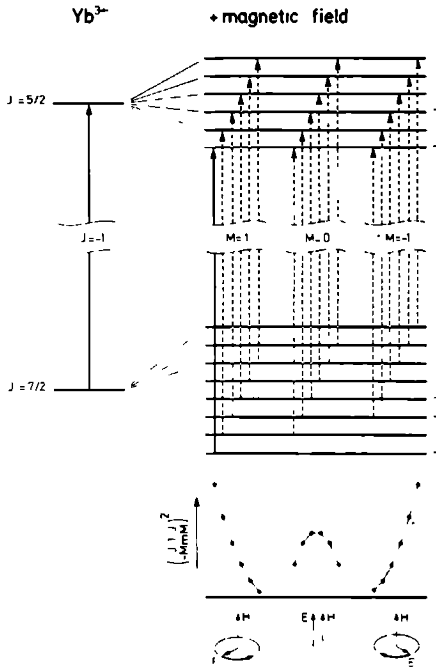

Fig 2 Energy diagram of the $3d^{10}4f^{13} \rightarrow 3d^9 4f^{14}$ transition of Yb^{3+} without (left) and with (right) a magnetic field The vertical arrows indicate the dipole selection rule allowed transitions $|\alpha JM\rangle \rightarrow |\alpha' J' M'\rangle$ Their relative intensities are given by the dots The required polarization is indicated at the bottom

same mechanism have strongly differing dependences on field temperature and polarization [9] In general one has to take the Boltzmann weighted average of the squared 3j symbol in eq (1) or

$$\mu_{JJ}(\Theta) = \text{constant} \times \sum_{q=-1}^{1} A^{q}_{JJ}(\Theta) \times |\langle \alpha J M | C^{(1q)} | \alpha J' M' \rangle|^{2} \qquad (2a)$$

with

$$A^{q}_{JJ}(\Theta) = \sum_{M=-J}^{J} \begin{pmatrix} J & 1 & J' \\ -M & q & M' \end{pmatrix}^{2} \times e^{-M/\Theta} \left(\sum_{M=-J}^{J} e^{-M/\Theta} \right)^{-1} \qquad (2b)$$

where

$\Theta = k_B T / g \mu_B H$

is the effective temperature In general the expressions for $A^{q}_{JJ}(\Theta)$ can be expressed in terms of Θ [7 9] We restrict our attention to the factors $A^{\pm 1}JJ'$ corresponding to the two circularly polarized cases In fig 3 their temperature dependence is plotted for several rare earth species assuming a realistic magnetic field of 6 T and atomic values for J and the Lande factor g One should note from these figures that the dichroism effects are largest for the elements with high J and g values

3 Performance of polarization filter

From the example discussed above it is easy to see that a foil of a material containing Yb^{3+} ions which are magnetically ordered along the direction of propagation of the light is capable of filtering out one of the circular components of any unpolarized or linearly polarized beam

For the general case the properties of a filter consisting of a magnetically ordered rare earth material can be calculated from the absorption coefficient of the two circular components $\mu_{\pm}$ given by eqs (2) using the Lambert Beer law

$$T^{\pm} = I^{\pm}/I^{\pm}_0 = \exp(-m\mu_{\pm}) \qquad (3)$$

where m is the mass thickness of the absorber From these transmissions one can calculate the degree of

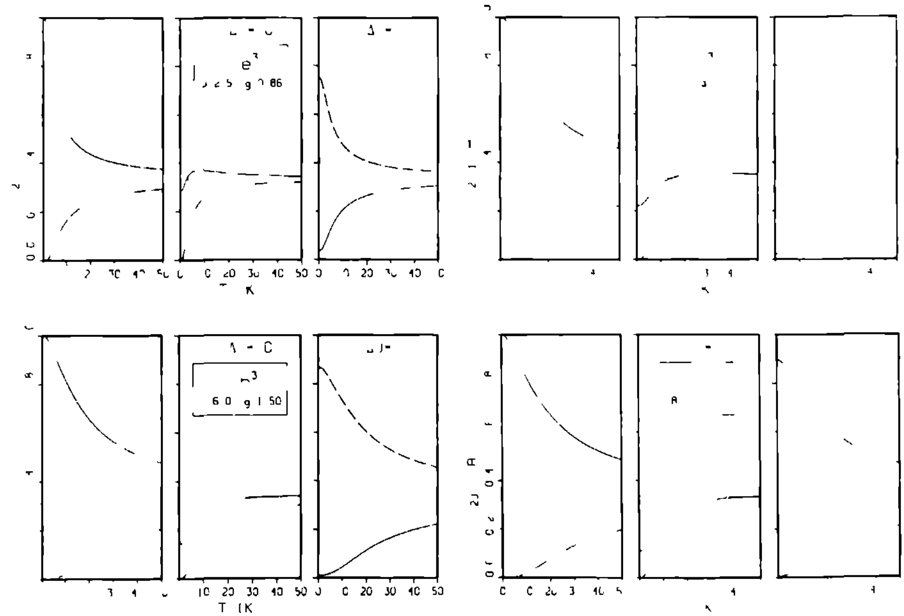

Fig 3 Temperature dependent part of the absorption strength A_{JJ} for $\Delta J = 0 \pm 1$ normalized to $(2J+1)^{-1}$ for Ce^{3+} Gd^{3+} Tb^{3+} and Ho^{3+} ions in a field of 6 T ——— left circularly polarized light - - - right circularly polarized light The high temperature limit of 1/3 is indicated by the dashed line

polarization of a linearly polarized beam after transmission through the foil

$$P = \frac{T^+ - T^-}{T^+ + T^-} = \frac{\exp(-m\mu_+) - \exp(-m\mu_-)}{\exp(-m\mu_+) + \exp(-m\mu_-)} \tag{4}$$

Similarly the overall transmission of that beam is given by

$$T_{\rm tot} = \tfrac{1}{2}(T^+ + T^-) = \tfrac{1}{2}\left(\frac{I^+}{I_0^+} + \frac{I^-}{I_0^-}\right)$$
$$= \tfrac{1}{2}[\exp(-m\mu_+) + \exp(-m\mu_-)] \tag{5}$$

For the calculation of the transmission it is necessary to include the background absorption by electrons in the valence bands and shallow core levels At the position of the 3d → 4f absorption edge their contribution amounts to a nearly energy independent background $\mu_{\rm backgr}$ the size of which can be estimated from tabulated values of atomic absorption coefficients [14] By comparing $\mu_{\rm backgr}$ with the values of $\mu_{3d \to 4f}$ calculated in ref [12] it is clear that the absorption of the strongest 3d → 4f peaks is typically 30 times larger than that of the background Although precise experimental determinations of the respective cross sections are lacking at the present moment this theoretical conclusion is corroborated by the strong peak to background ratios in the rare earth 3d–4f XAS spectra [10]

A second background effect arises from the 3d → *n*p absorption edge that for the rare earths heavier than Gd lies between the $3d_{5/2} \to 4f$ and $3d_{3/2} \to 4f$ lines From ref [14] values of – 0 02 Å^2/eV/atom are found for the 3d → *n*p edge, which is quite comparable to the cross section of the $3d_{3/2}$ lines of the heavy rare earth (see e g fig 1) so that their effectiveness as polarizing lines is strongly limited

Fig 4 gives the transmission for a linearly polarized beam (eq (5)) and the degree of circular polarization after conversion by the foil (eq (4)) as a function of photon energy for a number of rare earth ions The transmission of left and right circularly polarized beams (eq (3)) is also given The data were plotted assuming an energy independent $\mu_{\rm backgr}$ The 3d → *n*p edge was not included in the calculation owing to the lack of knowledge of its energy dependence The mass thicknesses were chosen to yield a degree of polarization of 99% in the main polarizing peak and a field of 6 T and a temperature of 4 2 K were assumed

Table 1 gives the mass thicknesses necessary to obtain under the same conditions 90% or 99% circular polarization and the corresponding transmission $T_{P-90\%}$ and $T_{P-99\%}$ for all major absorption peaks

Table 1

Calculated rare earth mass thickness of trivalent rare earth ions yielding 90% or 99% circular polarization with the indicated sense of rotation (+/− helicity = left/right circularly polarized) The magnetic field is assumed to be antiparallel to the light direction The absorption by valence and shallow core levels has been included (see ref [14])

Element	J	$M_{4\,5}$	Energy (eV)	Helicity	P = 90%		P = 99%	
					m (μg/cm^2)	T (%)	m (μg/cm^2)	T (%)
Ce	2 5	5	882 0	+	55	2 9	100	0 3
		4	898 2	+	100	9	200	2 2
			900 5	−	45	12	80	3 5
Pr	4	5	925 6	+	55	2 2	100	0 2
			927 6	−	180	3	30	0 3
		4	945 2	−	45	28	80	15
Nd	4 5	5	–			–	–	–
		4	999 6	−	40	35	70	25
Sm	2 5							
Gd	3 5	5	1184 7	−	28	18	70	7
		4	1214 9	+	100	19	170	8 5
Tb	6	5	1239 0	−	46	39	80	30
Dy	7 5	5	1288 0	+	120	34	210	21
			1293 1	−	34	45	70	38
Ho	8	5	1343 7	+	250	23	230	11
			1348 2	−	28	48	64	43
		4	1384 4	−	410	22	750	10
Er	7 5	5	1405 3	−	24	48	65	32
		4	1444 7	−	550	21	1000	11
Tm	6	5	1461 6	−	28	48	68	43
		4	1507 3	−	100	11		
Yb	3 5	5	1519 4	−	62	46	110	40

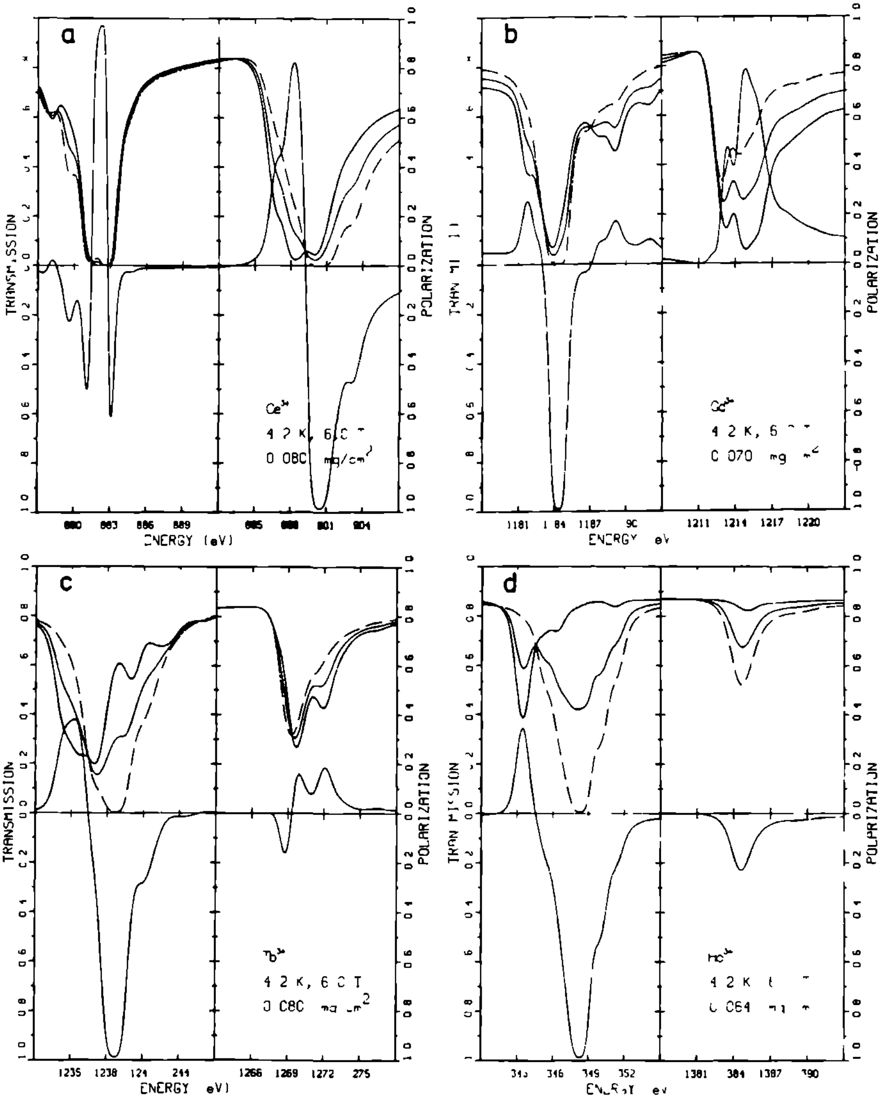

Fig. 4 Calculated performance of a foil containing the specified mass thickness of paramagnetically aligned rare earth ions at 4.2 K and in a field of 6 T. The mass thickness is chosen to give a maximum polarization of 99%. Dashed (dotted) curve: transmission of left(right) circularly polarized radiation. Dash-dotted curve: transmission of linearly polarized radiation. Full curve: degree of circular polarization behind the foil.

4 Discussion

From table 1 it can be seen that high degrees of circular polarization can be obtained with satisfactory transmission factors The maximum transmission for a certain degree of polarization lies in the $3d_{3/2}$ for the first half of the series and switches over to the $3d_{5/2}$ at Gd [15] It is highest in the elements with high J and g values like Nd in the first half of the series and Ho in the second half

Ce Gd, Dy and Ho have strong polarizing peaks of both senses with $\Gamma_{P\ 99\%}$ ranging from 3 5% to 43% allowing switching between them by tuning the monochromator Pm is not listed because it is radioactive and Sm is left out because its MXD effects decrease very rapidly with temperature due to its low J and g values

4 1 Flux

The flux from a double beryl crystal monochromator is fairly strongly dependent on energy in the range of interest here If a focussing mirror is used as with the BESSY KMC monochromator the flux per 100 mA electron beam current rises from 10^8/s at 850 eV to 10^9 /s at 1550 eV [16] (slightly different numbers hold for the SSRI JUMBO monochromator [17]) With the calculated $P - 99\%$ transmission factors the resulting flux after conversion ranges from $\sim 5 \times 10^7$/s (Ce) to $\sim 10^9$/s (Ho)

It must be stressed that these performances are based on calculated absorption coefficients However, the main experimental features of the 3d → 4f multiplet structures and peak to background ratios are in good agreement with these calculated values Thus, while there may be some uncertainty in the detailed shapes of the polarization dependence and the absolute cross sections it is unlikely that the major features described here will be significantly changed

4 2 Filter materials

The mass thicknesses listed in table 1 correspond to submicron film thicknesses This allows vacuum deposition of the rare earth compound on a high transmission foil (e g 10 μm Be, Al, C or Ti) Also the rare earth ions could be incorporated in a foil of a (dilute) alloy of those same materials In either case the extra material leads to an additional attenuation in the order of 10 to 50%

The requisite magnetic ordering could be either paramagnetic or ferromagnetic In the latter case the high exchange field results in higher effective temperatures Θ but this advantage is strongly reduced by the occurrence of complex non-collinear spin structures present in most rare earth compounds [18] which lead to a decrease in polarization [8] Paramagnetic ordering at experimentally feasible conditions of 4 2 K 6 T using a superconducting magnet gives adequate ordering for the rare earths with a high ground state J value This has the additional advantage of allowing the field direction and thus the polarization state to be switched

4 3 Comparison to other methods

Sources of circularly polarized X-rays currently existing or under development can be divided into two classes The first is based on the polarization characteristics of radiation from relativistic electrons moving in a magnetic field This class includes the out-of-plane emission from storage rings which in principle is usable over the whole energy range of the synchrotron Until now it has been applied only below 40 eV [19,20] and between 7 and 9 keV in the hard X-ray regime in MXD experiments on Gd [21] and Fe [22] and in Compton scattering experiments [23]

As mentioned in the introduction new developments in this class are asymmetric wigglers and crossed undulators Working on low emittance rings only, these sources will be the circular polarized equivalent of standard wigglers and undulators providing a continuous spectrum The predicted intensities are 10^{12} to 10^{13} photons per second at $\sim$ 1000 eV, dropping steeply at higher energies It will be possible to switch between the polarization senses at a rate of 1 kHz

The second class is formed by the extension to the X-ray region of the polarization phenomena known from the visible region Under this heading falls birefringence, e g in MgF_2 up to 9 eV [24] and Si at 10 keV energies [25], where degrees of polarization of 85% and 15% respectively have been obtained To our knowledge it has not been used in the soft X-ray range

5 Conclusion

We have shown that the filter described here can provide a source of circularly polarized X-rays at a series of energies between 850 and 1550 eV We find a degree of polarization of 99% with a satisfactory intensity of 5×10^7 10^9 photons/s 100 mA storage ring current, assuming a double beryl crystal monochromator equipped with a focussing mirror The bandwidth is $\sim$ 0 3 to $\sim$ 0 45 eV depending on monochromator resolution

Compared to other sources the main disadvantage of the device is the line character However it is rather unique in providing a high intensity × polarization product in this energy range The main advantages of its application in a polarizing filter are the unique energy range, the simplicity and correspondingly low costs of the design and the possibility to switch the polarization senses

Finally we note that the use of this device can be extended straightforwardly to the determination of the polarization of other circularly polarized X-ray sources

Acknowledgements

This work was supported in part by the Netherlands Foundation for Chemical Research (Stichting Scheikundig Onderzoek Nederland, SON) with financial support from the Netherlands Organization for Scientific Research (Nederlandse Organisatie voor Wetenschappelijk Onderzoek, NWO) and by the Committee for the European Development of Science and Technology (CODEST) program We are grateful to the Laboratoire pour l'Utilisation du Rayonnement Electromagnétique (LURE) staff for their valuable aid

References

[1] Applications of Circularly Polarized Light Using Synchrotron and Ordinary Sources, eds F Allen and C Bustamante (Plenum, New York, 1985)

[2] M B Moiseev, M N Nitikin and N I Fedosov, Sov Phys J 21 (1978) 332

[3] J Goulon, P Elleaume and D Raoux, Nucl Instr and Meth A254 (1987) 192

[4] H Onuki, Nucl Instr and Meth A246 (1986) 94

[5] K J Kim, Nucl Instr and Meth 219 (1984) 425, Nucl Instr and Meth 222 (1984) 11

[6] First results have just been obtained, see H Onuki, N Saito and T Saito, Appl Phys Lett 52 (1988) 173

[7] B T Thole, G van der Laan and G A Sawatzky, Phys Rev Let 55 (1985) 2086

[8] G van der Laan, B T Thole, G A Sawatzky, J B Goedkoop, J C Fuggle, J-M Esteva, R C Karnatak J P Remeika and H A Dabkowska, Phys Rev B34 (1986) 6529

[9] J B Goedkoop, B T Thole, G van der Laan, G A Sawatzky, F M F de Groot and J C Fuggle, Phys Rev B37 (1988) 2086

[10] J Sugar, Phys Rev A6 (1972) 1764,
J Sugar, W P Brewer, G Kalkowski, G Kaindl and E Paparazzo, Phys Rev A32 (1985) 2242

[11] S A Yavna, V L Sukhorukov and V F Dehmekhin, Sov Phys Solid State (Fiz Tverd Tela) 26 (1984) 2300

[12] B T Thole, G van der Laan, J C Fuggle, G A Sawatzky, R C Karnatak and J-M Esteva, Phys. Rev B32 (1985) 5107

[13] The calculations were performed with the program of R D Cowan, described in his book The Theory of Atomic Structure and Spectra (University of California Press, Berkeley, 1981)

[14] B I Henke, P Lee, T J Tanaka, R L Shimabukuro and B K Fujikawa, Atom Data Nucl Data Tables 27 (1982) 1

[15] Note that although the linear MXD effects of Gd are quite small, it gives quite strong polarization

[16] J Feldhaus, F Schafers and W Peatman, SPIE vol 733, Soft X-ray Optics and Technology (1986) 272

[17] Z Hussian, E Umbach, D A Shirley, J Stohr and J Feldhaus, Nucl Instr and Meth 195 (1982) 115

[18] Handbook of the Chemistry and Physics of Rare Earths, vol 2, eds K A Gschneider and L Eyring, (North-Holland, 1979)

[19] U Heinzmann, B Osterheld and F Schaefers, Nucl Instr and Meth 195 (1982) 395

[20] U Heinzmann, p 1 in ref [1]

[21] J L Erskine and E A Stern Phys Rev B12 (1975) 5016, E Keller and E A Stern, EXAFS and Near Edge Structure III (Springer, Berlin, 1984) p 507

[22] G Schutz, W Wagner, W Wilhelm, P Kienle, R Zeller, R Frahm and G Materlik, Phys Rev Lett 58 (1987) 737

[23] M J Cooper, D Laundy, D A Cardwell, D N Timms, R S Holt and G Clark Phys Rev B34 (1986) 5984

[24] U Heinzmann, J Phys E10 (1977) 1005,
P A Snyder and E M Rowe, Nucl Instr and Meth 172 (1980) 345

[25] J A Golovchenko, B M Kincaid, R A Levesque, A E Meixner and D R Kaplan, Phys Rev Lett 57 (1986) 202

4.3 An X-ray Absorption Microscope

In addition to the applications mentioned in the foregoing paper, a high-field solenoid as depicted in Fig. 4.1 can be used to construct an x-ray absorption microscope. In such a device the divergence of the magnetic flux out of the bore of the magnet is used as objective lens for the yield of electrons excited by light (or electrons) from a sample placed in the bore. This is possible because the electrons stay near the magnetic field line near which they were created, spiralling around it in tight orbits. A second coil producing a weak field, *e. g.* 10 Gauss, collimates the electron field before it is made visible by means of a microchannel electronmultiplier plate and a phosphor screen.

The magnification by a magnetic lens is given by the square root of the high to low field ratio[114], and with the field values given above would be 20–40. The resolving power depends on the radius of the orbit of the helical motion of the electrons around the magnetic field lines and thus is determined by the maximum field strength and the electron energy. With standard technology a resolving power of 0.5 μm has been proven to be feasible for 5 eV electrons[114].

Until quite recently, magnetic lens systems were only used in laboratory spectrometers[115, 114]. In combination with synchrotron radiation the magnetic electron microscope would be a powerful tool for XAS measurements of inhomogeneous samples. In addtion, in combination with the MXD effect such a device would offer the possibility to study the high-field magnetic domain structure. of ferromagnetic materials.

Work on the design of a suitable system, based on an existing 6 Tesla superconducting magnet, has been started. The current design includes the possibility to vary the sample temperature independendly from the magnets' cryostat between 10 and 400 K by using a separate flow-cryostat for sample cooling. Also the design allows the sample to be rotated arround the magnetic field axis.

Chapter 5

EXPERIMENTAL ASPECTS OF SOFT X-RAY ABSORPTION SPECTROSCOPY

5.1 Introduction

This chapter deals with experimental aspects of soft x-ray spectroscopy. The first two sections give details on the beamline and experimental apparatus used in the experiments that are described in the remaining part of this thesis. The last two sections are reprints of papers describing innovative work in XAS.

Section 2 describes the double crystal monochromator beamline constructed by our group (Nijmegen and Groningen Universities) at the newly constructed Super-ACO storage ring at the Laboratoire d'Utilisation de Rayonnement Electromagnetique (LURE), Orsay, France. This beamline was financed by a EC CODEST program fund, and was completed slightly over two years after the fund was granted.

Section 3 describes the LURE-based experimental system used for most experiments, which in the last four years has evolved into a well-equipped surface science system. Special attention has been given to the need to operate the machine quickly, since beamtime is too expensive to be wasted much.

Section 3 deals with the possibility of constructing a soft x-ray monochromator from a combination of a synthetic metallic multilayer and a organic crystal.

Section 4 presents a method for the reproducible characterization of the resolution of soft x-ray monochromators. This work was spurred by the need to obtain the width of the curve with which the calculated atomic dipole spectra are broadened to simulate the experimental resolution (see Chapter 3), and the necessity to be able to compare the resolution of the multilayer/organic crystal monochromator with that of other monochromators.

5.2 A Windowless UHV Double Crystal Monochromator Beamline for Soft X-ray Absorption Studies

5.2.1 Introduction

The experimental work described in this thesis was carried out during visits to four synchrotron rings in three different countries. In all cases a double crystal monochromator was used: the SOXAFS beamline 3.3 at SRS Daresbury[116], the Doppelkristal line at BESSY[117], Berlin, and the old[118] and new double crystal lines at ACO and Super-ACO, both at LURE, Orsay. We will describe here the new Super-ACO beamline SA21, which was constructed by our group as part of an EC CODEST project, and is fairly representative for the other lines.

The work in three synchrotron radiation centres gave a unique opportunity to compare technical details, and has allowed us to construct a relatively cheap state-of-the-art beamline. At the moment of writing the beamline can be used for high resolution-high intensity XAS and EXAFS experiments in the soft x-ray range (650–5000 eV). In a later stage a 1:1 focussing mirror with focal distance of 10 m will be installed behind the monochromator, more than doubling the total length of the beamline. This addition will enhance the intensity even further to enable XPS (x-ray photoemission), CIS (constant initial state), CFS (constant final state), resonant XES (x-ray emission), and XPD (x-ray photodiffraction) studies.

5.2.2 Layout of the beamline

The beamline is described moving downstream with the photons, starting at the source point.

The beamline is situated at bending magnet SA21 of the Super-ACO storage ring at LURE, Orsay. Under normal operating conditions the critical photon energy is 650 eV. As can be seen in Fig. 5.1, in the operating range of the monochromator the input flux drops monotonically, and even almost exponentially at high energies[119].

The front-end of the beamline, built by LURE, contains fast acting vacuum protection shutters and a removable gamma radiation trap which is inserted during injection of the ring. The front-end opens to a mirror box where a grazing incidence mirror deflects one half of the 30 mrad wide light cone to a neighbouring beamline. The mirror box also protects the synchrotron

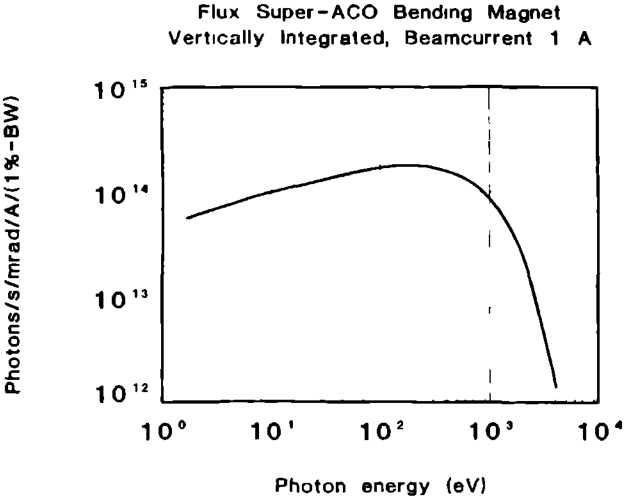

Figure 5.1: Flux from a bending magnet of Super-ACO under normal operating conditions.

vacuum from accidental venting of parts of the beamline by retarding the shock-waves through expansion, giving the shutters more time to close.

At 6 meters from the source point the radiation beam passes through a thin absorber foil which filters out the low energy part (IR to UV) of the white light beam, leaving the x-rays and reducing the power in the beam by about 50%[117]. The filter foils are mounted on a vertically adjustable rack, allowing selection of the filter (currently 1.5, 3.0, 4.5 μm Al and 1.1 μm C) according to the operating photon energy and monochromator crystals used. The same vacuum chamber is fitted with two horizontal collimators with which the beam width is defined to within 0.1 mrad, *i. e.* 100 μm at 10 m.

The monochromator, which is described below, is located at 8 meters from the source point. One meter behind the monochromator the output signal I_0 is monitored by the electron yield signal from a 90% transparent tungsten grid or a 1.5 μm Al foil. The I_0 gives information on structures in the output due to absorption edges or so-called glitches[120], and is therefore stored along with the data. Experimental systems interface to the I_0 chamber.

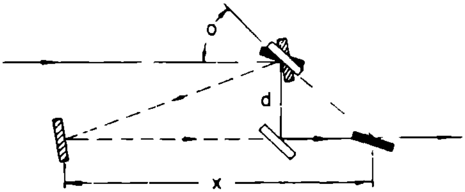

Figure 5.2: Principle of constant deviation non-dispersive double crystal monochromator.

The double crystal monochromator

The double crystal monochromator, located at 8.5 m from the source point, is of the non-dispersive (+/−) constant-deviation type (see *e. g.* James[54]). The principle of the instrument is explained in Fig. 5.2. Only the part of the incoming white radiation that fullfills the Bragg equation

$$n\lambda = 2d\sin\theta, \tag{5.1}$$

(where d is the lattice spacing of the monochromator crystals and θ the Bragg angle,) is reflected by the first crystal. The second crystal is kept parallel to the first by a combined rotation-translation mechanism. and thus Bragg-reflects the beam into its original direction, but offset downwards by a fixed distance (30 mm for this instrument).

All movements of the energy scanning mechanism are mechanically coupled and driven by a single lead-screw/stepping motor external to the vacuum system. Energy setting is accomplished by converting the readout of a linear optical encoder to the angle of incidence on the first crystal, using the formula

$$\theta = 45^\circ - \arctan\frac{L(45^\circ) - L(\theta)}{D} \tag{5.2}$$

where D is the vertical offset of the beam, nominally 30 mm, and $L(45^\circ) - L(\theta)$ is the difference between the actual reading of the linear encoder and the reading at $\theta = 45^\circ$.

Calibration of this formula to correct for errors in the constants D and $L(45^\circ)$ was achieved using a angular optical encoder mounted on the axis of the first crystal. Differences between the actual Bragg angle and the angle

crystal	Miller indices	$2d$ (Å)	Energy range (eV)
ML/KAP ($KHC_8H_4O_4$)	(100)	26.632	472–800
Beryl ($Be_3Al_2Si_6O_{18}$)	$(10\bar{1}0)$	15.95	790–1550
Quartz (SiO_2)	$(10\bar{1}0)$	8.512	1500–1800
InSb	(111)	7.486	1680–
Si	(111)	6.271	2010–

Table 5.1: Currently available monochromator crystals

obtained from eq. (5.1) were less than 120 arcsec over the complete 10–80° angular span of the monochromator. A more detailed description of the mechanical coupling mechanism and the calibration procedure can be found in MacDowell *et al.* [116].

Crystal change and alignment

Crystals are changed by bringing the monochromator up to air. After modest baking a base pressure of 10^{-9} Torr is obtained with a 200 l/s ion pump. Extreme care is taken to prevent vacuum contamination with hydrocarbons which were found to deposit on the crystals due to radiation induced cracking. Fine-tuning of the crystal parallelism before operation, which corresponds to maximizing the throughput, is achieved by orienting the first crystal around the two perpendicular axes in the surface plane using a double lever system driven by two UHV compatible stepping motors.

A number of different crystals is available, for which the lattice spacings and energy ranges are given in Table 5.1. Maximum crystal dimensions are 5x25x45 mm^3 but smaller sizes can be installed using high precision interface blocks.

The mounting block of the first crystal is water-cooled with the dual purpose of minimizing damage by the heat load of the white synchrotron beam and preventing thermal expansions that would influence the calibration through changes in the lattice spacing d. Gallium is used to enhance the thermal coupling between the back surface of the crystal and the holder.

Rocking curve control

An important property of double crystal monochromators is the *rocking curve*, the intensity profile obtained by scanning one crystal through the Bragg condition set by the other. The shape of the rocking curve is related to the instrumental function and its width gives information on the crystal quality and resolution. The maximum of the rocking curve corresponds to exactly parallel crystals[54]. A special feature of the Super-ACO instrument is the fully automatic acquisition of rocking curves, whereafter the instrument aligns itself on the maximum. This feature allows rapid and reproducible optimization of the instrument

5.2.3 Monochomator control and data acquisition

The monochromator control electronics and software were designed and realized at the University of Nijmegen Electronics department.

The hardware consists of an Olivetti M240 Personal Computer, an interface unit, two stepping motor driving units, two Heidenhain encoders, and a small hand-held remote control box. The computer, which controls all functions of the monochromator and runs the data acquisition programs, is equipped with a *PIO-12* interface which is used for all communication with the other units, and with an IEEE interface, which can be used for data collection with more sophisticated measurement units.

The main Interfacing Unit (I. U.) is connected to the computer by the *PIO-12* bus and multiplexes the communication between the computor and the other instruments. Also it houses three digital scalers for positive TTL pulse counting detectors and an 8 digit LED display giving the actual energy.

The two Heidenhain units are used for measuring and calibrating the position of the monochromator carriage. The first (model VRZ181) reads and displays the linear optical encoder connected to the main driving mechanism with an accuracy of $0.1\mu m$. After every movement of the monochromator the computer reads this instrument via the interface and converts the position to Bragg angle and photon energy with the aid of the calibrated form of eq. (5.2).

The second Heidenhain (model VRZ166) reads and displays the circular optical circular encoder mounted on the rotation axis of the first crystal, which is used only in the calibration procedure described by MacDowell *et* *al.* [116].

Both steppermotor controllers are build around the simple supplies delivered with the motors. Apart from controlling the stepping mode and direction they signal limit switch error situations, both digitally and via front panel LED's. The two internal motors used for setting the parallelity of the crystals are powered by a single supply which is electronically switched between the motors. The relative position of these motors, which are not equipped with encoders, is displayed on two signed 4 digit LED displays on the front panel, giving the number of steps made by each motor since power-up.

Control is either by the computer or manually, via front panel switches or with the remote control box. The latter consists of a small hand-held box connected to the interface unit via a 8 m long cable. It gives the operator push-button control over the monochromator movements which greatly adds to the experimental convenience in complex situations like positioning of the sample in the beam, where rapid scanning of the monochromator on and of the absorption maximum is required.

The computer program is menu organized, with the possibility of toggling between the alphanumeric menu screens and the graphic spectrum displays. It consists of ~110 small modules written in *C* (Microsoft *V*5 0). The six menus are dedicated respectively to initialization, gross changes of the monochromator position. data acquisition, automatic acquisition of rocking curves, remote control, and energy calibration on two edges of well known energy. The program takes data either from the scalers of the interface unit or from the *IEEE* 488 interface card in the computer, allowing great flexibility in the choice of detectors.

The main data acquisition menu includes options for dividing a single energy scan in up to 5 regions with different step sizes (0.05–10 eV/step), and multi-scanning of the same spectrum. In this mode both the new scan and the sum of the previous scans are displayed on the screen. The new data are stored at the end of each scan, while at the completion of all scans also the sum spectrum is stored. Data storage is in binary form; files consist of a header and two arrays of signal data and an I_0-monitor data, both stored as unsigned long integers. Currently hardcopies of the data are obtained by dumping the graphics screen on a 24-pin printer.

The algorithm for scanning the monochromator involves a scheme of successive approaches to the new position: The desired new energy is converted to a position of the linear encoder and the difference between the current position and the desired position is calculated. The motor is moved towards the new position with a step corresponding to a fixed, large percentage of this difference. The new position is read from the linear encoder and the procedure is repeated until the new position and the desired position differ less than a specified fixed value. In order to minimize the effects of back-lash, whenever the position of the monochromator is higher than the position wanted, a large negative overshoot is included in the first step to assure that the desired position is always approached from below.

5.2.4 Performance

Until now the monochromator has been operating mainly with beryl crystals. For these crystals a typical throughput curve of the monochromator is shown in Fig. 5.3.a. The observed increase of intensity with the photon energy is the result of the competing effects of decreasing intensity from the storage ring (see Fig. 5.1), and the increasing monochromator throughput with decreasing Bragg angle. The strucure at higher energies is due to absorption edges of the Al and Si present in the beryl crystals.

The estimated maximum flux at 1300 eV is of the order of 6x10^8 phot/sec-/100mA/mrad hor./full vert./% bandwidth. In more practical terms: with the ring operating at 300 mA electron current and with the slits set to give a 1x1 mm^2 spot on the sample we estimate the flux at 1300 eV to be 5x10^6 photons/second. with a resolution of $\leq$ 1 eV. At this energy the vertical divergence of the beam does degrade the resolution and for optimum resolution the entrance slit of the monochromator has to be closed to 100 μm ($\sim$ 450 meV. with a concommitant loss of flux. However, even then it is possible to acquire spectra of films of submonolayer thickness in one half hour.

The instrument was characterized further by measurements of the rocking curve at a number of different Bragg angles. The obtained widths were identical to those reported by Hussain *et al.* [121]. Also, spectra of the Ni L_3 edges and various rare earth M_5 edges, as for instance that of Ho in Fig. 5.3.b were comparable to spectra published elsewhere[29, 122].

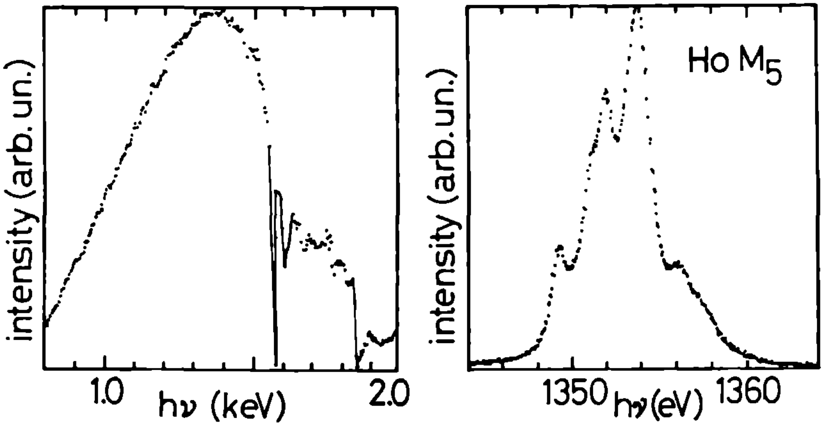

Figure 5.3: a. Throughput of the monochromator fitted with beryl ($Be_3Al_2Si_6O_{18}$) crystals. The structure above 1500 eV is due to the K absorption edges of Al and Si.
b. M_5 total yield spectrum of Holmium.

5.3 The Dutch Experimental Surface Science system at LURE

5.3.1 General description

The system is build up of two UHV chambers separated by an isolation valve. Each chamber is pumped with cryopumps which can be valved off during venting or during regeneration of the pumps. The whole system is mounted on a rectangular frame, which carries also the Helium compressor unit of the cryopumps (Leybold RG 210) and the power supply of the bake-out oven. The frame is equiped with wheels and (x,y,z) orientation adjustments for alignment of the system to the beamline. All watercooling circuits are equiped with quick-connect couplings, making (de-)coupling to the beamline a matter of minutes.

The chambers and the cryopumps can be roughed out independently, using a single turbopump mounted on a five-way manyfold located in the system's frame. The chambers can be baked either separately or together with an oven system build up from insulated aluminium panels.

5.3.2 Preparation chamber

The preparation chamber acts mainly as insertion lock for the sample analysis chamber. It is equiped with an axially mounted linear transfer rod that accomodates up to six samples. The samples can be cleaned by either scraping with an Al_2O_3 file or ion bombardment before being brought in the analysis chamber. Since in general the acquisition of an XAS spectrum of a polycrystalline sample is a matter of only tens of minutes it is possible, by baking the system overnight, to measure six samples per day. If necessary, this speed can be further enhanced by installation of a simple bajonet mechanism with which individual samples can be transferred from a 10-–slot magazine in the preparation chamber to the manipulator on the analysis chamber.

5.3.3 Analysis chamber

The design of the analysis chamber has three functional levels:

1. The top level is dedicated to the preparation and characterisation of single crystalline samples. It is equiped with a two grid forward view LEED optics (Vacuum Generators) and a PC controlled single pass

cylindrical mirror analyzer (CMA) with a coaxial electron gun (PHI 3017 AES subsystem with 10-155 CMA). This latter system works in the pulse counting mode, allowing the use of low sample currents and thus minimizing contamination of the sample by the electron beam[123]. Spectra are obtained in direct signal, but can be smoothed and differentiated digitally. Sample cleaning is possible with an ion bombardment system which involves backfilling the chamber to a pressure of 10 ^{5}.

2. The middle level is the measurement level where the chamber interfaces with the preparation chamber and the x ray beam entry port. Standard components on this level are a viewport on the flange opposite the beam entry port, which is necessary for alignment of the system; and the yield detector on a port which makes an angle of 45° with the beam. Different detectors are available for the different electron-yield methods that are discussed in the next section.

3. The lowest level contains, besides pumping and gas inlet lines, a Knudsen type evaporator unit, which aims upwards at the sample position in the middle level. The unit consists of a commercial oven-and-crucible assembly, mounted coaxially with a stainless steel water-cooled heat shield on an FC63 flange. A shutter on the same flange completes the unit. In order to minimise outgassing. the mounting port of the evaporator unit is also water cooled on the outside by a copper spiral wrapped around the port.

   Determination of the thickness of the evaporated layer is done with a commercial water-cooled oscillating quartz crystal monitor (Intellemetrics IL100) located a few centimetres behind the samples' deposition position.

Transfer of the sample between levels 1 and 2 is possible with a standard high precision micromanipulator (VG HPLT 165) mounted on top of the system. All electrical connections to the sampleholder can be made via the feedthroughs on the manipulator. For low temperature experiments the manipulator was equiped with a homebuild He cold finger, which could be rotated around its vertical axis using a differentially pumped rotary feedthrough. The lowest temperature attainable with this cryostat is 50 K. A commercial UHV compatible low-loss cryostat (Oxford Instruments CF100) has been purchased, and will be installed in the next phase of the development.

Yield Detection Methods for XAS

Although widely used, electron-yield measurements are still poorly understood. Important work has recently been done in the hard x-ray range[124], but much less is known about soft x-ray electron yield. This section describes the different detection methods of XAS.

Traditionally x-ray absorption spectra were measured in the standard transmission mode. Here the spectrum is given by the ratio between incident and transmitted intensity. In the lower x-ray energy range, where the attenuation length of the x-rays is of the order of tens of microns or less, preparing suitable. free standing films of uniform thickness is in most cases prohibitively difficult. Furthermore the absorption spectrum has to be obtained from a ratio measurement, with the concommitant noise problems.

Several indirect methods of XAS measurement, known as *yield methods*, have have been developed to complement and largely replace the traditional method, especially in the soft x-ray range. In these methods one measures instead of the transmitted intensity the yield of electrons or fluorescent radiation produced as a result of the decay of the core hole, created in the absorption proces.The great advantage of yield methods is that the sample may be a powder, a solid bulk sample, or even a liquid.

Fluorescence yield is a true bulk method since both the incident as fluorescent radiation have large attenuation lengths, which are of the order of microns in the soft x-ray range and larger at higher energies.

Electron yield techniques have a probing depth which is determined by the range of the detected electrons. The primary Auger electrons lose their energy in collisions with valence electrons, producing a cascade of electrons with lower energies. The yield at the surface consists therefore mainly of electrons with a kinetic energy less than 5 eV. Depending on their energy, the range of the Auger electrons lies between 10 nm in the soft x-ray range and 1000 nm at a few keV. Therefore, electron yield in the soft x-ray range is quite surface sensitive, necessitating the use of ultra high vacuum. However, in the soft x-ray range fluorescence yields are low[125, 16, 126, 17], making electron yield the method of choice.

Electron yield methods

A number of varieties of electron yield methods exists, which differ in the detector used.

- The simplest method, and the one used in most of the work described here, is the *total electron yield* method, where all yield electrons are collected without energy discrimination. The total yield detector used for most of the work described here consists of a pulse-counting channeltron detector, which is mounted in a grounded hood, which leaves the channeltrons' aperture exposed to the electron flux from the sample. Optionally the front of the detector is biased to +300 Volts to attract electrons into the aperture.

  The detector assembly is mounted with studs on a FC63 flange equiped with the necessary voltage feedthroughs. A bellows between this flange and the mounting port of the detector allows positioning of the detector in the flux of electrons from the sample.

- A variety on the total yield method is the *total electron yield current* method, where the photo current from the sample is measured using a pico-amperemeter. In many respects this is the easiest method, and in a recent comparative study this method was found to be the most reliable[124]. Prerequisites for the use of the current mode are sufficient conductivity of the samples and a sufficient signal strength (*i. e.* photon flux). A separate version of the monochromator acquisition program has been developed for current measurements using a Keithley model 617 electrometer which is connected to the beamline computer via an *IEEE* interface. Initial tests failed because of the signal to noise ratio was too low, which may be due to leakage currents in the UHV current feedthroughs.

- In the *partial yield* method a retarding field analyser is used to select the high energy part of the yield spectrum, with the purpose of increasing the surface sensitivity. To this end the total yield detector described above can be fitted with variable voltage high-transparency grids placed in front of the channeltron aperture, giving the possibility to reject the slowest secondary electrons in the partially electron yield mode. Little experience exists in this mode, and its usefulness is not yet clear.

- In the *Auger yield* method a cylindrical mirror analyser is used to select the signal of the primary Auger electron from the total yield spectrum. In principle this offers the possibility of depth selective XAS measurements by monitoring the yield of electrons in the inelastic tail of the Auger peaks. These electrons have undergone one or more inelastic collisions with valence electrons, and their energy loss is a measure of their creation depth. The experimental system described in the previous section allows for this option through the possibility of mounting the CMA on the yield detector port.

5.4 Multilayer/crystal monochromators for soft x-rays

Nearly all the x-ray absorption transitions involving localized final states lie between 300 and 1500 eV (the soft x-ray range). The energy range 850–1500 eV, which encompasses all the 3d→4f transitions of the rare earths, is very satisfactorilly covered by the double Beryl crystal monochromator. In contrast, the 1s→2p of O, N, F, and the 2p→3d transitions of all the 3d transition elements (except Ni) fall in the lower energy range 300-850 eV, for which no high resolution monochromators were available until quite recently.

It is possible to extend the range of double crystal monochromators to lower energies by using monochromator crystals with a larger lattice parameter d, which is related to the photon energy by $E = hc/2d \sin\theta$, where θ is the Bragg angle. The only suitable crystals known which have larger $2d$ ratings than Beryl ($2d = 15.95$Å) are the *acid phthalate salts* (XAP, X = Na, K, Rb. Very short tests (~minutes) were sufficient to prove that these organic crystals are not stable under the intense radiation of the direct synchrotron beam.

Here we reprint a paper dealing with the first realization of the longstanding idea to protect the XAP crystals from most of the heatload and x-ray intensity from the storage ring by prefiltering the radiation with a synthetic metallic multilayer. We present tests and operating experience of this system with the emphasis on spectroscopic applications.

More information on this work can be found in the publications cited in the list of publications on the first pages of this thesis.

A high resolution soft-x-ray monochromator for synchrotron radiation based on a multilayer/crystal combination

G van der Laan[†], J B Goedkoop[‡] and A A MacDowell[§][||]
[†] Department of Applied and Solid State Physics University of Groningen Nijenborgh 18 9747 AG Groningen The Netherlands
[‡] Research Institute for Materials Catholic University of Nijmegen Toernooiveld 10 6525 ED Nijmegen The Netherlands
[§] Daresbury Laboratory Science and Engineering Research Council Warrington WA4 4AD UK

Received 18 February 1987 in final form 20 May 1987

Abstract. A novel concept for a monochromator in the difficult soft x ray region is described Using a multilayer KAP combination an energy resolution of ~0 8 eV can be obtained for photon energies between 550 1000 eV Its practical value is demonstrated with applications for soft x ray absorption spectroscopy A detailed comparison is given with existing monochromators based on gratings and on double crystals and potential improvements are discussed

1 *Introduction*

The increasing interest in research using vuv soft x ray radiation which is reflected in the advent of dedicated low energy storage rings undulators and free electron lasers has necessitated the development of suitable dispersive elements The soft x ray spectral range contains the K edges of important elements such as O and F and the L edges of 3d transition metals but has often been referred to as a difficult spectral region to monochromatise (see e g Saile and West 1983) Considerable effort is needed to bridge the existing gap ranging from ~400 to 800 eV between grating and crystal monochromators

Recently successful attempts have been reported to extend the use of grating devices to higher energies with a resolving power of 1000 2000 (Peterson 1986 Maezawa *et al* 1986) An alternative approach is to push down the low energy limit of crystal monochromators At the moment this limit is at 790 eV obtained with beryl crystals ($2d = 1\ 595$ nm) Lower energies can be covered with large d spacing organic crystals if there is a way to protect them against the heat load from the intense synchrotron radiation

In an earlier paper we demonstrated the feasibility of soft x ray monochromatisation with an organic crystal preceded by a multilayer acting as a predispersor (van der Laan *et al* 1987) The multilayer consisting of 20 layers of W Re and C in combination with a rubidium acid phthalate (RBAP) crystal ($2d = 2\ 612$ nm) resulted in a resolution of ~1 eV at 800 eV but with a low peak reflectivity of ~10 We predicted an improvement in reflectivity of several orders of magnitude for an optimised multilayer design In this paper we describe the

---

Present address NSLS Brookhaven National Laboratory Upton NY 11973 USA

0022 3735 87 121496 + 07 $02 50

performance of such an optimised multilayer/KAP combination mounted in a conventional double crystal monochromator These crystal monochromators are generally available at most synchrotron radiation centres, which is an important advantage The usefulness of multilayer/KAP is shown by a detailed comparison with state of the art grating and crystal mono chromators Finally we shall discuss some future prospects of this new type of monochromator

2. Concept and basic facts

Multilayer reflecting coatings have been a practical reality in the field of soft x ray optics for about a decade (Henke 1981 Gaponov *et al* 1983) and have even become available on a commercial basis These artificial one dimensional crystals are composed of alternating layers of materials with high and low refractive index Multilayers can be tailored to suit specific demands on d spacing and can survive long periods of exposure to intense synchrotron radiation However, compared with single crystals, their energy resolution is poor, limited primarily by interface roughness and by the effective number of reflecting layers, which is determined by absorption rather than by extinction The application of a double multilayer mono chromator is therefore restricted to high intensity, low resolu tion purposes (Pianetta *et al* 1986, Bruijn *et al* 1986)

On the other hand, there are several organic crystals known with a large d spacing which could offer a good energy resolution The acid phthalate (AP) crystals with d spacings ranging from 1 295 to 1 332 nm can cover energies down to 500 eV, although the strong absorption near the O K edge (532 eV) produces a decrease in reflectivity and in resolution Using the Darwin–Prins model the calculated peak reflectivity of KAP (RBAP) gradually decreases from 14% (18 7%) at 1000 eV to 2% (3 5%) at 550 eV (Henke *et al* 1982) The calculated resolving power changes from 1575 (1330) at 1000 eV to 850 (800) at 550 eV Therefore these crystals are only appropriate for energies above 550 eV They are frequently employed in commercial x ray fluorescence (XRF) spectrometers with conventional x ray anode tubes However these AP crystals are completely destroyed within a few minutes when exposed to the full flux from a low emittance synchrotron source Even in the filtered radiation from a low intensity synchrotron source the AP crystals deteriorate rapidly resulting in a final resolving power of ~250

A concept for monochromatisation using an organic crystal preceded by a multilayer matched in d spacing has the following advantages

(1) The crystal is protected against the high radiation flux by the multilayer which acts as a preselector for energies around the Bragg angle of crystal The heat load on the crystal will be roughly proportional to the band pass of the multilayer

(2) The total energy resolution is determined by the element of the smaller band pass, which is the crystal

In order to have the benefits of a constant deviation exit beam, the multilayer with the crystal can be mounted directly in a double crystal monochromator Because the two Bragg angles are the same the multilayer d spacing has to be equal to a multiple of the crystal d spacing This multiple number determines the order of reflection for the multilayer We found from calculation that multilayers optimised for first and for second order give roughly the same peak reflectivity We have opted for second order reflecting multilayers because the band pass is smaller than in first order A further advantage using the multilayer in second order is that the first order reflection from the multilayer cannot be reflected by the crystal if the wavelength exceeds its $2d$ spacing Therefore no first order contamination is present in the low energy spectrum

Besides the radiation diffracted according to Bragg's law, the multilayer will also reflect all the radiation of which the energy has a critical angle above the given Bragg angle This low energy specular beam can be filtered from the diffracted beam with thin C foils Another solution would be a small offset angle between the Bragg planes and the surface of the organic crystal

On a high energy storage ring the hard x rays have to be eliminated using a premirror Apart from causing possible damage to the multilayer hard x rays are insufficiently absorbed in the coating and can be reflected by the substrate Si(111) in our case

3. Experimental details

Multilayer coatings were obtained from the Institute for Atomic and Molecular Physics (AMOLF), Amsterdam The coatings were deposited by electron beam evaporation (Bruijn *et al* 1985) and consisted of 127 layer pairs of W Re (0 4 nm) and C (2 2 nm), AP crystals were obtained from Quartz and Silice, Paris

Measurements were performed at the 2 GeV storage ring in Daresbury (UK) with typical beam currents between 100 300 mA The experimental set up at beam line 3 4 is schematically sketched in figure 1 A platinum coated mirror (A) at 3° grazing angle rejects the radiation with energy above ~1 5 keV The UV radiation is suppressed with two 450 nm C foils (B) These foils also serve to separate the vacuum of the monochromator (1 μPa) from the storage ring The beam size has been reduced with a diaphragm (F) to a solid angle of $10^{-3}\pi$ mrad^2

The multilayer and the AP crystal were mounted in a Bird and Tole constant deviation monochromator (D) which has an angular range from 10 to 80° A full description of this apparatus will be given elsewhere (MacDowell *et al* 1987) The throughput of the monochromator was optimised by tuning the rocking angle between the multilayer and the crystal The backside of the multilayer was thermally connected with Ga to a water cooled Cu block in order to dissipate the heat load from the beam

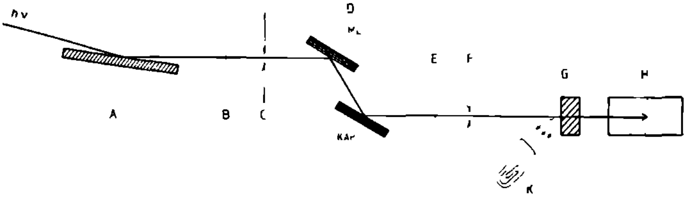

Figure 1 Experimental set up A Pt coated grazing incidence mirror B two 450 nm C foils C horizontal entrance slit of monochromator D constant deviation monochromator equipped with multilayer (ML) and organic crystal (KAP) E 2 5 μm Be window (optional) F diaphragm G sample position H proportional counter used for transmission measurements K electron yield detector used for measurements on bulk samples

Absorption measurements were performed in a separate experimental chamber either in the transmission mode or in the total electron yield mode.

In the transmission mode the photons were counted with a proportional counter (H) filled with an Ar/CO$_2$ mixture at 800 torr (~107 kPa). The entrance window consisted of 4 μm Mylar on a 50% transparent stainless steel support grid. The transmission measurements were done on Ne gas introduced into the chamber using a leak valve. The chamber was separated from the monochromator and the rest of the beam line with a 2.5 μm Be foil (L) allowing for the gas a 50 cm absorption path length.

In the total electron yield mode we measured solid bulk samples either sublimed or scraped clean in vacuum. Electrons emitted from the illuminated surface (G) were collected with a wide angle electrostatic lens into an electron channeltron (K). Standard pulse counting techniques were used to procure the data.

4. Multilayer/KAP throughput

The absolute number of transmitted photons through the multilayer KAP monochromator was measured with the proportional counter. This photon flux corrected for absorption in the Mylar window and support grid is given in table 1 for three different photon energies. Also given in table 1 is the calculated flux emanating from the Pt mirror, the transmittance of the C foils and the reflectance and resolution of the KAP crystal (Henke *et al* 1982). From these numbers we calculated the peak reflectivity of the multilayer. The obtained value increased from 2.1×10^{-4} at 600 eV to 3.8×10^{-4} at 850 eV. This energy dependence for the reflectivity is expected from Fresnel's equation.

The reflectivity obtained can be compared to previous results (van der Laan *et al* 1987). A reflectivity of 8.2×10 at 800 eV was obtained with a combination of RbAP and a 20 period WRe/C multilayer coating in which the layer thickness gradually varied from a quarter wave stack ratio at the bottom to 1.0 nm (WRe) and 1.6 nm (C) at the top. The gain in reflectivity of more than two orders of magnitude for the present optimised 127 period multilayer has three main reasons which are, in order of importance:

(i) smaller perpendicular roughness between the layers

(ii) more layer pairs

(iii) better choice for the layer thickness ratio.

The influence of these factors on the reflectivity has been discussed previously (van der Laan *et al* 1987).

Although the photon flux from the multilayer/KAP *monochromator is rather low compared with a double crystal* monochromator, a sufficient count rate can be obtained for a sensitive detecting device such as a proportional counter or a channeltron.

Table 1. The input and output flux of the multilayer KAP monochromator for different photon energies. The peak reflectivity of the multilayer has been calculated from these numbers using the tabulated values for the carbon foils and the KAP crystal.

	Photon energy (eV)		
	600	700	850
Photon flux behind Pt mirror† ($\times 10^{11}$)	3.4	3.4	3.3
Photon flux behind monochromator† ($\times 10^{4}$)	2	9	33
Transmittance of C foil at 900 nm‡	0.17	0.31	0.50
Percentage peak reflectance of KAP‡	2.61	4.29	8.32
Energy resolution of KAP (eV)‡	0.64	0.63	0.63
Peak reflectivity obtained for the multilayer ($\times 10^{-4}$)	2.1	3.2	3.8

† In photon s/0.1 A/eV band pass 10 [illegible] mrad at 2 GeV

‡ From Henke *et al* (1982)

5. Resolution

In this section the energy resolution for some multilayer crystal combinations will be determined using the measured linewidth of the Ne K and La M_5 absorption edges.

In figure 2 the absorption spectrum of Ne at a pressure of ~0.1 torr (13.3 Pa) is shown as measured with multilayer KAP. The cross section has been calibrated with data from Marr and West (1976). The first peak at 867.25 eV is the 1s → 3p transition (Wuilleumier 1970). Also the 1s → 3p transition at ~1.5 eV higher energy is visible just below the continuum. The full width of the 1s → 3p line is equal to 1.0 eV measured as two times the left half width. The intrinsic width of this line is ~0.3 eV (Esteva *et al* 1983). Without making assumptions on the line shapes the experimental resolution will be equal to 0.8 ± 0.1 eV. This result is in agreement with the theoretical prediction because the calculated Darwin–Prins width for KAP is equal to 0.63 eV (Henke *et al* 1982) and convoluted with a beam divergence of about 20″ we obtain the experimental value.

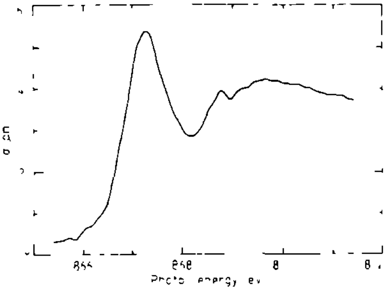

Figure 2. Ne K absorption structure measured with multilayer KAP (100 pm^2 = 1 Mb (megabarn)).

The La $M_{4,5}$ absorption spectrum of LaF$_3$ measured in total yield and using multilayer KAP is shown in figure 3. A normalised spectrum obtained with beryl crystals is given for comparison. The data show the three dipole allowed $3d^{10}4f^0 \to 3d^9 4f^1$ transitions: a very weak line at ~830 eV, a sharp M_5 line at 834.2 eV and an asymmetrical M_4 line at 850.5 eV. The latter is broadened by Fano interaction (Thole *et al* 1985a). The La M_5 line which is best suited for determination of the energy resolution has an intrinsic width of 0.8 eV (Thole *et al* 1985a). Multilayer KAP results in a FWHM of 1.5 eV. The value for the experimental resolution equal to 0.8 ± 0.1 eV as derived above is in agreement with the fact that both the KAP rocking curve (Liefeld *et al* 1970) and the intrinsic La M_5 line (Thole *et al* 1985a) have mainly a Lorentzian line shape. We can further see from figure 3 that the spectral purity for multilayer KAP is high. There are no ghost lines or peak deformations observed in the spectrum.

Also resolution measurements were performed on a multilayer RbAP combination. In this case the width of the La

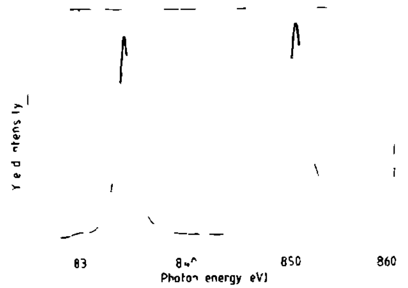

Figure 3 The La M_{4} absorption structure of LaF_{3} measured with multilayer KAP (complete spectrum) and with beryl (1010) crystals (inserted peaks)

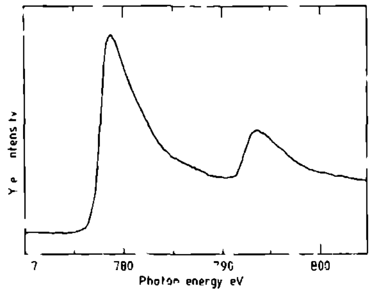

Figure 4 Co L_{2} absorption spectrum measured with multilayer/KAP

M line was equal to 1 65 eV which agrees with the calculated value of the Darwin–Prins width for RBAP (0 70 eV) Use of a RBAP crystal with an offset angle of I between the crystal's front face and the reflecting Bragg planes resulted in a somewhat larger La M width equal to 1 88 eV This decrease in resolution must be ascribed to distortions in the structure at the surface due to the manufacturing process

6 Applications

Possible applications can be found in various kinds of high resolution studies in the soft x ray spectral region such as photoelectron spectroscopy Cooper minima spectroscopy x ray absorption near edge structure (XANES) resonant photoemission and magnetic dichroism Here we will demonstrate the practical use of multilayer KAP with examples from the field of soft x ray absorption spectroscopy

6 1 The L absorption structure of 3d transition metal compounds

The 3d transition metal compounds display strong features at the L edges which are often referred to as white lines for historical reasons associated with the use of photographic plates for x ray spectra These features are transitions $2p^{6}3d^{n}$ $2p$ $3d^{n}$ ^{1} which are distributed over a short energy range of only a few eV due to the narrow bandwidth of the 3d states They are split in 2p (L) and 2p (L) by the spin orbit interaction Because of the narrow width of the 2p core levels (< 1 eV) high resolution L absorption spectra can reveal information about the distribution of 3d states above the Fermi level Not many of these studies have yet been performed owing to the lack of proper monochromatising elements Only the Ni L edges are well documented because they can be covered by beryl (see e g van der Laan *et al* 1986 and references therein) Electron energy loss spectroscopy (EELS) can be used to measure other 3d metals One important disadvantage of this technique is the necessity for thin films 50 to 100 nm thick (see e g Fink *et al* 1985) whereas total yield measurements using synchrotron radiation can be performed on bulk samples

The Co L absorption spectrum of the pure metal is shown in figure 4 There is a good agreement with the EELS data of Fink *et al* (1985) although the latter have better resolution The steep slope at the onset of these edges reflects the Fermi level in the metal The structure above the edges is mainly due to the dispersion of the empty 3d bands

The Fe L spectra of a haematite (αFe O) holmium iron garnet (Ho Fe O) magnetite (Fe O_{4}) pyrite (FeS) and Fe metal are shown in figure 5 The iron sites in these compounds

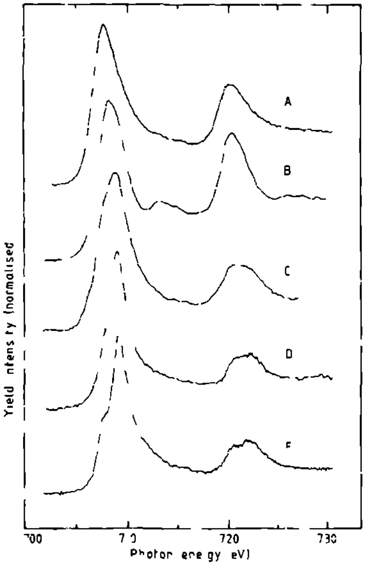

Figure 5 The Fe L_{2} absorption structures of various iron compounds measured with multilayer KAP A pure iron B pyrite (FeS_{2}) C magnetite (Fe O_{4}) D holmium iron garnet (Ho Fe O_{12}) E haematite (αFe O)

differ in valency spin configuration and symmetry Comparison of the experimental spectra with multiplet calculations can result in quite accurate values for physical quantities such as the spin–orbit crystal field Coulomb and exchange parameters (Yamaguchi *et al* 1982 van der Laan 1987 Thole *et al* 1985b) For instance αFe O and Ho Fe O are both high spin Fe compounds The irons in the sesquioxide have octahedral symmetry whereas the irons in the garnet are located in octahedral and tetrahedral lattice positions As seen in figure 5 their spectra are distinctly different especially near the L onset which is almost entirely caused by the crystal field

As a final example the Mn L spectrum of MnSi a weak itinerant ferromagnet is shown in figure 6 This proves that also near 600 eV data can be taken with good statistics

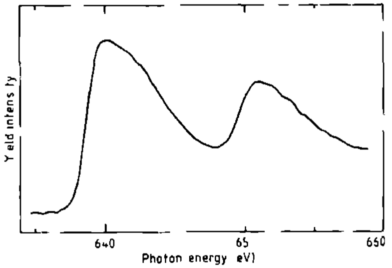

Figure 6 The Mn $L_{2,3}$ absorption spectrum of MnSi measured with multilayer/KAP

6 2 *XANES of the fluorine K edge*

In figure 7(*a*) is shown the F K absorption spectrum of CaF an important insulating material e g used to sandwich integrated circuits There is a good agreement with other reported data such as from Zimkina and Vinograd (1971) and Himpsel *et al* (1986) Recently Oizumi *et al* (1985) obtained F K spectra with very high resolution Their data for CaF measured with a 10 m grazing incidence grating monochromator is reproduced for comparison in figure 7(*b*)

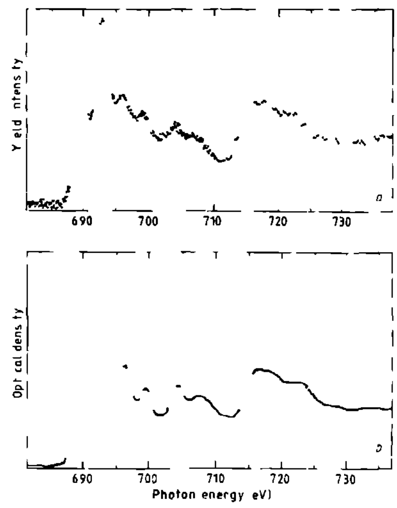

Figure 7 The fluorine K absorption spectrum CaF_2 (*a*) measured with multilayer KAP (4s point) (*b*) data reproduced from Oizumi *et al* (1985) as measured with the 10 m GIM at the Photon Factory (2400 line mm 10 μm slit)

7 Appraisal of other monochromator devices

There are various kinds of dispersive elements which can be used with a fixed direction exit beam such as reflection gratings crystals multilayers zone plates and transmission gratings (Saile and West 1983) The last two classes are both fragile and not commercially available and therefore not widely used In order to make a comparison possible with multilayer/crystal combinations we will discuss the performance of some operational monochromators based on gratings and crystals and discuss their capabilities and limitations

7 1 *Grating monochromators*

Gratings are normally used for energies below the C K edge However strong efforts have been made to extend their use to higher energies (Stohr *et al* 1980) and to improve their resolution (Petersen 1986 Maezawa *et al* 1986) Limiting factors are the source size the optical quality of the beam line elements stray light background higher order contributions from diffracting elements build up of carbon contamination heat load from the x ray flux and the high manufacturing costs

In the soft x ray region the efficiency of a single grating is roughly 10 However the throughput of the total device is reduced by the slit size and since losses are associated with each reflection the number of mirrors employed to maintain the focal point fixed in a large energy range (Johnson 1986) It is difficult to obtain higher resolving powers than 1000 although there are a few outstanding exceptions

The SX 700 plane grating monochromator at BESSY Berlin covers the soft x ray spectral range up to 2 keV (Petersen 1982 1985 1986) The source size limited spectral resolution can only be obtained when the influence of the large tangent error in the present focusing mirror is eliminated by aperture reduction Changing the ellipsoidal mirror for a spherical mirror would also reduce these slope errors as is proposed in the design of the monochromator for beam line 1 at the SRS Daresbury (Padmore 1986) Using the full ellipsoidal mirror together with a 1200 line mm holographic grating the SX 700 monochromator gives for La Al a La M linewidth equal to 3 3 eV (FWHM) Reducing the aperture and using an exit slit of 10 μm the La M linewidth decreases to 1 3 eV and for the Ne K edge a width of 1 0 eV has been obtained (table 2) The ultimate resolution is estimated to be 4 meV at 12 eV increasing to 800 meV at 850 eV with a functional dependence on photon energy that varies as *E*

Another high resolution grating device is the 10 m grazing incidence monochromator (GIM) at the Photon Factory in Japan (Maezawa *et al* 1986) Using a 2400 line mm grating and a 5 μm slit size a Ne K linewidth of 0 5 eV has been obtained Spectra of the fluorine K edge and the 3d transition metal L edges in the fluorides have been reported with a resolution of 0 4 eV (Nakai *et al* 1985 1986 Oizumi *et al* 1985)

Finally we mention the 10 m 172 toroidal grating

Table 2 Experimentally obtained widths of the Ne K and La M lines and theoretical resolution for grating double crystal and multilayer XI monochromators Intrinsic line widths are 0 3 eV for Ne K and 0 8 for La M

Monochromator	Linewidth FWHM (eV) Ne K	Linewidth FWHM (eV) La M	Theoretical resolution (eV) at ~ 850 eV
SX700 BESSY (1200 line mm 10 μm slit)	1 0^a	1 3^b	0 8^h
10 m GIM Photon Factory	0 5^c		0 4
Double beryl (1010)	0 5	0 9^g	0 3 ± 0 1^h
Multilayer/KAP	1 0^h	1 5^h	0 63
Multilayer/RBAP		1 65^h	0 70^i

(a) Peterson (1985) (b) Peterson (1986) (c) full aperture gives 3 3 eV (d) Maezawa *et al* (1986) (e) Oizumi *et al* (1985) (f) Esteva *et al* (1983) (g) this work (h) Thole *et al* (1985a) (i) Henke *et al* (1982) monochromator (TGM) from IBM at the NSLS in Brookhaven. At the fluorine K edge the resolution is about 0.8 eV.

7.2 *Crystal monochromators*

Although there are many different crystals known with a large d spacing (>0.8 nm) their potential use in bright synchrotron radiation has never been demonstrated (Alexandropoulos and Cohen 1974, Bertin 1975, Wong *et al* 1982, Hussain *et al* 1982). The main difficulties are heat load and chemical decomposition. Beryl (10$\bar{1}$0) is the only well established crystal which can go down in energy to 790 eV leaving the other frequently used crystals α quartz (10$\bar{1}$0) (>1479 eV), InSb(111) (>1683 eV) and Ge(111) (>1922 eV) far behind.

The resolution of the double beryl monochromator at 850 eV is equal to 0.3 ± 0.1 eV as estimated from rocking curve measurements (van der Laan *et al* 1987). The Ne K width obtained is equal to 0.5 eV (Esteva *et al* 1983) and the La M_5 width obtained is equal to 0.9 eV (Thole *et al* 1985b).

Wide energy scans such as are necessary in EXAFS for instance are complicated when the crystals have a poor heat conductivity as is the case for beryl and quartz. The imposed heat load makes the d spacing of the first crystal strongly dependent on the Bragg angle. The rocking angle needs a constant adjustment during the scan in order to maintain the Bragg condition for both crystals (Greaves *et al* 1983).

Like all crystals beryl shows intense glitches in its reflection spectrum. In the (0001) plane of incidence beryl (10$\bar{1}$0) displays a glitch at 898 eV (van der Laan and Thole 1987). Near 1072 eV a large absorption is observed from Na present as a spurious element in natural beryl. Mg, Zn and Fe are also frequently present as impurities.

7.3 *Comparison to multilayer/KAP*

In table 2 we summarised the resolution data quoted for some grating, crystal and multilayer/crystal monochromators. Of course above 790 eV beryl offers the best resolution. However multilayer/KAP can be useful in energy regions where beryl suffers from spurious reflection or absorption.

It is seen from table 2 that where energy resolution is concerned the multilayer KAP monochromator is competitive with the latest generation of grating monochromators.

8. Conclusions

We have shown that a multilayer/KAP combination can be used in the 550–1000 eV range for spectroscopic purposes. It offers a high spectral purity and a resolution of 0.8 ± 0.1 eV. This performance is about as good as can be obtained with new types of grating monochromators, such as the SX700 at BESSY in Berlin. We know of only one grating device which gives a much better source size limited resolution, namely the 10 m GIM at the Photon Factory in Japan.

Although multilayer/KAP has inferior resolution when compared with beryl it can be used to avoid the tedious adjustments on the rocking angle and the spurious structures in beryl.

The desired photon flux depends of course on the specific application. In our examples of absorption spectra the count rate was sufficient to cover the complete dynamic range of the proportional counter and the electron channeltron. More photon flux was not necessary and in some cases even undesirable. For the study of processes with a weak x ray response the efficiency of the monochromator must be larger. At present the efficiency is reduced by the multilayer's poor peak reflectivity ($\sim 10^{-4}$) mainly due to the interfacial layer roughness. Reduction of this roughness is therefore of utmost importance and would be feasible by using sputtering deposition techniques and by cooling the substrate.

A multilayer/crystal combination directly mounted in a double crystal monochromator merits consideration if one pursues a simple configuration. However higher throughput and resolution can be obtained in more complicated arrangements which consist of at least three diffracting elements. One promising solution would be to use a laterally graded multilayer in front of two organic crystals. At a fixed exit angle the energy variation is achieved with one linear movement of the graded multilayer. Operating the multilayer at a small glancing angle the reflectivity will be very high. The combination of this graded multilayer with two KAP crystals rather than with one will give an improvement of 1.5 in resolution (DuMond 1937).

Moreover other crystals which have not been tested yet are predicted to give even higher resolution than KAP. Theoretically the FWHM resolution of a double crystal combination using sodium or ammonium acid phthalate must be about 0.3 eV at 700 eV (Henke *et al* 1982).

Acknowledgments

The authors would like to thank G A Sawatzky, J C Fuggle, B T Thole, W J Myring, J B West, H A Padmore, C M B Henderson, J Verhoeven, H van Brug, R van der Pol and the Daresbury technical staff for valuable contributions. This work was supported by the Netherlands Foundation for Chemical Research (Stichting Scheikundig Onderzoek Nederland) with financial aid from the Netherlands Organisation for the Advancement of Pure Research (Stichting Zuiver Wetenschappelijk Onderzoek).

References

Alexandropoulos N G and Cohen G G 1974 Crystals for stellar spectrometers
Appl Spectrosc **28** 155

Bertin E P 1975 *Principles and Practice of X ray Spectrometric Analysis* (New York: Plenum)

Bruijn M P, Chakraborty P, van Essen H, Verhoeven J and van der Wiel M J 1985 Automatic deposition of multilayer x ray coatings with laterally graded d spacing
SPIE Proc **563** 36

Bruijn M P, Verhoeven J, van der Wiel M J, van der Laan G, Goedkoop J B, Fuggle J C and MacDowell A A 1986 Characterization of multilayers as monochromators using 200–900 eV synchrotron radiation
Nucl Instrum Meth Phys Res A **253** 135

DuMond J W M 1937 Theory of the use of more than two successive x ray crystal reflections to obtain increased resolving power
Phys Rev **52** 872

Esteva J M, Gauthe B, Dhez P and Karnatak R C 1983 Double excitation in the K absorption spectrum of neon
J Phys B At Mol Phys **16** L263

Fink J, Muller Heinzerling Th, Scheerer B, Speier W, Hillebrecht F U, Fuggle J C, Zaanen J and Sawatzky G A 1985 2p absorption spectra of the 3d elements
Phys Rev B **32** 4899

Gapanov S V, Garin F V, Gusev S L, Kochemasov A V, Platonov Yu Ya and Salashchenko N N 1983 Multilayer mirrors for soft x ray and vuv radiation
Nucl Instrum Meth **208** 227

Greaves G N, Diakun G P, Quinn P D, Hart M and Siddens D P 1983 An order sorting monochromator for synchrotron radiation
Nucl Instrum Meth **208** 335

Henke B L 1981 Low energy x ray spectroscopy with crystals and multilayers
AIP Conf Proc **75** 85

Henke B L Lee P Tanaka T J Shimabukuro R L and Fujikawa B K 1982 Low energy x ray interaction coefficients photoabsorption scattering and reflection
At Data Nucl Data Tables **27** 1

Himpsel F J Karlsson U O Morar J F Rieger D and Yarmoff J A 1986 Determination of interface states for CaF Si(111) from near edge x ray absorption measurements
Phys Rev Lett **56** 1497

Hussain Z Umbach E Shirley D A Stohr J and Feldhaus J 1982 Performance and application of a double crystal monochromator in the energy region $800 < h\nu < 4500$ eV
Nucl Instrum Meth **195** 115

Johnson R L 1986 Grazing incidence monochromators for synchroton radiation – a review
Nucl Instrum Meth Phys Res A **246** 303

van der Laan G 1987 Mixed electronic states and magnetic moments studied with near edge x ray absorption spectroscopy
Giant Resonances in Atoms Molecules and Solids
(Nato Advanced Study Institute Series) ed R C Karnatak J M Esteva and J P Connerade (New York Plenum) pp 445 60

van der Laan G Goedkoop J B Fuggle J C Bruijn M P Verhoeven J van der Wiel M J MacDowell A A West J B and Munro I H 1987 Soft x ray monochromatisation using a multilayer single crystal combination
Daresbury Sci Rep DL SCI P522E also
Nucl Instrum Meth Phys Res A **255** 592

van der Laan G and Thole B T 1987 Determination of glitches in soft x ray monochromator crystals
Nucl Instrum Meth Phys Res A **255** in press

van der Laan G Zaanen J Sawatzky G A Karnatak R C and Esteva J M 1986 Comparison of x ray absorption with x ray photoemission of nickel dihalides and NiO
Phys Rev B **33** 4253

Liefeld R J Hanzely S Kirby T B and Mott D 1970 X ray spectrometric properties of potassium acid phthalate crystals
Adv X ray Anal **13** 373

MacDowell A A West J B and van der Laan G 1987 The soft x ray monochromator at Daresbury
To be published

Maezawa H Nakai S Mitani S Noda H Namioka T and Sasaki T 1986 A 10 m grazing incidence monochromator for high resolution soft x ray spectroscopy at the Photon Factory
Nucl Instrum Meth Phys Res A **246** 310

Marr G V and West J B 1976 Absolute photoionization cross section tables for helium neon argon and krypton in the VUV spectral regions
At Data Nucl Data Tables **18** 497

Nakai S Ogata K Ohashi M Sugiura C Mitsuishi T and Maezawa H 1985 Multiplet structures in the L absorption spectra of 3d transition metal fluorides
J Phys Soc Japan **54** 4034

Nakai S Ohashi M Mitsuishi T Maezawa H Oizumi H and Fujikawa T 1986 F K XANES studies of alkaline earth fluorides
J Phys Soc Japan **55** 2436

Oizumi H Fujikawa T Ohashi M Maezawa H and Nakai S 1985 F K XANES studies of alkaline earth fluorides
J Phys Soc Japan **54** 4027

Padmore H A 1986 The use of spherical optics in high resolution soft x ray grating monochromators
Daresbury Sci Rep DL SCI P518E

Petersen H 1982 The plane grating and elliptical mirror a new optical configuration for monochromators
Opt Commun **40** 402

Petersen H 1985 Gold N EXAFS Messungen am SX 700 BESSY
Jahresber 1985 p136

Petersen H 1986 The high energy plane grating monochromator at BESSY
Nucl Instrum Meth Phys Res A **246** 260

Pianetta P Barbee T W Jr and Redaelli R 1986 Performance of layered synthetic microstructures in monochromator applications in the soft x ray region
Nucl Instrum Meth Phys Res A **246** 352

Saile V and West J B 1983 VUV and soft x ray monochromators for use with synchrotron radiation
Nucl Instrum Meth **208** 199

Stohr J Jaeger R Feldhaus J Brennan S Norman D and Apai G 1980 Extended absorption fine structure studies above the carbon nitrogen oxygen and fluorine absorption edges
Appl Opt **23** 3911

Thole B T Cowan R D Sawatzky G A Fink J and Fuggle J C 1985b New probe for the ground state electronic structure of narrow band and impurity systems
Phys Rev B **31** 6856

Thole B T van der Laan G Fuggle J C Sawatzky G A Karnatak R C and Esteva J M 1985a 3d x ray absorption lines and the $3d^9 4f$ multiplets of the lanthanides
Phys Rev B **32** 5107

Wong J Roth W L Batterman B W Berman L E Pease D M Heald S and Barbee T 1982 Stability of some soft x ray monochromator crystals in synchrotron radiation *Nucl Instrum Meth* **195** 133

Wuilleumier F 1970 K absorption discontinuity of neon
C R Acad Sci B **270** 825

Yamaguchi T Shibuya S Suga S and Shin S 1982 Inner core excitation spectra of transition metal compounds II p d absorption spectra
J Phys C Solid State Phys **15** 2641

Zimkina T M and Vinogradov A S 1971 X ray spectra and energy band structure of alkali flourides
J Physique Coll **32** 4278

Nuclear Instruments and Methods in Physics Research A275 (1989) 435 441
North Holland Amsterdam

EXPERIMENTAL RESOLUTION IN SOFT X-RAY MONOCHROMATORS

S W KORTBOYER, J B GOEDKOOP, F M F DE GROOT, M GRIONI * and J C FUGGLE

Research Institute for Materials University of Nijmegen Toernooiveld 6525 ED Nijmegen The Netherlands

H PETERSEN

Berliner Elektronenspeicherring Gesellschaft für Synchrotronstrahlung mbH (BESSY) Lentzeallee 1000 D 100 Berlin 33 Germany

Received 22 September 1988

In order to facilitate the quantative estimation of monochromator instrument functions we present series of X ray absorption spectra which have been broadened with different Gaussian and Lorentzian functions These permit assessment of the instrumental broadening at ~ 510 ~ 710 and ~ 850 eV We illustrate the use of our curves with X ray absorption spectra from grating monochromators and also from double crystal monochromators fitted with beryl and multilayer/KAP and multilayer/multilayer pairs as the dispersive elements

1. Introduction

The purpose of this work was to investigate simple empirical methods to estimate the resolution of soft X-ray monochromators for synchrotron radiation We expect these methods to be applicable to the soft X-ray monochromators which are increasingly finding use for X-ray absorption (XAS) extended X-ray absorption fine structures (EXAFS) X-ray photoemission spectroscopy (XPS) etc utilising synchrotron radiation

In general XAS EXAFS and XPS spectra are a fold of the shape of the monochromator output the Lorentzian broadening due to the core hole lifetime and the spectral function which contains the required information (In XPS there is also a contribution from the electron energy analyser) It is the first of these quantities the instrument function of the monochromator which is of interest here Various approaches are used in the literature to measure the monochromator instrument function for instance for double crystal monochromators an upper limit for the resolution can be determined from the measured rocking curves [1 2] Another approach is to measure the full width at half maximum (FWHM) of a known peak in the XAS spectrum (e g the Ne 1s or La 3d peaks) and subtract the intrinsic peak width If the intrinsic lineshape is well known this procedure should yield the FWHM of the instrument function [3 5] Another criterion sometimes used is to consider the 10–90% energy width of a steplike feature

In our own work on developing new monochromators and dispersive elements (see e g refs [1 4 6 7]) and in simply measuring XAS data we have frequently found these methods unsatisfactory The above methods are either based on unreliable assumptions or are complicated to perform In practice frequent changes of beam position and size in synchrotron storage rings and the requirement to change spectral regions frequently preclude a complete study of the monochomator instrument function Indeed it is often not even cost effective to completely optimise the monochromator performance because of the short times available for experimentation There is thus a definite need for a simple, reproducible method for day-to-day use on synchrotrons where the beam dimensions and position may change quite frequently, or where one needs to measure the performance of new optical elements at a variety of energies

In response to this need we have investigated methods based on comparison of XAS spectra of the $L_{2,3}$ edges of the 3d transition metals measured in a simple total yield mode with standard spectra which have been broadened to simulated the various possible instrument functions These measurements only require a channeltron and a method for cleaning the sample surface and can be easily performed in a standard UHV apparatus As references we use high resolution electron energy loss (HRELLS) spectra [8] because these seem to be amongst the best and most reliable spectra at present available in the range of 500–1000 eV [9] In the soft

---

* Postal address Laboratoire pour l Utilisation du Rayonnement Electromagnetique (LURE) F 91405 Orsay Cedex France

0168-9002/89/$03 50 Elsevier Science Publishers B V
(North-Holland Physics Publishing Division)

X-ray energy range. HREELS spectra give the same information as XAS, as long as the conditions in HREELS are chosen to analyse only losses with low momentum transfer so that the small angle approximation is valid [10,11]. We will discuss here the influence of two different instrumental broadening functions, i.e. Lorentzian and Gaussian, and present data in a form suitable for use by others.

2. Simulation of the instrumental broadening

A Gaussian curve has the form

$$I(E) = I_0(E_0)\exp\left[-(E-E_0)^2/2\sigma^2\right]$$

where I is the intensity and E_0 is the energy of the peak centroid. In the literature it is common to designate broadenings by the FWHM which is 2.354σ. When two Gaussian curves are folded the values of σ and FWHM add quadratically, i.e.

$$\sigma_{\mathrm{tot}} = \left(\sigma_1^2+\sigma_2^2\right)^{1/2}$$

or

$$\mathrm{FWHM}_{\mathrm{tot}} = \left(\mathrm{FWHM}_1^2+\mathrm{FWHM}_2^2\right)^{1/2}$$

The Lorentzian lineshape has the form

$$I(E) = I_0(E_0)\Gamma_L/\left[(E-E_0)^2+\Gamma_L^2\right]$$

so that the FWHM is 2Γ. In contrast to the Gaussian curves the widths of folded Lorentzian curves add arithmetically.

There is no simple formula for folding together Gaussian and Lorentzian broadening and they must be folded numerically in order to form the curves sometimes known as Voigt profiles [12]. In the following account we restrict ourselves to consideration of pure Gaussian or Lorentzian broadening.

We numerically broadened the HREELS spectra which acted as our standards with Gaussian or Lorentzian broadening functions. To test both our programs and the computer simulations of the HREELS instrument function we took two EELS spectra of Fe. For these spectra the resolution (FWHM) was determined by Fink et al. to be 0.2 eV [13] and 0.6 eV [8]. The 0.2 eV resolution spectrum was convoluted to get a broadened EELS spectrum with a total resolution of 0.6 eV. The match between the broadened EELS spectrum and the recorded spectrum with the 0.6 eV resolution was perfect proving that the instrumental function of the EELS spectrometer indeed is a Gaussian. It is important to know the instrumental contribution to the standard spectra because it will contribute to all our simulated spectra.

For this paper we selected the three transition metal $L_{2,3}$ XAS spectra with the sharpest features and which gave the best results in determining the resolution. Figs. 1, 2 and 3 show the original EELS spectra (bottom of the drawing) and curves with different broadenings (solid lines) of V, Fe and Ni respectively. The numbers on the right in the drawings are the total Gaussian broadenings (FWHM in eV) of the curves. The vanadium EELS spectrum (fig. 1) consists of two peaks, the L_3 and L_2 absorption edges, the L_3 peak having a shoulder on the low energy side. The onset of the shoulder starts at an energy of 511.7 eV. As the broadening is increased (going up in fig. 1) the shoulder is no longer noticeable in the spectrum. The appearance of the shoulder is a good indication for the resolution in the range of 0.2–1.0 eV (FWHM) and makes V our first choice for characterizing high resolution monochromators. It is also clear that the relative heights of the two peaks changes for different total Gaussian broadenings. This is because the L_3 lifetime broadening is less than for L_2. Thus it loses height more quickly when an extra instrumental broadening is added. This change in relative height would be a good guide for determining the energy resolution between 1.0 eV and approximately 4.0 eV, but is extremely dependent on the background slope. This indication is thus unreliable. In this resolution range it is better to compare the overall shape of the L_3 peak with the standard spectra in fig. 1. We also see that the apparent peak separation decreases at poorer

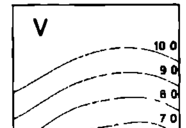

Fig. 1. Dotted curve: the V $L_{2,3}$ EELS spectrum [13] with instrumental broadening of 0.2 eV FWHM. Solid lines: the same spectrum with extra Gaussian broadening. The numbers on the right give the total Gaussian broadening (FWHM).

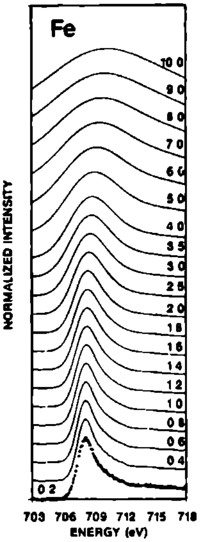

Fig 2 Dotted curve the Fe L_3 EELS spectrum [13] with instrumental broadening of 0 2 eV FWHM Solid lines the same spectrum with extra Gaussian broadening The numbers on the right give the total Gaussian broadening (FWHM)

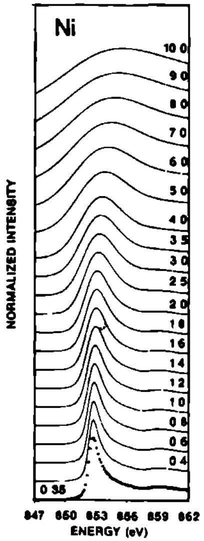

Fig 3 Dotted curve the Ni L_3 EELS spectrum [13] with instrumental broadening of 0 35 eV FWHM Solid lines the same spectrum with extra Gaussian broadening The numbers on the right give the total Gaussian broadening (FWHM)

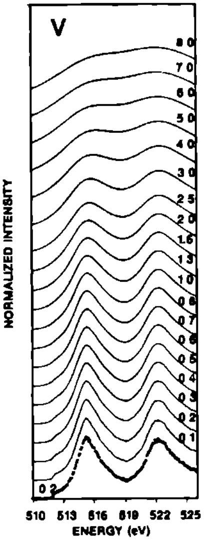

Fig 4 Dotted curve the V $L_{2,3}$ EELS spectrum [13] with instrumental broadening of 0 2 eV FWHM Solid lines the same spectrum with extra Lorentzian broadening (FWHM) as shown by the numbers on the right

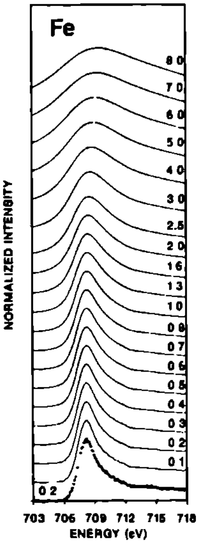

Fig 5 Dotted curve the Fe L_3 EELS spectrum [13] with instrumental broadening of 0 2 eV FWHM Solid lines the same spectrum with extra Lorentzian broadening (FWHM) as shown by the numbers on the right

energy resolutions At a total Gaussian broadening of approximately 8 0 eV only a single broad feature is seen

Because of the larger spin–orbit splitting in the Fe and Ni spectra (figs 2 and 3), we show only the L_3 peaks The Fermi level (or XAS threshold) is at 706 6 eV in the Fe EELS spectrum and at 851 9 eV in the Ni spectrum At the bottom both figures show the original EELS spectrum of the L_3 absorption edge which consists of an asymmetric peak with a steep edge on the low energy side This edge shifts on broadening towards higher energies, becomes less pronounced, and is a fine indication of the resolution In comparing the experimental spectra with the reference spectra we also considered the total FWHM of the L_3 peak These give a good indication of the experimental resolution only up to a total energy resolution of approximately 3 5 eV for Fe and Ni, because at poorer resolutions there are some scaling problems As seen in figs 2 and 3 at poor resolutions the low energy end of the broadened spectra are cut by the frame of the figure before they fall of to zero intensity

The effects of applying a Lorentzian broadening to the $L_{2,3}$ XAS spectra of V, Fe, Ni are shown in figs 4, 5 and 6, where the numbers on the right hand side give only the FWHM of the Lorentzian broadening applied (exclusive core hole lifetime broadening) At first sight the observed trends are rather similar to those found for Gaussian broadening However closer examination reveals some differences In particular the long tail of the Lorentzian function causes small details in the wings of a peak to become less distinct with smaller broadening than for Gaussian curves This may be seen if, for instance, the 511 7 eV shoulder at 0 4 eV Lorentzian broadening is compared with that at 0 8 eV Gaussian broadening Also Lorentzian broadening is noticeable in the relative heights of the L_2 and L_3 peaks sooner than for Gaussian broadening Note, for instance that the two maxima have equal height at ~ 0 3 eV Lorentzian broadening or 0 8 eV Gaussian broadening However as we shall see below it is not always easy to distinguish experimentally a Lorentzian machine function from a broader Gaussian function

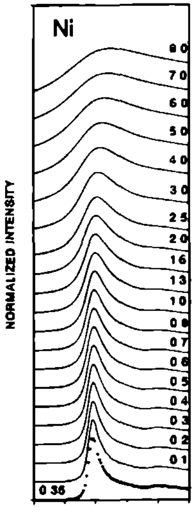

Fig 6 Dotted curve the Ni L_3 EELS spectrum [13] with instrumental broadening of 0 35 eV FWHM Solid lines the same spectrum with extra Lorentzian broadening (FWHM) as shown by the numbers on the right

3. Experimental

The broadened EELS data were compared with XAS data recorded with several monochromators The SX700 grating monochromator (10–2000 eV) at BESSY in Berlin was used for the L_3 edges of Sc to Ni The resolution of this monochromator depends critically on the exit slit and the source beam stability The spectra were recorded with an exit slit of 10 μm and a 1200 lines/mm grating Optical design, performance and operation of this monochromator is discussed by Petersen [14–16] Very recently and after the data discussed here were taken – performance has been strongly further improved by the replacement of the old SX700 elliptical focussing mirror (tangent error 3 arcsec) by a new one (tangent error 0 92 arcsec [17])

We also used XAS data recorded with the SOXAFS monochromator (Daresbury UK) and with the KMC double crystal monochromator (BESSY, Berlin, Germany) Both monochromators were equiped with either two beryl crystals (for use above ~ 800 eV) and a multilayer/KAP (ML/KAP) combination (for use above ~ 600 eV) In the latter configuration the second order reflection of the multilayer was used as a bandpass filter for the KAP as discussed in refs [4 18] The matched multilayers consisted of 200 double layers of W and Si ($2d = 53 2$ Å Ovonics Synthetic Materials) In Daresbury and BESSY experiments with a combination of two multilayers consisting of 181 layers of Ni and C of 22 Å thickness (supplied by FOM-Institute for Atomic and Molecular Physics Amsterdam The Netherlands) were also performed More information on these experiments can be found in refs [6 7]

4. Comparison with experiment

The XAS spectrum of vanadium recorded with the SX700 grating monochromator is shown in fig 7, to-

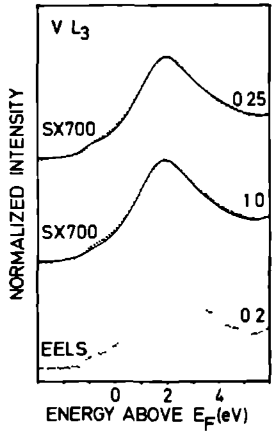

Fig. 7. V EELS spectrum (bottom curve) and the V XAS spectrum recorded with the SX700 grating monochromator (middle and upper dotted curve). The solid lines through the curves are the broadened EELS spectra with respectively Gaussian broadening (middle curve: total FWHM 1.0 eV) and with Lorentzian broadening (upper curve: Lorentz contribution of 0.25 eV FWHM).

gether with the EELS spectrum. The lines through the SX700 spectra are the broadened EELS curves which give the best match (see also table 1). Only the L_3 peak of the vanadium spectrum is taken into consideration because the (small) uncertainty in the background in EELS spectra results in large uncertainties in the L range.

An EELS curve with a total Gaussian broadening of 1.0 eV (FWHM) gives a good match for the overall width of the line (middle curve in fig. 7). But as seen from the figure the valence band structure at the shoulder of the L_3 peak is poorly reproduced. One can clearly see that the instrumental broadening function should have more a tail character. In the top curve of fig. 7 a Lorentzian broadening function of 0.25 eV (FWHM) was taken which means that the total FWHM of the resulting broadening function including the V L_3 lifetime broadening is 0.35 eV. Although the match is not entirely perfect it is better at the shoulder of the L_3 peak. This suggests that the instrumental function of the monochromator cannot be represented with a pure Gaussian in this case. Note that the FWHM found with a Lorentzian broadening (total FWHM 0.35 eV of *which 0.25 eV is from the Lorentzian broadening*) is much smaller than the Gaussian FWHM (1.0 eV) needed for the best simulation.

Fig. 8 shows the XAS data for Fe together with the broadened EELS curves (solid lines). For the ML/KAP and ML/ML data as well as for the SX700 data we do get a good match with just a Gaussian broadening. The numbers on the right in the drawing show the FWHM (in eV) of the total Gaussian broadening of the EELS curves. The match between the broadened EELS curve and the ML/ML data fails at the end of the spectrum (top curve in fig. 8) because the contribution of the L_2 edge has been neglected.

Table 1

Best values for the FWHM of Gaussian and Lorentzian instrumental broadening function (in eV) under various conditions.

Monochromator	Energy (eV)	Gauss FWHM	Lorentz FWHM $^{a)}$
Beryl beryl	~850	0.85	0.2
Grating	~510	1.0	0.25
Grating	~710	1.6	0.9
Grating	~850	1.15	0.6
ML KAP	~710	1.6	0.9
ML KAP	~710	1.9	1.3
ML ML	~710	6.8	6.0

With a Gaussian contribution of between 0.2 and 0.35 eV from the EELS measurements (see text).

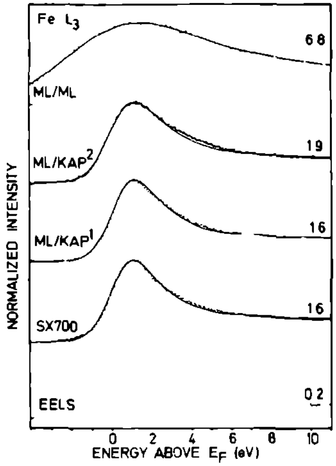

Fig. 8. The dotted curves are from the bottom to the top: the original Fe EELS spectrum with 0.2 eV (FWHM) resolution, the Fe XAS spectrum recorded with the SX700 grating monochromator, the Fe XAS spectra recorded with the Daresbury SOXAFS monochromator (ML/KAP^1) and the KMC double crystal monochromator (ML/KAP) equipped with a ML/KAP combination and a Fe XAS spectrum recorded with the SOXAFS monochromator equiped with a ML/ML combination. The solid lines through the spectra are the Gaussian broadened Fe EELS curves. The numbers on the right give the total Gaussian broadenings (FWHM) of these curves in eV.

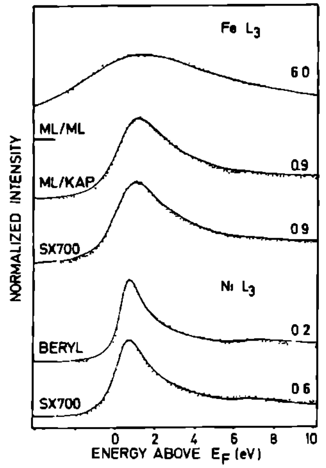

Fig. 9. Fe XAS spectra (upper three dotted curves) recorded with the SX700 monochromator and the Daresbury SOXAFS monochromator equipped with a ML/KAP and a ML/ML combination. Ni XAS spectra (lower two dotted curves) recorded with the SX700 monochromator and the Daresbury SOXAFS monochromator equipped with two beryl crystals. The solid lines are the corresponding Lorentzian broadened EELS curves. The numbers on the right give the Lorentzian broadenings (FWHM) of these curves (in eV) added to the original Gaussian instrumental FWHM of the standard EELS spectra.

Because of the good results for Lorentzian broadening for the XAS data of V, we tried also Lorentzian broadening on the Fe EELS spectra, but it clearly resulted in a poorer match, as shown in fig. 9 for some data on Fe and Ni.

The XAS data for Ni recorded with the SX700 and double beryl monochromators are shown in fig. 10. Again the match between the Gaussian broadened EELS curves and the XAS data is very good and again the match with Lorentzian broadened EELS curves (fig. 9) is less perfect.

5. Discussion

As illustrated in figs. 7–10, a given measured spectrum can often be simulated rather well using standard data and either Gaussian or Lorentzian approximations to the soft X ray monochromator instrument function. As seen in table 1, the assumption of Lorentzian broadening gives much more attractive figures for the resolution than Gaussian broadening, particularly at good resolution. For this reason alone we think that Lorentzian figures are likely to be more widely quoted.

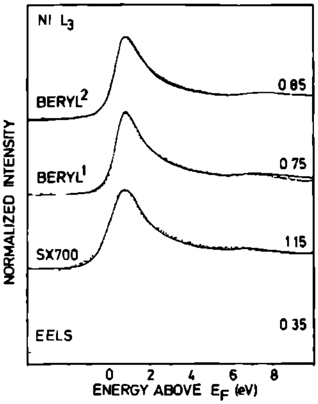

Fig. 10. Ni EELS spectrum (bottom curve) with 0.35 eV resolution (FWHM) and the Ni XAS spectra (dotted curves) recorded with the SX700 grating monochromator, the SOXAFS monochromator (Beryl^1) and the KMC double crystal monochromator (Beryl) equipped with beryl crystals. The solid lines through the XAS spectra are the Gaussian broadened Ni EELS spectra. The numbers on the right in the drawing are the total Gaussian broadenings (FWHM) of these spectra in eV.

Whilst some theoretical arguments can be made in favour of Gaussian instrument functions, in practice there is probably no good reason to assume either pure Gaussian or pure Lorentzian forms and an infinite number of shapes are feasible. The results reported here show that it is not usually possible to determine unambiguously the instrument function of a soft X ray monochromator by comparing measured XAS spectra with broadened standard data. We do not believe that methods based on deconvolution would be superior.

We note that whilst our studies did not yield detailed instrument functions, figs. 1–6 were a basis for a reliable and reproducible scale of resolution for several different monochromators. We regard this as very useful in view of the numerous inconsistencies in quoted instrumental resolutions revealed by even a short study of the XAS and synchrotron PS literature. We were able to show that the instrument function of a high energy grating monochromator in standard (not optimal) operation not only increases in width at higher energies, but that it also changes shape from run to run. This is the reason why the SX700 resolution given for 710 eV appears anomalously bad (see table 1). At ~ 500 eV the Gaussian function had insufficient weight in the tail to provide an ideal simulation.

It is interesting that the XAS spectra obtained with artificial multilayers as the dispersive elements in the monochromator are so well fitted with Gaussian broadering There are arguments that the contribution of the crystal rocking curve should give a Gaussian contribution to the instrument function Clearly if this contribution is very large, then possible non-Gaussian contributions from aberrations in the optical system can be neglected

Acknowledgements

We are grateful to the staff of the BESSY and Daresbury synchrotron institutes and in particular to Dr F Schaefers and Dr A A MacDowell, for their aid with the measurements We acknowledge the valuable work by Dr G van der Laan in the early stage of this project We also wish to thank Dr J Fink for permitting us to use his results This work was supported, in part, by the Dutch Foundation for Chemical Research (Stichting Scheikundig Onderzoek Nederland, SON) with financial assistance of the Netherlands Organization for Scientific Research (Nederlands Organisatie voor Wetenschappelijk Onderzoek, NWO) and of the Comittee for the European Development of Science and Technology (CODEST) program

References

[1] G van der Laan, J B Goedkoop, J C Fuggle, M P Bruijn, J Verhoeven, M J van der Wiel, A A MacDowell, J B West and I H Munro, Nucl Instr and Meth A255 (1987) 592

[2] Z Hussain, E Umbach, D A Shirley, J Stohr and J Feldhaus, Nucl Instr and Meth 195 (1982) 115

[3] H Maezawa, S Nakai, S Mitani, H Noda, T Namioka and T Sasaki, Nucl Instr and Meth A246 (1986) 310

[4] G van der Laan, J B Goedkoop and A A MacDowell, J Phys E20 (1987) 1496

[5] F J Himpsel, Y Junget, D E Eastman, J J Donelon, D Grimm, G Landgren, A Marx, J F Morar, C Oden, R A Pollak and J Schneir, Nucl Instr and Meth 222 (1984) 107

[6] A A MacDowell, J B West, G N Graves and G van der Laan, Rev Sci Instr 59 (1988) 843

[7] J Feldhaus, F Schäfers and W Peatman, Proc SPIE 733 (1987) p 24

[8] J Fink, private communication

[9] J Fink, Th Muller-Heinzerling, J Pfluger, A vom Felde and B Scheerer, Proc Int Conf on X-ray and Inner-Shell Processes in Atoms, Molecules and Solids, eds A Meisel and J Finster (Karl-Marx-Universitat, Leipzig, GDR, 1884), p 425

[10] R D Leapman, L A Grunes and P L Fejes, Phys Rev B26 (1982) 614

[11] M Inokuti, Rev Mod Phys 43 (1971) 297

[12] H H Voigt, Abriss der Astronomie I, Bibliographisches Institute AG (Manheim, 1969)

[13] J Fink, Th Muller-Heinzerling, B Scheerer, W Speier, F U Hillebrecht, J C Fuggle, J Zaanen and G A Sawatsky, Phys Rev B32 (1985) 4899

[14] H Petersen and H Baumgartel, Nucl Instr and Meth 172 (1980) 191

[15] H Petersen, Opt Commun 40 (1982) 402

[16] H Petersen, Nucl Instr and Meth A246 (1986) 260

[17] K Becker and K Beckstette, Proc Int Conf for Ultra High Precission Technology, Aachen, May 1988 (Springer, 1988) p 212

[18] G van der Laan, M P Bruijn J B Goedkoop and A A MacDowell, Proc SPIE 733 (1987) p 38

Chapter 6

X-RAY DICHROISM OF Tb IRON GARNET

6.1 Introduction

In this chapter we present x-ray absorption spectra of terbium iron garnet (TBIG), which form the first experimental verification of the magnetic dichroism described in Chapter 3.

Rare earth iron garnets (RIG), with structural formula $R_3Fe_5O_{12}$, form one subfamily of the huge class of metal oxides with the garnet stucture. Because of their interesting magnetic, magneto-elastic and magneto-optical properties, RIG have been the subject of continued study since the end of the fifties, when it was realized that the rare earth 'ferrites' studied by Néel[127] in fact had the garnet structure[128]. Interest peaked in the seventies when expectations were held high for the use of RIG films with perpendicular anisotropy as magneto-optical storage media[129] in so-called magnetic bubble domain memories but since then they have been dropped in favour of amorphous R-Fe alloy films[45]. Currently iron garnets are still heavily investigated because of their complicated magnetic behaviour, which shows anisotropic exchange[130] and magnetic phase transitions[131, 132].

Because of their high Néel temperatures(~545-560 K)[133, 134] and their uniaxial anisotropy, RIG were selected as testmaterials for the experimental verification of the magnetic x-ray dichroism according to the predictions by Thole *et al.* [28]. On the following pages we reprint a brief report[135] on experiments on TbIG that formed the first proof of the existence of the MXD effect. It is followed by an addendum wherein improved data are shown and wherein the discussion that is given in the article is extended.

ion	approximate O-coordination	spacegroup position	pointgroup
R	dodecahedron	24(c)	D_2—222
Fe	octahedron	16(a)	C_{3i}—$\bar{3}$
Fe′	tetrahedron	24(d)	S_4—$\bar{4}$

Table 6.1: Structural data of iron garnets

Some structural and magnetic details of garnets

The crystal structure of garnets has cubic symmetry (space group Q_h^{10} $Ia3d$). In the ferrimagnetic iron garnets the onset of magnetic order at the Curie temperature induces a rhombohedrally distortion of the unit cell[136]. The $Ia3d$ space group contains two Fe sublattices, and more properly, the formula unit of garnets is written as $R_3Fe_2Fe'_3O_{12}$, where R designates a rare earth and the prime serves to distinguish two different Fe sublattices. Each metal ion in the structure is completely surrounded by O atoms, with coordination, spacegroup positions and site pointgroups as given in Table 6.1. More detail can be found in the cited references.

Below the Curie temperature the two Fe sublattices order ferrimagnetically along the [111] axis. Since the ratio of 16(a) sites to 24(d) sites is 2:3, the net magnetic moment corresponds to one Fe moment (5 μ_{Bohr}) per formula unit. The rare earth ions are coupled antiferromagnetically with the 24(d) sites, a coupling constant one order of magnitude smaller than the coupling coupling between the Fe (c) and (a) sites. The other coupling energies are small enough to be neglected. The contribution of the rare earth ions to the magnetic moment increases only slowly with decreasing temperature. Since the saturation moments of the rare earth ions are nearly all larger than 5 μ_{Bohr}/atom, the magnetic moment vanishes at the compensation point were the R moment and the Fe moment cancel. Below this temperature the R moment dominates the magnetic moment (see *e. g.* Kittel[13]).

PHYSICAL REVIEW B VOLUME 34, NUMBER 9 1 NOVEMBER 1986

Experimental proof of magnetic x-ray dichroism

Gerrit van der Laan, Bernard T Thole, and George A Sawatzky
Physical Chemistry Department of the Material Science Center, University of Groningen
NL-9747 AG Groningen The Netherlands

Jeroen B Goedkoop and John C Fuggle
Research Institute for Materials, University of Nijmegen Toernooiveld 10
NL-6525 ED Nijmegen The Netherlands

Jean-Marc Esteva and Ramesh Karnatak
Laboratoire pour l Utilisation du Rayonnement Electromagnétique,
F-91405 Orsay Cédex, France

J P Remeika
AT&T Bell Laboratories, Murray Hill, New Jersey 07974

Hanna A Dabkowska
Instytut Fizyki Polskiej Akademii Nauk Aleja Lotnikov 32/46 Warzawa, Poland
(Received 24 April 1986)

What we believe to be the first experimental results have been obtained on strong magnetic x-ray dichroism in the M_{45} absorption spectra of magnetically ordered rare-earth materials, in accordance with recent predictions

The feasibility of using x-rays to determine the magnetic structure of magnetically ordered materials by magnetic dichroism has recently been predicted theoretically[1] Strong magnetic x-ray dichroism (MXD) is expected in the M_{45} absorption edge structure of rare-earth-metal compounds Polarized synchrotron radiation can therefore be used to reveal information on the local rare-earth-metal magnetic moments in solids, thin films, and surfaces In this Brief Report we will give what we believe is the first experimental proof of this effect

The M_{45} absorption in rare-earth-metal compounds shows good agreement with the atomic Hartree-Fock calculations for the transitions from the $4f^n(J)$ Hund s rule ground state to the manifold of $3d^9 4f^{n+1}(J')$ final states[2-4] Although in x-ray absorption spectroscopy (XAS) hundreds of excited levels may be involved, one can distinguish between three different types of excitations, namely for $J - J = -1$, 0, and 1

In the presence of a magnetic field the $2J+1$ degenerate ground state $4f^n(J)$ splits into sublevels $M_J = -J$, $,+J$ The relative population of these sublevels depends on the temperature That the polarization vector of the x rays has a drastic effect on the spectrum can be seen from the simple case where only $M = -J$ is populated ($T = 0$ K) With the polarization direction parallel to the magnetization only the $\Delta M = 0$ transitions are allowed The transitions $J' - J = -1$ will then vanish, because the $M' = -J$ sublevel is not present in the $J' = J - 1$ state

Here, we will illustrate in more detail the use of MXD on terbium iron garnet (TbIG), which has a rather complicated magnetic structure The rhombohedral (or trigonal distorted cubic) cell of ferrimagnetic rare-earth-metal iron garnets ($R_3Fe_5O_{12}$) contains eight formula units[5] The Fe^{3+} ions occupy the 24 *d* (tetrahedron) and the 16 *a* (octahedron) positions The larger R^{3+} ions occupy the 6 *c* (dodecahedral) positions Below the Néel temperature the spins of the 24 *d* and 16 *a* irons are ordered antiparallel along the [111] axis The rare-earth-metal moments couple antiferromagnetically to the net iron moment[6] By symmetry the 6 *c* sites can be divided into c_1, c_2, c_3 and c_1, c_2, c_3', where c_2 (c_2') and c_3 (c_3') are obtained from the c_1 (c_1') by rotation around the trigonal [111] axis From neutron diffraction at 4 2 K the Tb moments in TbIG are known to form a double umbrella structure[7 8] The magnetic moments on c_1 and c_1' are both in the $(0\bar{1}1)$ plane, having angles $\beta = 30\ 79°$ and $\beta' = -28\ 07°$ with the trigonal axis, and absolute values $m = 8\ 18\mu_B$ and $m' = 8\ 90\mu_B$, respectively Above 4 2 K the values of β, β', m and m' are expected to decrease[7]

In our experiment, a single crystal of TbIG was mounted on a rotatable helium-flow cryostat in an ultrahigh vacuum of $\sim 10^{-10}$ Torr The temperature at the surface of the sample was 55 ± 5 K A Co_5Sm permanent magnet provided a field of ~2 kG parallel to the [111] surface normal, which is the easy direction of magnetization

Synchrotron radiation from the 540-MeV storage ring ACO (Anneau de Collision d'Orsay) at the Laboratoire pour l'Utilisation du Rayonnement Electromagnétique was monochromatized with a constant-deviation double-crystal monochromator Using beryl $(10\bar{1}0)$ crystals (morganite) the energy resolution at the Tb M_5 edge is 0 9 eV full width at half maximum[3] In the spectral region of interest the x-ray flux is invariant with photon energy The emitted radiation in the equatorial plane of the storage ring is linearly polarized In the actual setup it is *s* polarized with respect to the beryl crystals and *p* polarized with respect to the sample

XAS spectra were measured using the electron yield method,[3] and were obtained at different angles (α) between the polarization vector of the incident radiation and the [111] magnetization direction

The experimental M_5 spectra for various values of α are given in Fig 1 The solid lines are theoretical curves, as discussed below As seen, the intensities of the two major peaks are strongly polarization dependent Parallel polarization with respect to the net magnetization enhances the left-hand peak, whereas for perpendicular polarization the right-hand peak increases in intensity

Neglecting crystal field effects, the theoretical curves in Fig 1 can be calculated with the theory given in Ref. 1. The Boltzmann-averaged sum of the absorption intensities for transitions between the magnetic sublevels αJM in the ground state (α labels different levels of equal J) and the excited levels $\alpha' J' M'$ is given by the line strength times a factor

$$\langle A^{\theta}_{JJ'}\rangle = \langle A^{\parallel}_{JJ'}\rangle \cos^2\theta + \langle A^{\perp}_{JJ'}\rangle \sin^2\theta \ , \qquad (1)$$

where θ is the angle between the magnetic moment and the electrical polarization vector of the incident radiation

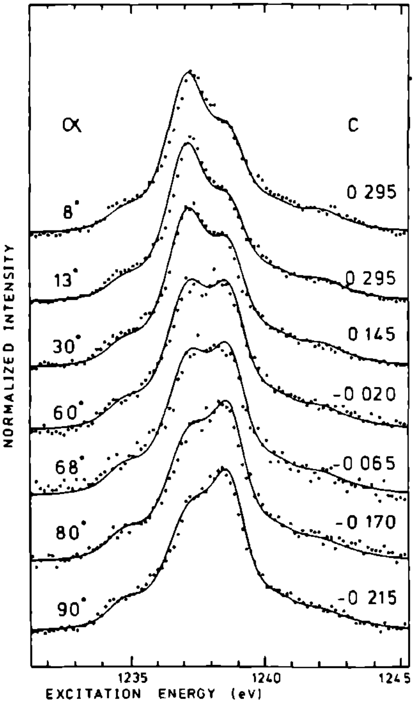

FIG 1 Experimental M_5 absorption spectra of TbIG at various values of α, which is the angle between the polarization vector of the x rays and the [111] magnetization direction The solid lines are fits using Eq (5) The optimum values of C are indicated

The temperature-dependent factors for parallel and perpendicular polarization $\langle A^{\parallel}\rangle$ and $\langle A^{\perp}\rangle$ are related as

$$\langle A^{\perp}_{JJ'}\rangle = \tfrac{1}{2}[1/(2J+1) - \langle A^{\parallel}_{JJ'}\rangle] \qquad (2)$$

There are only three different factors $\langle A^{\parallel}_{JJ'}\rangle$, viz $J'-J=-1,0,+1$ They are given as a function of the temperature-dependent quantity $\langle M^2\rangle$ in Eq (6) of Ref 1

If the magnetic moments are not collinear the angular average of Eq (1) has to be taken For a single umbrella structure we obtain

$$\langle \cos^2\theta\rangle = \tfrac{1}{3} + \tfrac{2}{3}(\tfrac{3}{2}\cos^2\alpha - \tfrac{1}{2})(\tfrac{3}{2}\cos^2\beta - \tfrac{1}{2}) \ , \qquad (3)$$

where α is the angle between the [111] magnetization direction and the polarization vector, and β is the angle between the [111] direction and the magnetic moment For the double umbrella the average of $\cos^2\beta$ has to be taken Combination of Eq (6) of Ref 1 with Eqs (1), (2), and (3) of this work yields

$$\langle A^{\theta}_{J+1}\rangle = \frac{1}{3(2J+1)}\left[1 - \frac{J(2J-1)}{(J+1)(2J+3)}C\right] \ ,$$

$$\langle A^{\theta}_{J}\rangle = \frac{1}{3(2J+1)}\left[1 - \frac{2J-1}{J+1}C\right] \ , \qquad (4)$$

$$\langle A^{\theta}_{J-1}\rangle = \frac{1}{3(2J+1)}(1-C) \ ,$$

where

$$C = (\tfrac{3}{2}\cos^2\alpha - \tfrac{1}{2})(\tfrac{3}{2}\cos^2\beta - \tfrac{1}{2}) \times \frac{\langle M^2\rangle - \tfrac{1}{3}J(J+1)}{J^2 - \tfrac{1}{3}J(J+1)} \equiv C_\alpha C_\beta C_M \qquad (5)$$

Note that the factors $\langle A\rangle$ have axial symmetry around the [111] axis

In order to observe an anisotropic absorption ($C\neq 0$), three conditions must be met α and β have to be different from the magic angle (54 7°), and $\langle M^2\rangle$ must be unequal to its isotropic value $\tfrac{1}{3}J(J+1)$ This value is reached when all sublevels are equally populated The largest anisotropy is expected if β is zero and $\Theta = kT/g|\mu_B|H$ is small

Line strengths and energies were calculated with an atomic Hartree-Fock program [9,10] The theoretical spectra for values of C which gave the best fit to the experimental data are displayed in Fig. 1 As seen, there is a good agreement between theory and experiment for all the structures present in the spectrum

The optimized values of C are shown in Fig 2 The solid lines give C as a function of α for various constant values of $C_\beta C_M$ The least-squares value for $C_\beta C_M$ is equal to 0 312, with an error of ~0 05 We can verify this value of $C_\beta C_M$ by results from magnetization measurements At $T=55\pm 5$ K the Tb contribution to the magnetization in TbIG is equal to $m=(18\,0\mp 0\,8)\mu_B$ per formula unit[6] Using $m=3(\cos\beta)g\langle M\rangle\mu_B$ and Eq (5) in Ref 1 this gives $C_\beta C_M = 0\,30 \mp 0\,03$ for $\beta=30$, or $C_\beta C_M = 0\,34\mp 0\,03$ for $\beta = 0°$ We obtain a reasonable value for $C_\beta C_M$, which shows that the magnetic dichroism

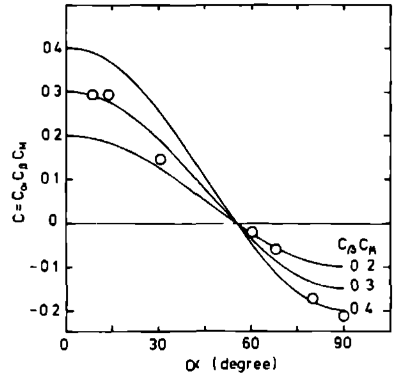

FIG 2 The optimum values of C, obtained by fitting the experimental spectra (o) C as a function of α for various constant values of $C_\beta C_M$ is given by the solid lines

effect is in agreement with other magnetic measurements It is also seen that, with the given error bars in the numbers, the experiment cannot accurately predict the value of β However, the large scatter in the values for $C_\beta C_M$ can be reduced by improving the statistics in the experimental spectra and by regulating the temperature more precisely

In order to obtain more detailed information about the magnetic structure it is also important to measure at a lower temperature For $\Theta = kT/g\,|\mu_B|\,H \lesssim 0\ 3$, only the lowest magnetic sublevel is filled, then C_M goes to one, and the temperature dependence disappears We are planning improvements on our experimental setup in order to achieve this

In summary, we conclude that the M_5 absorption spectrum of TbIG in the presence of a magnetic field shows strong polarization-dependent effects These effects are in accord with the magnetic structure, multiplet calculations, and the predictions of Ref 1

MXD is complementary to other techniques, such as neutron diffraction and Mossbauer, because it can be applied to magnetically ordered thin films and surfaces, and because it is applicable for all magnetic rare-earth-metal compounds and probably can be extended to transition-metal compounds Because MXD yields information on $\langle M^2\rangle$ this technique can also be used for antiferromagnets where $\langle M\rangle = 0$

This investigation was supported by The Netherlands Foundation for Chemical Research (Stichting Scheikundig Onderzoek Nederland) with financial aid from the Netherlands Organization for the Advancement of Pure Research (Nederlandse Organisatie voor Zuiver-Wetenschappelijk Onderzoek), and by the Centre Nationale de la Recherche Scientifique (CNRS), France

---

[1] B T Thole, G van der Laan, and G A Sawatzky, Phys Rev Lett **55**, 2086 (1985)

[2] J Sugar, Phys Rev B **5**, 1785 (1972), Phys Rev A **6**, 1764 (1972), V F Demekhin, Fiz Tverd Tela (Leningrad) **16**, 1020 (1974) [Sov Phys Solid State **16**, 659 (1974)]

[3] B T Thole, G van der Laan, J C Fuggle, G A Sawatzky, R C Karnatak, and J-M Esteva, Phys Rev B **32**, 5107 (1985)

[4] J Sugar, W D Brewer, G Kalkowski, G Kaindl, and E Paparazzo, Phys Rev A **32**, 2242 (1985)

[5] *Physics of Magnetic Garnets* edited by A Paoletti (North-Holland, Amsterdam, 1978)

[6] S Geller, J P Remeika, R C Sherwood, H J Williams, and G P Espinosa, Phys Rev **137**, A1034 (1965)

[7] M Lahoubi, M Guillot, A Marchaud, F Tcheou, and E Roudault, IEEE Trans Magn **MAG-20**, 1518 (1984)

[8] F Sayetat, J X Boucherle, and F Tcheou, J Magn Magn Mater **46** 219 (1984)

[9] R D Cowan, *The Theory of Atomic Structure and Spectra* (University of California Press, Berkeley, 1981)

[10] Slater integrals used were $F_f^2 = 12\ 47$, $F_f^4 = 7\ 84$, $F_f^6 = 5\ 64$, $F_{fd}^2 = 10\ 06$, $F_{fd}^4 = 4\ 71$, $G_{fd}^1 = 5\ 79$, $G_{fd}^3 = 3\ 40$, and $G_{fd}^5 = 3\ 35$ eV

6.3 Addendum

Although the statistics of the data shown in the preceding publication[135] (hereafter referenced as PRB) is poor, they convincingly show the existence of the MXD effect. The bad statistics was caused by the experimental configuration: in order to bring the sample in a single magnetic domain state, it was located in front of one of the poles of a permanent magnet. The yield electrons emitted by the sample follow the magnetic field lines that surround the magnet, and impinge finally on the other pole of the magnet.

In the measurements for PRB, the detector was intercepting only a small part of the magnetic flux lines. Since the appearance of this publication we have remeasured the spectra, this time with a detector that could be moved into the magnetic flux from the sample. In this Addendum we present these new data. Also we elaborate the interpretation of the data given in PRB.

6.3.1 Experimental details

A flux grown single crystal of TbIG of ~8 mm^3 was cut and polished to expose a (111) oriented back plane. This plane was used to mount mount the sample in the way described in PRB. The front surface of the sample was formed by the (110) and (211) facets that were formed during growth. From XPS measurements performed on an YIG crystal it was found that these as-grown surfaces are nearly clean after baking the UHV system, while a very light argon ion sputtering was found to removes the < 1 monolayer of carbon remaining on the surface after the bake.

Temperatures could be measured with a K-type thermocouple fixed on the sample holder next to the sample. From the lag between the stabilization times of the sample holder temperature and the MXD effects it was found that thermal conductance between the sampleholder and the samples front surface was poor, limiting the accuracy of the temperature temperature could be stabilized to ± 5 K.

6.3.2 Results and Discussion

In Fig. 6.1 we present the new experimental data. The spectra were obtained at temperatures of 55 ± 7 K and, as before, at various angles between the magnetization and the polarization directions. We will concentrate here on

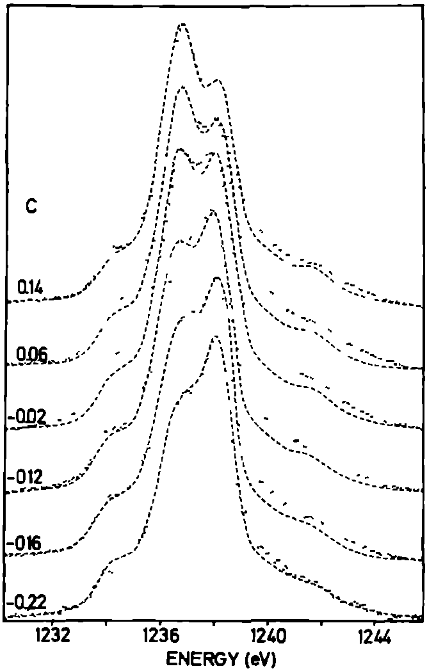

Figure 6.1: Tb M_5 XAS spectra of Tb iron garnet. The dashed lines are fits to the experimental spectra using the C-values listed on the left.

the quality of the fit of the theoretical curves to the experimental data, from which one seeks to obtain the linear dichroism parameter C.

The solid lines in Fig. 6.1 are the the best eye-fits of theoretical curves to the experimental data based on the atomic model calculations described in PRB and Section 3.5. The C-values pertinent to the theoretical curves are given on the left of the figure. The Slater integrals used to obtain these curves are the same as given in ref. 10 of PRB; they correspond to reductions of 80%, 100% and 80% for $F_f^{2,4,6}$, $F_{fd}^{2,4}$ and $G_{fd}^{1,3,5}$ respectively. It should be noted that these values give a substantially narrower line than the values used in Fig. 3.2.

For spectroscopic standards, the correspondence of experimental and theoretical curves is very good. Close inspection shows however that the theoretical curves are too broad by a few 100 meV. Reducing the Gaussian (resolution) or Lorentzian (lifetime) broadening does improve this, but leads to a too deep valley in between the main peaks and a too pronounced left shoulder. We attempted to obtain better correspondence by varying systematically the the reduction factors of the Slater integrals. Doing so moves around the three ΔJ contributions with respect to each other. As a second order effect, also their shape is affected. We did not find substantially better results, while deviations of a few percent from the listed values severly detoriorate the match. Apparently we have reached the limitations of the multiplet program used for the calculations. Although the precise cause is not clear yet, we suspect the problem lies in the neglect of configuration interaction and the separation of the wavefunction in a radial and an angular part.

We end this discussion of the fits with a rather subtle point related to the reliability of the obtained dichroism parameter values. In Fig. 6.2 we present the $T = 0$ K spectra for perpendicular-, parallel-, and un-polarized x-rays for the set of Slater parameters used here. It can be seen that in the two polarized cases one peak dominates the spectra, while the complementary component (the lesser peak) is visible at best as a weak shoulder. However since, as mentioned above, the separation between the two peaks in the unpolarized spectrum is too large, when $|C|$ is increased from the unpolarized value, the lesser peak remains remains visible longer. Since when fitting by eye one uses by necessity mainly the ratio of the main peak to the lesser peak, one will underestimate the true C-value. This point is returned to in Chapter 8, when the measured angular dependence of C of thin Tb films on a Ni(110) crystal is discussed.

6.3.3 Conclusion

Although the correspondence between data and theoretical curves is excellent, the agreement between the data and the atomic model is somewhat fortuitious. Since the appearance of the article reprinted on the previous pages, we have realized that the assumption that crystal fields can be neglected, such as is made a few lines above equation PRB(1), is certainly not warranted for the rare earth ions in garnets[137, 138, 139]

Due to the low symmetry D_2 of the rare earth sites[129, 140], the exchange field and the crystal field terms in the Hamiltonian are of the same order of magnitude. Furthermore, due to the low symmetry of the rare earth sites, both the crystal field potential and the anisotropic exchange tensor contain

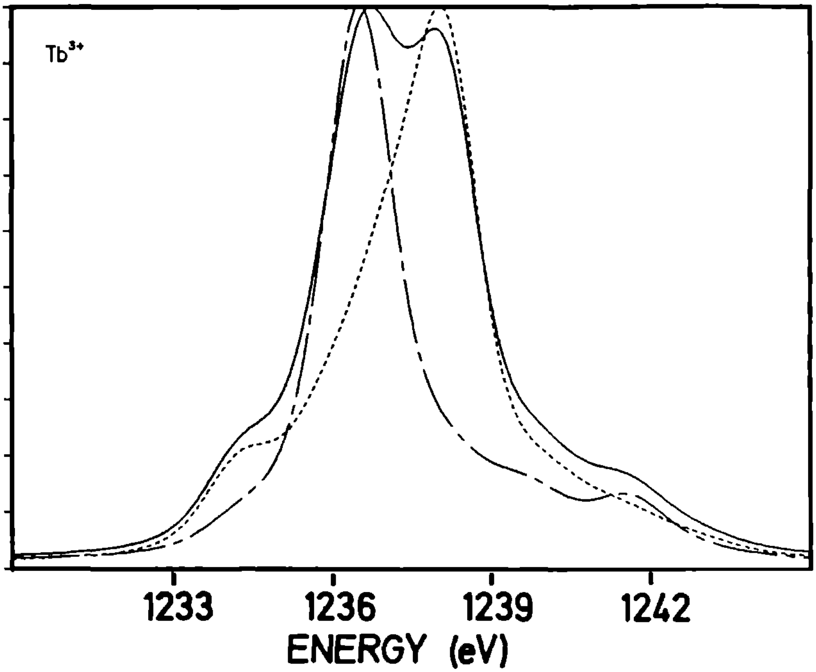

Figure 6.2: Calculated Tb M_5 spectra for unpolarized (full curve), perpendicular (dashed) and parallel (dotted) polarized x-ray. Note these curves are considerably narrower than those in Chapter 3, due to the different values used for the Slater integrals.

at least nine non-vanishing terms[139]. This has forbidden detailed analysis of the energy level schemes except in a few particularly simple cases like Eu, Gd and Yb iron garnets, for which total splittings of ~500 cm^{-1} (700 K) have been found from infra-red absorption experiments. The situation sketched above shows that in this case it is impossible to state wether the splittings responsible for the dichroism effect in the present data is produced by magnetic or by crystal field splittings.

However, it is undoubtedly because of the *magnetic* ordering that the effect is seen in a crystal that has *cubic symmetry* above the Curie temperature[129]. A combination of linear and circular dichroism techniques, combined with lower temperature measurements would be a strong tool to separate magnetic and crystal field effects.

Chapter 7

AN XAS STUDY OF Tb—Ni INTERMETALLIC COMPOUNDS AND THE Tb/Ni(110) OVERLAYER SYSTEM

7.1 Introduction

In this chapter we present results of a systematic study of the Ni L_3 and Tb M_5 edges of Tb—Ni intermetallic compounds and Tb/Ni overlayers. This study was performed to give a background for the interpretation of the MXD measurements described in the Chapter 8 of this thesis. Also, it forms a part in a broader study of the electronic and magnetic structure of RE—TM compounds currently performed by our group. The band structure effects present in the data will be integrated with XPS/BIS measurements and spin-resolved bandstructure calculations[111] in a later stage.

The rare earth-transition metal (RE —TM) intermetallic compounds are interesting both from a technological and from a scientific point of view. First of all, the important progress made in the development of hard magnetic materials (*e. g.* Co_5Sm, $Nd_2Fe_{15}B$) concerns these materials[142]. Also, the combination of out-of-plane magnetic anisotropy, high remanence and large Kerr rotation found in co-evaporated TbFe(Co) amorphous films is likely to find widespread application in magnetic storage technology[46]. Scientifically, these materials are of interest because of the anomalies in the magnetic behaviour, which are still not understood. For instance, in the Ni - RE series the Ni moment vanishes in the 1:5 compound, reappears in the 2:7 and 1:3 compounds and disappears again for still higher RE concentrations[113, 111].

For a proper understanding of electron yield measurements it is essential to know the probing depth profile. Information on the probing depth can be obtained from experiments on overlayer systems by measuring the overlayer thickness dependence of the edge-jumps, *i. e.* the step in the absorption coefficient at the absorption edge, of both the substrate material and the overlayer.

Recently Erbil *et al.* gave a detailed analysis of the probing depth of total electron yield for K edge EXAFS at photon energies above 5 keV[124]. These authors used a simple two-step model for the yield produced at the surface per absorbed photon. In the first step the numbers and energies of the primary Auger electrons produced by the *decay cascade* in the core ionized atom are determined, using the known relative probabilities of Auger decay versus fluorescence decay[16, 125]. The second step consists of modelling the number of yield electrons produced at the surface by each primary Auger electron in the *collision cascade* wherein it loses its energy.

As was shown by Erbil *et al.* (see Figures 7.1[124] and 7.2[144]) their analytical expressions for the yield-current as a function of thickness predict satisfactorily the scarce available data on overlayer systems. The authors conclude that the probing depth of the yield method is determined by the range of the most energetic primary (KLL) Auger electron, while lower energy (LMM) Augers can lead to an enhanced surface sensitivity (*e. g.* the peak in the Ge signal of Fig. 7.1.

In the soft x-ray range up to know only few results on poorly characterized samples are known[145]. In part, this is due to the problems arising from the shorter penetration depth of soft x-rays, necessitating the use of thinner layers and hence better vacuum conditions. However, knowledge of the probing depth is necessary for the interpretation of electron yield spectra. For instance, as was suggested by Thole *et al.* [29], in some cases the maximum absorption in the white lines of concentrated systems may lead to an x-ray attenuation length that might be comparable to the range of the Auger electrons, which would lead to a saturation of the strongest peaks in white line spectra. An indication of the occurence of such effects was obtained by van der Laan and Thole[146] from the angular dependence of the La M_5 line. The purpose of the overlayer experiment was to obtain information on this problem.

7.2 Experimental

X-ray absorption spectra were taken at the newly constructed windowless UHV double crystal beamline SA21 at the Super-ACO storage ring at LURE.

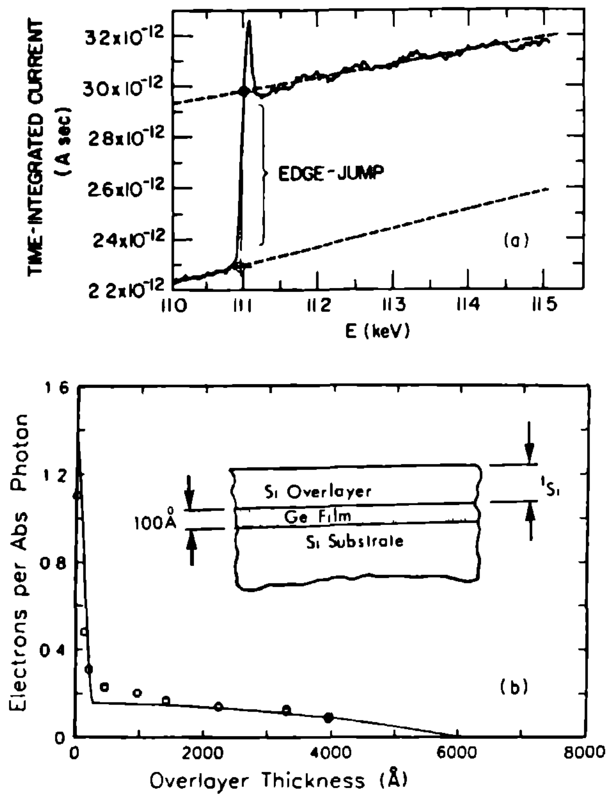

Figure 7.1: (a) Definition of the edge jump for the Ge K edge. (b) Si-coverage dependence of the Ge K edge-jump of the system Si/Ge(100Å)/Si. From Erbil *et al.* [124]

The monochromatizing crystal were two natural beryl crystals. Low energy radiation from the ring was rejected with a self-supporting C foil of 1 μm thickness placed in front of the monochromator. Because of the high flux it was always possible to reduce the beam dimension to less than 1 mm^2. The resolution is estimated to be 400 meV at the Ni L_3 edge[147, 148] (851.9 eV) and 450 meV at the Tb M_5 edge (1238.4 eV)[29].

The polycrystalline Tb—Ni alloys were prepared by fusing stoichiometric proportions of high purity base material in an arc furnace, followed by annealing for different periods of time under an inert atmosphere. The phase of the samples was checked by standard x-ray diffraction. The 3:1 compounds were found to be sensitive to air and were kept under vacuum prior to measurement. Immediately prior to measurement the samples were scraped with an Al_2O_3 file to remove surface contaminants. During measurement the pressure was better than 5x10^{-10} Torr; total acquisition time was $\leq$ 30 min. The spectra were recorded at normal incidence in the total electron yield mode, with the detector at 45 from the light direction.

The single crystal Ni sample was cleaned in vacuum by the usual cycles of sputtering and annealing. Good 1x1 LEED surfaces were obtained. C contamination was less than 10% as judged from Auger spectra, and no other contaminants were observed. Tb overlayers were deposited from a Knudsen cell furnace. The temperature of the substrate during deposition was ~300 K as measured with a K-type thermocouple spotwelded on the back of the sample. Layer thicknesses were determined with an oscillating quartz monitor with an estimated systematical error of 40%. During annealing and evaporation the base pressure of 2x10 ^{10} Torr rose to 10x10^{-10} Torr. The overlayers were found to contain ~10% C contamination.

All total yield spectra were obtained at normal incidence. The detector consisted of an unbiased channeltron (Philips X919BL) with an opening cone diameter of 10 mm. Except for the cone aperture, the channeltron was covered by a grounded stainless steel hood. All overlayer spectra were collected during a single run under constant operating conditions of the channeltron. Maximum counting rates were always kept below 80 kHz to avoid saturating the channeltron, which is important for analysis of these very sharp 'white line' spectra.

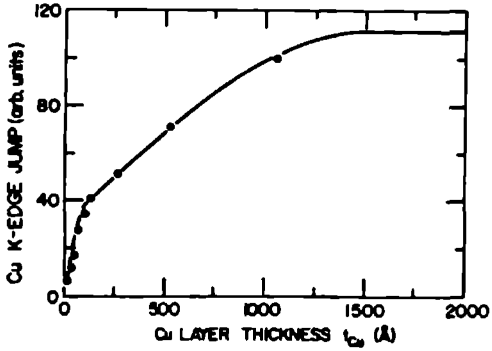

Figure 7.2: Coverage dependence of the signal strength of the Cu K egde of the system Cu/Ni. From Martens *et al.* [144]

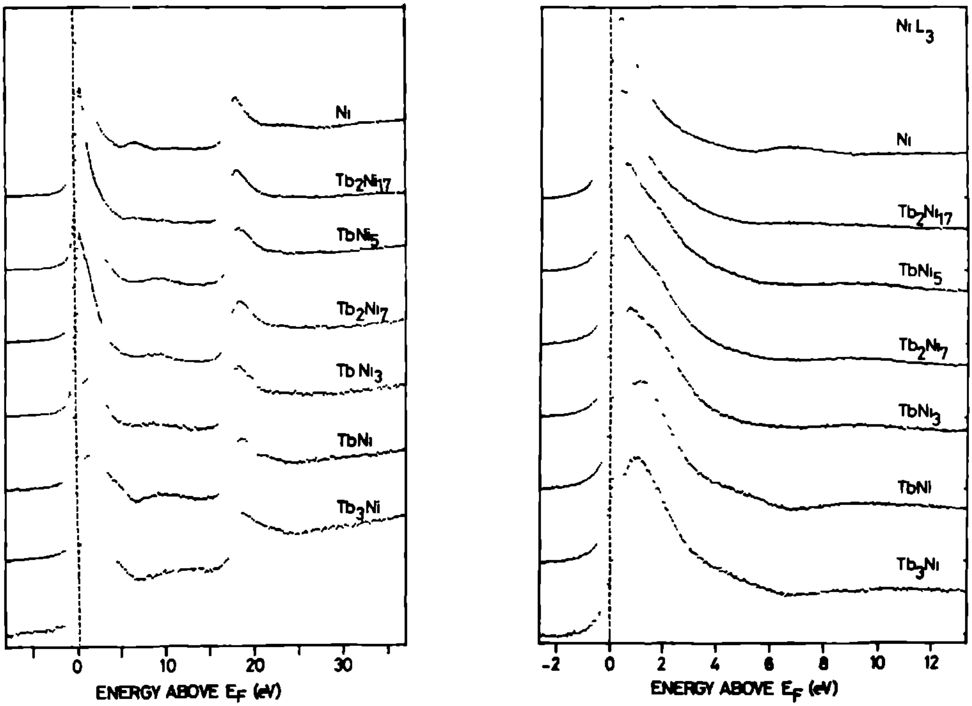

Figure 7.3: Peak-normalized Ni $L_{2,3}$ edges of Ni and 6 Tb—Ni intermetallic compounds. (a) $L_{2,3}$ edges. (b) L_3 edges in detail.

7.3 Results and Discussion

7.3.1 Bulk compounds

In Fig. 7.3 we show the Ni $L_{2,3}$ edges of Ni metal, Tb_2Ni_{17}, $TbNi_5$, Tb_2Ni_7, $TbNi_3$, TbNi and Tb_3Ni intermetallic compounds. The spectra were peak normalized after division by a linear background, which was obtained from the slope of a 20 eV interval in front of the edge (not shown). The slope of this background is assumed to be representative of the change in throughput of the monochromator.

It is immediateley evident from the spectra that the intensity ratio of the main peak to the plateau following it does not change much over the series. Also the L_2 to L_3 intensity ratio does not appear to change much, compatible with the metallic nature of these compouds [18]. Since the lifetime broadening of the L_2 is much larger than that of the L_3 we focus our attention on the L_3 spectra. In Fig. 7.3.b we show the Ni L_3 edges in more detail. The main feature in all spectra is the peak at 2-4 eV above the edge. On surveying the series, a prominent general trend is the shift of intensity away from the Fermi level, with a change of the main peaks' shape from right-angled triangular to semi-elliptical in the 1:1 and 3:1 systems. Although we will not discuss bandstructure effects in detail here, we draw attention to the near-constancy or even increase in the area of the main peak with respect the plateau. In pure Ni the main peak is thought to consist of unoccupied Ni d states. If we assume this is true also for the compound spectra, then it follows that the number of 3d holes on the Ni site stays roughly constant. This is in contradiction to what has been observed in a large number of other Ni binary alloys studied with XAS[149] and XPS/BIS[150], where invariably the main peak decreased strongly with respect to the plateau upon increasing dilution by the partner element.

The spectra in Fig. 7.3.b are aligned on the Fermi level, which was estimated from comparisons to broadenings of model density of states. The amount by which the spectra were shifted is plotted in Fig. 7.4. It is seen that both the edge and the peak positions increase continuously with increasing Tb concentration to higher photon energies, with the maximum shifts of 0.45 eV for the edge and 1.0 eV for the peak occuring in Tb_3Ni. We ascribe the shift of the edge position to a core level shift due to the changing chemical coordination of the Ni atoms upon increasing dilution with rare earth atoms, as was suggested by Johansson *et al.* [151]. An interpretation involving core excitons can be rejected on the ground that the Ni L_3 edge energy corresponds to closely with the XPS binding energy of the $2p_{3/2}$ level[152]. The extra shift of the peak position, is clearly related to bandstructural changes.

The M_5 spectrum of Tb (not shown) consists of a structured sharp peak reflecting the final state multiplet structure of the atomic-like transition 3d→4f[28]. Due to the atomic nature of the edge it is unaffected by the chemistry of its surroundings. For the present purpose the important information of the Tb M_5 spectra lies in the trend of the background-normalized peak height, or signal strength, as is discussed below.

7.3.2 Concentration dependence of signal strength

The present series of compounds offers a good opportunity to quantify the sensitivity of XAS in total electron yield mode. In Fig. 7.5 we plot the concentration dependence of the signal strength S, defined here as

$$S = \frac{Y_{edge} - Y_{pre-edge}}{Y_{pre-edge}}, \tag{7.1}$$

where Y_{edge} and $Y_{pre-edge}$ are the count-rates in the maximum of the edge and in front of the edge respectively. The practical value of this definition is that a low S (< 0.2) means one has to accumulate very long to obtain sufficient statistics in the background-substracted spectrum. The signal strength used here differs from the edge-jump as used by Erbil *et al.* [124], which is the ratio of the step in the absorption at the edge to the absolute x-ray intensity, measured with an I_0 monitor. However, the results from Martens *et al.* given in Fig. 7.2[144] give the signal strength as defined here.

From the figure the Tb signal is seen to increase linearly with the Tb concentration x, as on first sight one would expect it to, since the shape of the Tb M_5 is known to be unaffected by the electronic structure of the alloy [28, 88]. With the exception of Tb_2Ni_7 (x=22%) the points can be fitted very well by the straight solid line. Unfortunately we lacked a pure Tb sample, but by extrapolation we obtain a value of 19.0 for the signal strength at x=1.

The Ni L_3 results at first sight are somewhat surprising. Again with the exception of Tb_2Ni_7 the Ni signal strength is found to decrease monotonically with Tb concentration. However, these seemingly contradictory curves can be reconciled if one looks closer at expression 7.1. For an edge of component A of

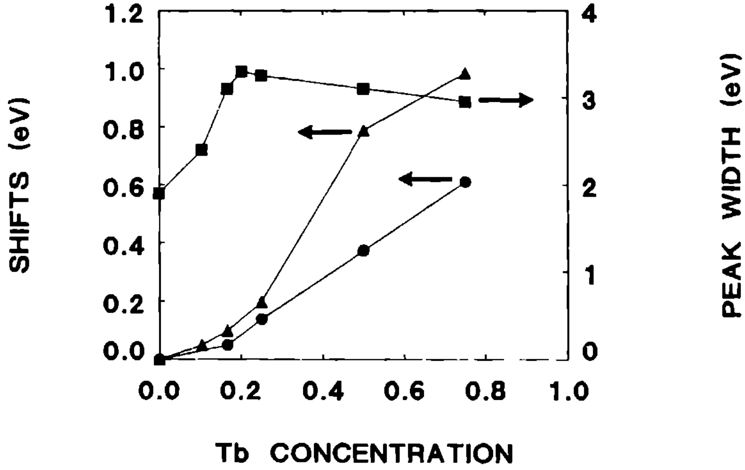

Figure 7.4: Shift of the edge and peak energy position relative to the Ni L_3 edge position, as a function of Tb concentration.

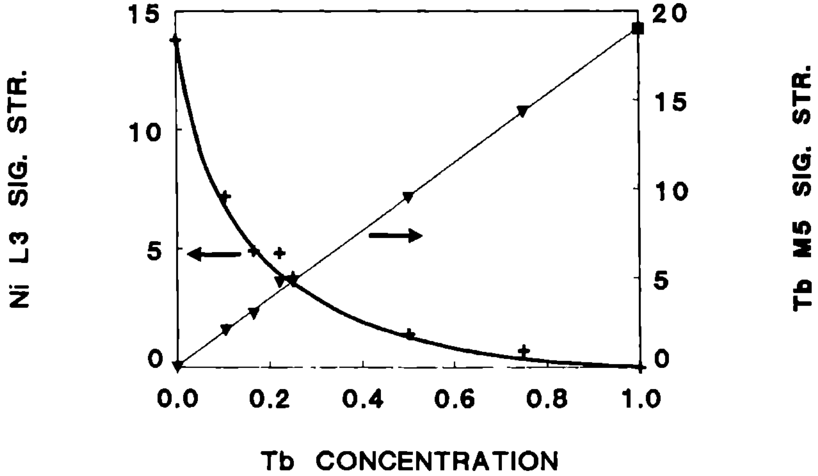

Figure 7.5: Concentration dependence of the signal strength of the Tb M_5 edge and the Ni L_3 edge of the intermetallic compound series Tb_xNi_{1-x}. The solid lines are fits to the data as explained in the text. The value for the Tb M_5 edge for x=1 is obtained by extrapolation of the points at lower concentrations.

a binary system $A_{1-x}B_x$, the pre-edge and edge count-rates are proportional to:

$$\begin{aligned} Y_{edge}(A) &\propto (1-x)(\sigma_e Y_e + \sigma_o Y_o) + x\sigma_B Y_B && (7.2) \\ Y_{pre\ edge}(A) &\propto (1-x)\sigma_o Y_o + x\sigma_B Y_B && (7.3) \end{aligned}$$

where σ_e is the partial absorption cross-section of the core level of the edge of element A, and σ_o and σ_B are the total pre-edge cross-sections of components A and B respectively. The Y's indicate the corresponding yield of electrons at the surface per absorbed photon for the three absorption channels.

Upon substitution of these equations in (7.1) we obtain

$$S = \frac{(1-x)a}{1+x(b-1)}, \qquad (7.4)$$

where $a = \sigma_e Y_e / \sigma_o Y_o$ and $b = \sigma_B Y_B / \sigma_o Y_o$. For $b = 1$ we obtain a linear dependence, as was found experimentally for the Tb signal. From tabulations of calculated partial cross-sections[15] we obtain a Tb –pre-edge cross-section ratio $\sigma_{Ni}/\sigma_{Tb} = 1.6$, giving $Y_{Ni} = 0.6 Y_{Tb}$ at a photon energy of 1230 eV. Since the absolute cross section of the edge is not know, it is not possible to obtain the ratio between the pre-edge to edge yield ratios from the value obtained for a=19.

For the Ni data points in Fig. 7.5 we obtained a good fit for $b = 9$. Again using the tabulated cross-sections we have $\sigma_{Tb}/\sigma_{Ni} = 4.5$, giving $Y_{Ni} = 0.5 Y_{Tb}$ at 850 eV.

7.3.3 Tb/Ni overlayers

In Fig. 7.6.a we present the peak-normalized raw Ni L_3 total yield spectra of clean Ni(110) and Ni with different coverages of Tb up to 60 Å, obtained by succesively adding extra layers. The series was taken during one injection of the storage ring. We find the only effect of the overlayer is an increase of the high energy tail of the spectrum, which is caused by an increase of the slope of the absorption background.

From a number of studies[153, 154, 155, 156, 157] of rare earth overlayer growth on Ni and Cu it is known such layers form in a layer-by-layer mode when the substrate is at room temperature. Although conclusions about the growth

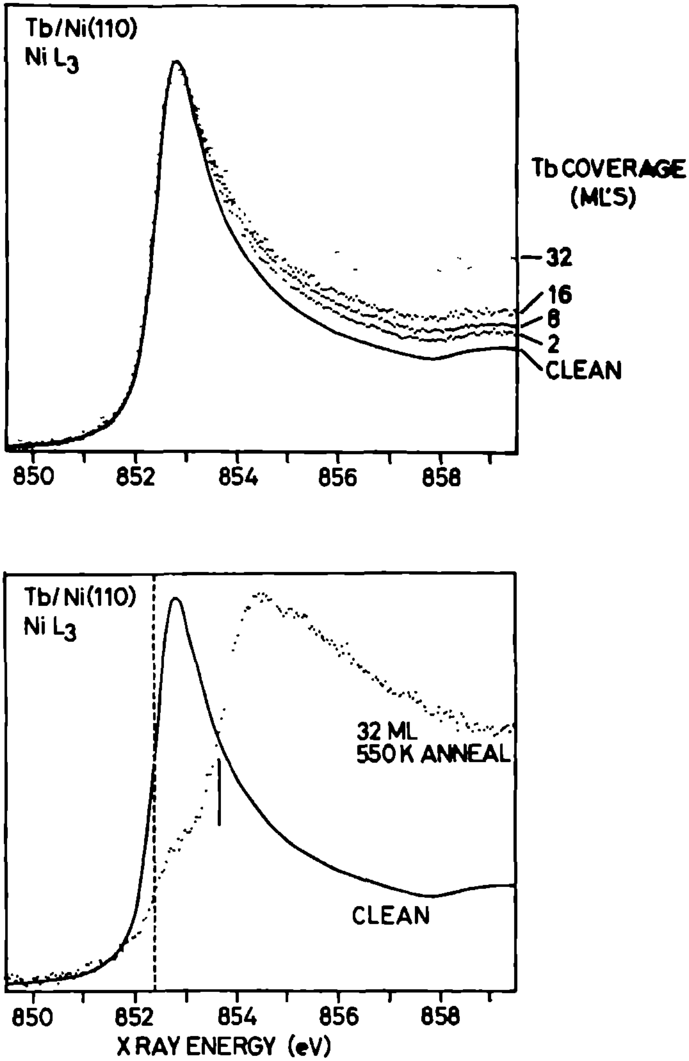

Figure 7.6: a. Normalized Ni L_3 XAS spectra of clean Ni(110) and Ni covered by Tb overlayers of increasing thickness, deposited at room temperature. The total thickness was obtained by adding new layers to the ones already deposited.
b. Ni L_3 edge of 170 Å Tb film after annealing for 5 min. at 550 K. The clean Ni spectrum is given for comparison.

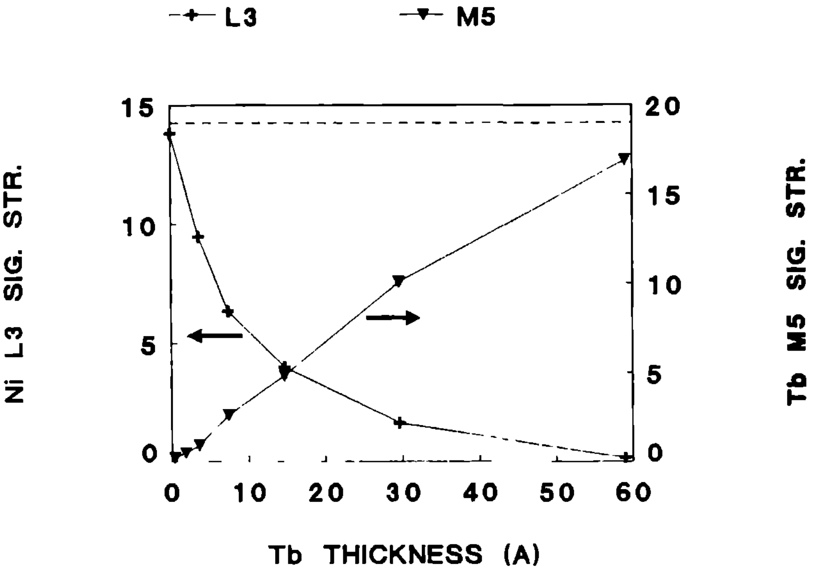

Figure 7.7: Coverage dependence of the signal strength of the Tb M_5 edge and the Ni L_3 edge of the Tb/Ni(110) system.

mode can not be drawn from our measurements alone, evidence against important alloying at the deposition temperature (room temperature) is obtained from Fig. 7.6.b, where we compare the clean Ni spectrum with the spectrum of the 60 Å overlayer after annealling for 5 minutes at 550 K. The double edge structure is a clear signs that a reaction takes place only at these elevated temperatures, in good agreement with what is observed in the cited references. From the tendency of the Ni L_3 edge to shift to heigher energies found for the bulk system we are able to interpret the double structure as being a superposition of the edge of the pure bulk Ni spectrum and the spectrum of Ni dissolved in Tb. The peak position of the latter contribution is shifted by 1.9 eV relative to the pure Ni edge, which is much more than the shift of 1.0 eV found for Tb_3, indicating a stronger dilution of Ni in Tb in the annealed layer.

The coverage dependences of the signal strength of the M_5 edge of Tb, and of the L_3 edge of the Ni substrate. are given in Fig. 7.7. The curves are remarkably similar to the corresponding curves of the compound series (Fig. 7.5). Apparently, the morphology of the sample is not of primary importance. Since we were able to explain the curves in Fig. 7 5 from the concentration dependence alone, the correspondence between the two graphs indicates that in the overlayer experiment we are sampling a surface layer of constant thickness, in which Ni is gradually replaced by Tb. In other words. it follows that the probing depth profile is roughly rectangular. Since even in the thickest layer the Tb signal is not yet saturated, we estimate the probing depth to be slightly over 60 Å.

7.4 Conclusion

We have presented a systematic study of the Ni $L_{2,3}$ and Tb M_5 edges of the Tb—Ni intermetallic compound system. It was found the Ni L_3 peak shifts by up to 1 eV to higher photon energy upon increase of the Tb concentration. The peak to post-edge plateau ratio stays roughly constant, in marked contrast to what was found in a great many of other Ni alloys.

The measured concentration dependence of the signal strength could be explained very well. We have shown this ratio can give useful extra information from XAS measurements, especially in the soft x-ray range where reliable beam intensity monitors are not yet available, so that the edge-jump[124], which is the more informative quatity, can not be measured.

Furthermore, the signal strength analysis allows the sensitivity of XAS in total electron yield to be quantified. The present study shows measurements of Tb impurities in Ni are much more feasible than the inverse case.

From the results of a parallel study of the Tb/Ni overlayer system we conclude no important interface reaction takes place during room temperature deposition, in accordance with other studies[153, 154, 155, 156, 157]. By comparing the dependencies of the signal strength on the Tb concentration of the bulk system and the Tb thickness of the overlayer system we conclude the probing depth is ≥ 60 Å. We note that an experiment on the Ni L_3 edge alone would have lead one to conclude that the probing depth is only ~ 10 Å.

Acknowledgements

We are grateful to Prof.Dr. K.H.J. Buschow for providing us with the Tb—Ni samples.

Chapter 8

X-RAY DICHROISM AS A PROBE OF THE SYMMETRY OF ULTRA-THIN RARE EARTH OVERLAYERS

Abstract

Strong x-ray dichroism is observed in the 3d XAS spectra of ultra-thin overlayers of rare earth elements on Ni(110) surfaces. The dichroism is present already at room temperature in the as-deposited films, and increases markedly upon annealing and upon cooling. The results are thought to be due mainly to exchange splitting of the ground-state, but as discussed crystal fields may be important for the observed effects.

8.1 Introduction

Strong polarization dependence (or dichroism) is known to occur in the atomic-like 3d x-ray absorption spectra of the rare earth elements, as we have described earlier both theoretically[2, 100] as experimentally[135]. In this paper we present the first application of x-ray dichroism to a practical problem, *in casu* the magnetization of rare earth overlayers on the ferromagnetic Ni(110) surface.

Rare earth overlayers on magnetic transition metal surfaces are currently under investigation because they present an excellent opportunity to study the interaction of localized magnetic moments with an itinerant substrate. Several interesting scientific questions can be raised, such as

- what is the magnetic anisotropy of the overlayer?

- does the overlayer change the anisotropy of the substrate near the surface?

- What is the spatial extent of the exchange coupling of the substrate into the overlayer, and how does the magnetic order of the substrate affect that of the overlayer?

- How does the surface structure influence the magnetic properties, such as ordering temperatures, moments and anisotropies?

- If present, what is the influence of the rare earth orbital moment on the above questions?

From an applied viewpoint these questions are also relevant, since compounds of rare earths with more delocalized magnetic elements are key materials for the development of stronger permanent magnets[111, 143, 142] and magneto-optical storage media[45, 46].

Several groups are carrying out systematic research of the structural and electronic properties of RE overlayers on single crystals of Ni[158, 159, 156, 157, 160, 161] and Cu[162, 153, 154, 155], motivated by the effectivity of RE/TM systems as catalysts for the production of ethanol. Especially Yb overlayers has been studied[158, 159, 156, 160, 161] because this element in addition shows mixed-valence behaviour on surfaces[163].

The magnetic properties of RE overlayers on single crystals of magnetic transition metals have already been studied by Landolt *et al.* [164, 165, 166]. Using spin-polarized Auger spectroscopy these authors found the first monolayer of Gd deposited on Fe(100) orders anti-parallel to the Fe magnetization. The ordering temperature of this system was found to be 800 K, which is intermediate between the Gd Curie temperature (293 K) and that of Fe (1043 K). Increase of the layer thickness leads to a decrease of the observed spin-asymmetry, which at 360 K vanishes at 8 Å. Still, these thick films are found to order antiparallel to the Fe substrate magnetization at the Curie temperature of bulk Gd. The authors conclude the Gd-Fe exchange interaction across the interface is responsible for the high ordering temperatures of the thin overlayers, and that it is sufficiently strong to orient the magnetization of thicker Gd films.

Ultra-thin layers of exactly the same system were studied with spin-polarized photoemission (SPPES) by Carbone *et al.* [167]. They observed an electron spin polarization of the Gd 4f signal of 70% at 100 K, accompanied by a partial depolarization of the Fe valence band signal. Also strong ordering of rare earth overlayers on Fe single crystals at 300 K has been reported /Rochow, private communication/

The above work, as well as nearly all the work on the magnetism of free RE surfaces[168, 169, 170, 171, 172, 173, 174], was performed on Gd, which is the only rare earth element that has no orbital contribution to the magnetic moment. This has as two important consequences: firstly crystal field effects are not important, resulting in low magneto-crystalline anisotropy, and secondly the absence of angular correlation terms makes it the only RE element in which the 4f levels can be treated with success in the single-particle approximation[175, 176] to obtain ground state properties.

At present, the only published experimental study of the surface magnetic properties of $L \neq 0$ RE elements seems to be that of Rau *et al.* [177]. Using electron capture spectroscopy (ECS) they found that a 3 monolayer film of bcc Fe(100), grown epitaxially on a Ag(100) surface, posseses an in-plane zero-field magnetic anisotropy, which is converted to perpendicular anisotropy on covering with a 2 monolayer Tb film.

The RE/TM system and RE surfaces have been investigated theoretically also, in part inspired by the above experiments[178, 179, 180, 181, 182, 183]. Peschel and Fulde[178] and Hsieh and Pink[179] studied the effect of the lower surface coordination on the magnetization of rare earth compounds. They predict an enhancement of the surface magnetization, in particular for materials with a non-magnetic singlet crystal field ground-state. Camley[181] gives a phase diagram for the magnetic structure of a RE overlayer on Fe as a function of thickness and temperature, using a simple mean field model with Fe Fe, Fe–RE and RE RE coupling constants as input. Blügel[184, 185] performed non-relativistic density-functional calculations for Gd adsorbed on Fe(100) and Ni(100) surfaces. He reported an antiferromagnetic ground-state in the case of iron while for Ni the ferromagnetic and antiferromagnetic calculatations differed little in energy. Due again to the $L = 0$ ground-state, Gd is the only RE for which such calculations can be performed with reasonable accuracy.

In this chapter we present initial results on the use of magnetic x-ray dichroism (MXD) as a probe for the magnetism of ultra-thin overlayers. Such dichroism has been predicted[2] and proven to exist[135] in the 3d→4f x-ray absorption spectra of ordered rare earth materials. MXD can be thought to arise from the deformation of the spherical symmetry of the 4f levels as a result of the lifting of the degeneracy of the atomic substates by a magnetic field[100].

MXD effects in Gd are expected to be small when using linearly polarized x-rays. The Tb/Ni(110) system was selected because Tb has next to Gd the highest magnetic ordering temperatures in the pure metal and in RE—Ni compounds. Also the most important absorption edges of this system, *i. e.* the Tb M_5 edge and the Ni L_3 edge, are both accessible to a double beryl crystal monochromator, allowing both substrate and overlayer to be studied together. A study of the chemical information contained in the spectra and those of the Tb—Ni intermetallic compounds is presented elsewhere[186].

The paper is organized as follows. After discussing some experimental details in the next section we present the observed thermal- and angular dependences of the absorption spectra in section 3; first for the as-deposited layers and then for annealed layers. These results are discussed in section 4 using a model in which the 4f ions are treated atomically. This interpretation is compared with one in terms of crystal field splittings. Section 5 rounds off the paper with conclusions.

8.2 Experimental

The Ni(110) crystal of 10x5x1 mm was cut from the boule by spark erosion with an easy direction of magnetization $[1\bar{1}1]$ along the longest dimension. Both (110) faces were given a rough polish with fine grained sandpaper. The front surface was polished mechanically using successively finer grains of diamond paste (15-0.25 μm). After polishing the sample was annealed for 24 hours at 650°C under a hydrogen flow at a pressure of 10^{-7} Torr to remove sulfur impurities from the sample.

Mounting of the sample was achieved by spotwelding it on two W/Rh wires (diameter 0.45 mm) protruding 5 mm from two Cu blocks which were sandwiched between two saphire platelets. This sandwich was pressed with one side against the main copper sample block of a helium cold finger using a pair of M3 bolts. The saphire supplied the necessary electrical and thermal insulation when the sample was heated, and the good thermal contact at low temperatures. The minimum temperature of the sample block was 50 K, while the lowest temperature achieved on the sample was 70 K. Temperatures were measured with a K-type thermocouple which was also spotwelded on the back of the sample. Also, the sample could be heated to 1300 K by electron bombardment on the back surface while the cryostat was kept cold. The cryostat could be rotated around its vertical axis without breaking vacuum by means of a differentially pumped rotary feedthrough. Further details of the experimental set up are described elsewhere[187].

After insertion in the vacuum the sample was further cleaned in vacuum by the usual cycles of sputtering and annealing. 1x1 LEED surfaces were obtained with C contamination less than 10% of a monolayer as judged from Auger spectra. No sulfur contamination was found.

The sample could be magnetized along the $[1\bar{1}1]$ direction by a small c-shaped electromagnet with a gap of 11 mm that embraced the sample, leaving a vacuum gap of 0 5 mm between both sides of the sample and the magnets' poles (see Fig. 8.1). The magnet could be pulsed to a maximum field strength of 5 KGauss which is more than sufficient to saturate the sample. Ex-situ magneto-optical Kerr effect (MOKE) measurements performed after completion of the absorption experiments showed the sample could be saturated easily. However, the remanent magnetization was found to be only $\sim$ 70 % of the saturation value . The apparent failure to arrive at a single domain state in remanence is ascribed to the size of the vacuum gap between the poles and the sample, and to crystal defects induced by the spotwelding method of mounting the crystal.

Tb overlayers were deposited on the Ni sample from a Knudsen cell furnace with a rate of $\sim$ 1 Å/min. During deposition the sample temperature stayed at 300 K. Layer thicknesses were determined with an oscillating quartz crystal monitor with an estimated systematical error of 40%. During annealing and evaporation the base pressure of 2x10 ^{10} Torr rose to 1x10 ^{9} Torr. When speaking of a Tb monolayer below we mean a single layer of the hcp lattice of Tb metal, which has a thickness of 2.85 Å.

The experiments were carried out in the commisioning phase of a newly constructed windowless UHV double crystal monochromator at Super-ACO, LURE, Orsay[188]. The x-ray absorption spectra were accumulated at angles between $-45°$ and $+70°$ degree off-normal-incidence using the total electron yield method. Thanks to the high flux from this presently unfocussed beamline the beam dimensions could be reduced to 0.1x0.1 mm for the grazing-incidence experiments without appreciable increase of the data acquisition times.

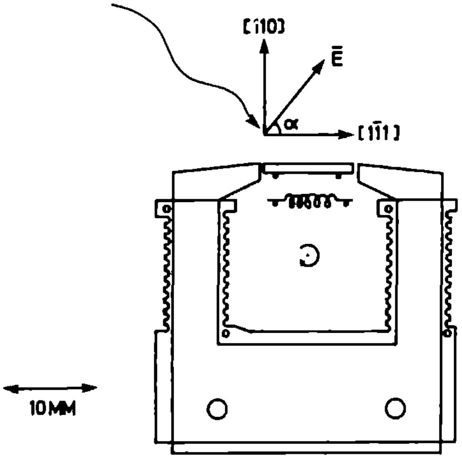

Figure 8.1: Layout of sample holder and magnet. The magnet windings are not shown. The complete assembly could be rotated in the horizontal plane (plane of drawing).

8.3 Results

8.3.1 Interface structure and kinetics

A number of detailed studies has been performed on the kinetics of rare earth overlayers on different Ni[158, 159, 156, 157, 160, 161] and Cu[162, 153, 154, 155] crystal faces. The behaviour has been found to be quite complex, but some traits common to all systems can be discerned. At room temperature the rare earth overlayer has been found to grow in a disordered layer-by-layer mode[158, 162, 157], although some intermixing of the interface layers may occur[157]. At higher deposition temperatures or after annealing, thin layers are found to form ordered structures, with a wide variety of complex LEED patterns occuring for different choices of thicknesses, deposition temperatures and crystal faces[153, 157]. Also, by annealing at higher temperatures the amount of overlayer material decreases[155], although it is unclear at present whether the material diffuses into the bulk or evaporates from the surface. The results for annealed surfaces have been interpreted as indicating the formation of a surface compound with a thickness in the range of 1 monolayer[157, 155]. The same marked tendency to passivate the substrate with the formation of sharp reacted interfaces is generally observed in RE/semiconductor systems[189]. The structure of this surface compound appears in most cases to be unlike that of any of the known bulk RE—TM intermetallic compounds[162, 157, 155].

Unfortunately, the surface kinetics of rare earths on the Ni(110) face has been studied in least detail. Chorkendorff *et al.* [158] in a study of Yb on Ni(110) report a behaviour as described above. In particular, the ordered Yb—Ni surface compound formed after prolonged annealing is found to consist of ~30% Yb[158].

This picture is corroborated by the results of a study comparing the Ni 2p x-ray absorption spectra of the Tb/Ni(110) interface with those of the NiTb intermetallic compounds, which is published elsewhere[186]. There we found that upon annealing thick overlayers for some minutes at 500 K, the L_3 edge of the Ni substrate shifts about 0.9 eV to higher binding energy, indicating an interface reaction takes place above room temperature. At the same time the signal strength (defined here as the peak signal divided by the pre-edge intensity) of the Tb signal is found to decrease and that of the Ni peak to increase, indicating a decrease of the amount of Tb on the surface. However, after a sharp initial decrease the signal strengths change only very slowly if at all. Also after prolonged annealing Tb remains clearly visible in the Auger spectrum. Finally, upon annealing of 1 3 monolayer films, sharp LEED patterns showing second and third order spots were found to reappear, including (1x1), (2x1), and (3x1) patterns. No systematical study correlating LEED patterns with deposition times and annealing conditions could be made yet.

A schematical diagram of the Ni(110) surface is given in Fig. 8.2. The fcc (110) surface consists of rows of atoms along the $[1\bar{1}0]$ direction, with the tops of the atoms of the second layer forming the bottom of the holes formed by the atoms of the rectangular surface-unit-cell. Also depicted are three Tb atoms absorbed on such sites. Assuming the radius of the free Tb atom, it is evident that Tb atoms fit very nicely in two adjacent rectangular sites in the $[1\bar{1}0]$ direction but not in the [001] direction. The symmetry of these rectangular absorption sites is C_{2v}.

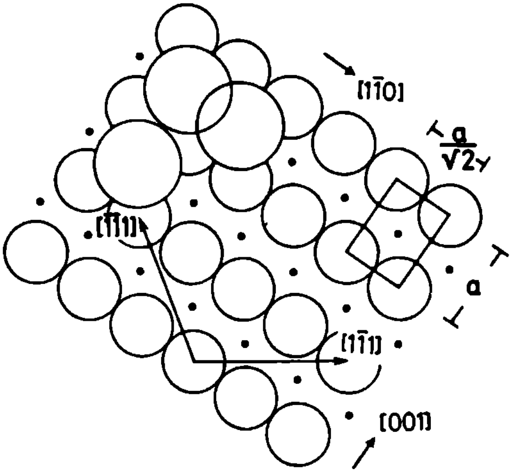

Figure 8.2: Schematical diagram of the fcc Ni(110) surface. The top layer Ni atoms with radius $a/2$ are indicated by the small circles ($a = 3.52$ Å is the lattice parameter). Heavy dots represent the position of the second atomic layer. The square represents one surface unit cell. The three large circles indicate Tb overlayer atoms, with radius 1.8 Å appropropriate for the neutral atom.

8.3.2 Dichroism of as-deposited layers

In describing the dichroism spectra below we will use the polarization angle α defined as the angle between the horizontal polarization vector and the in-plane [1$\bar{1}$1] direction. At normal incidence $\alpha = 0°$; at the smallest grazing incidence used here $\alpha = 80°$.

As is well known(see *e. g.* Thole *et al.* [29] and references therein) the 3d absorption spectrum of rare earth materials is given by the part of the final state multiplet that is allowed by the selection rules. These multiplets are divided in $3d_{5/2}$ and $3d_{3/2}$ parts by the 3d core hole spin-orbit interaction. We will consider here only the Tb $3d_{5/2}$ spectrum; the $3d_{3/2}$ was found to display only very small dichroism effects, as expected theoretically also[100].

The Tb $3d_{5/2}$-XAS spectrum of polycrystalline Tb materials consists of two peaks separated by a shallow minimum and flanked by shoulders of *ca.* one third of the main peak-height (see *e. g.* Fig.8.7.) In Fig. 8.3(a) we show room temperature spectra of a 1 monolayer (2.85 Å) Tb film taken respectively at $\alpha = 0°$ and 70°. As for all spectra discussed here, the spectra were peak-normalized, possibly after subtraction of a sloping linear background[190].

The spectra are clearly seen to be dichroic: at $\alpha = 0$ the high energy peak is lower in intensity than the low energy peak and the shoulders, while at 70° the situation is reversed. Such dichroism has earlier been found in Tb iron garnet[135, 191], and arises from the thermal dependence of the occupancy of the ground-state Zeeman levels[2]. The observation of the effect at room temperature indicates a total splitting of the atomic ground-state of the order of some hundreds of Kelvin. indicating a very large exchange interaction.

The displayed dichroism is small in comparison to theoretical predictions for magnetically saturated ions ($T = 0$ K), wherein in both cases one of the peaks is expected to disappear completely[100]. Also the effect shown in Fig. 8.3(*a*) is slightly smaller than what was found earlier[135] for Tb iron garnets at 55 K. Cooling these as-deposited overlayers to 70 K led to a slight increase of the effect, as evidenced by the slight decrease of the high energy peak of the $\alpha = 0$ spectra shown in Fig. 8.3(*b*).

The dichroism was found to be strongly dependent on the thickness of the overlayer. This is illustrated in Fig. 8.4 where we reproduce room-temperature normal-incidence spectra of overlayers with increasing thicknesses obtained by successive additions of new material to previously deposited layers. The effect is clearly strongest for the 1/4 monolayer film, and decreases already before completion of the first monolayer.

From the dependence of the signal strengths of the Tb M_5 and Ni L_3 edge intensities as a function of thickness we found the sampling depth of XAS in total electron yield mode. defined as the thickness of the surface layer from which 90% of the signal originates, to be ~60 Å[186]. The spectra of Fig. 8.4 thus represent the layer-integrated signal. Therefore the decrease in the dichroism asymmetry is likely to be due to a dilution of the signal from the interface Tb layer by that of the following, and apparently already the second layer is very much less ordered.

8.3.3 Dichroism of annealed layers

Fig. 8.5 shows the strong increase in the peak asymmetry of the room temperature normal-incidence spectrum of a 2 ML film upon annealing. A representative pair of measurements of annealed layers comparable with Fig. 8.3 is given in Fig. 8.6. Paradoxially, changes in the LEED pattern did not seem to affect the dichroism asymmetry.

The spectra of the annealed layers were found to depend more strongly

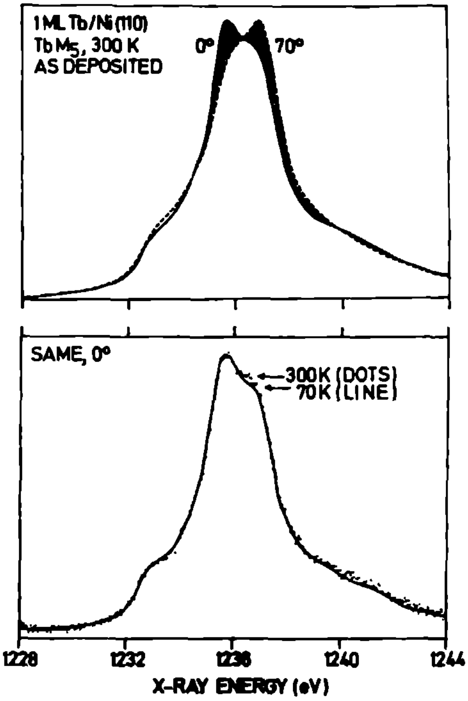

Figure 8.3: (*a*) Room temperature terbium M_5 XAS spectra of 1 monolayer Tb as-deposited on Ni(110) surface. The angle between the polarization vector E and the surface $[1\bar{1}1]$ direction is 0° and 70° respectively. The hatched area indicates the difference between the curves. The spectra were peak normalized after subtraction of a linear background.
(*b*) Normal incidence spectra showing the slight increase of the dichroism on cooling to 70 K.

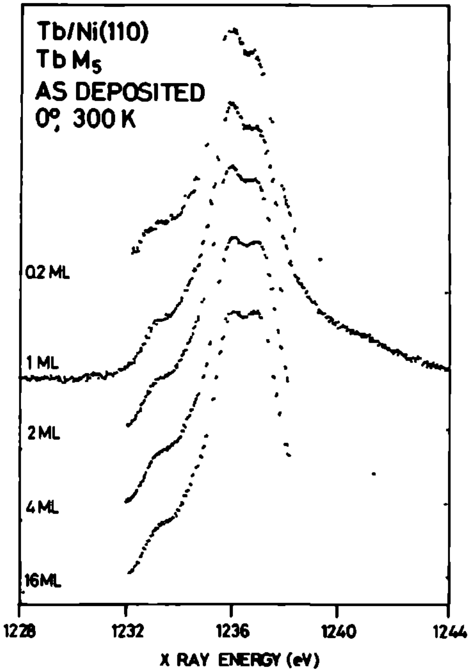

Figure 8.4: Tb M_5 XAS spectra of Tb overlayers of increasing thickness The total thickness was obtained by evaporating new material on top of the previous layer. The spectra were taken at room temperature and at normal incidence.

on temperature, as exemplified by the lowest curve in Fig. 8 5. As in the as-deposited layers, the dichroism was strongest for the thinnest films. For reference, in Fig. 8 7 we reproduce the spectrum of an annealed film of 1/4 ML at 70 K, which displayed the strongest dichroism found for Tb up to now. Total measurement time of this spectrum was 2 hour, with a signal-to-background ratio of 0.3 During this time the spectrum asymmetry did not change appreciably The acquisition of grazing incidence ($\alpha = 70°$) at low temperatures was impossible because the cryostat was unstable at low temperatures because of varying thermal stresses.

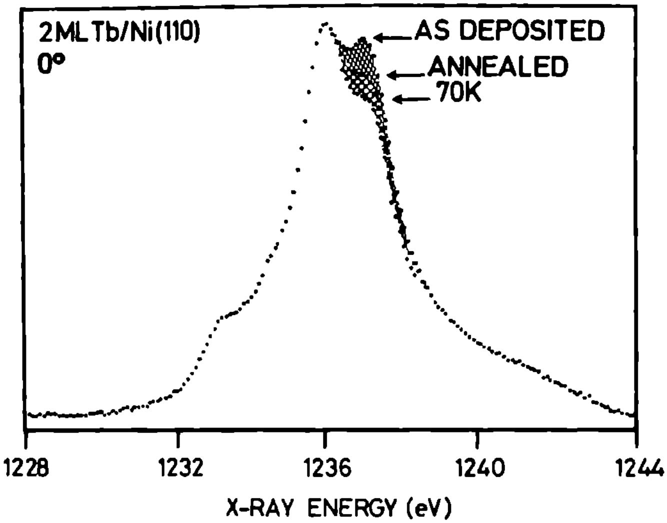

Figure 8.5: Evolution of the normal incidence Tb M_5 spectrum of a 2 ML film on Ni(110). Arrows indicate the height of the right shoulder after deposition ($C = 0.04$), after annealing($C = 0.08$), and after cooling to 70 K ($C = 0.16$). The first two spectra were acquired at room temperature. The values for C are arrived at as discussed in section 8.4.

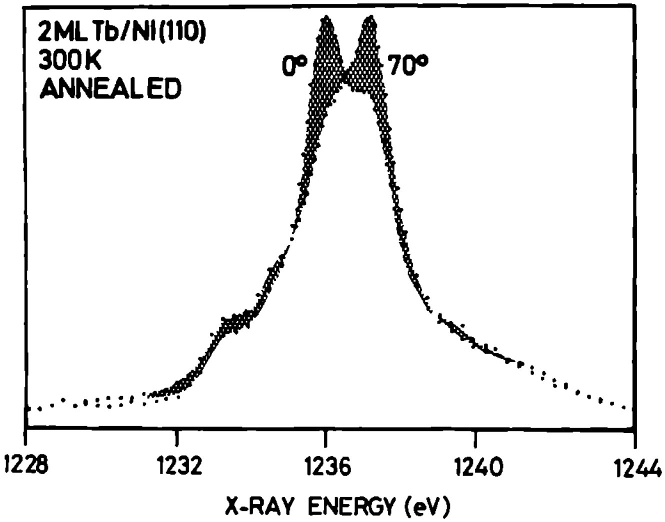

Figure 8.6. Room temperature Tb M_5 spectra of a 2 ML Tb film as in Fig. 8.3 but after annealing. Note the dispersion of the low left shoulder.

8.4 Atomic model analysis

We will analyse the data presented above in terms of a magnetized free-ion model[86]. It can be shown theoretically that, within the free-ion model and with linearly polarized light, for any combination of temperature, magnetic field, or polarization angle α the dichroic spectrum is an element of a continuous set of spectra, with each member of the set determined by the value of the so-called linear dichroism parameter C. This linear dichroism parameter is the product of an angular dependent term C_α and a magnetization term C_M[135]. For a free ion the angular term C_α has the form

$$C_\alpha = \frac{3}{2}\cos^2\alpha - \frac{1}{2}, \tag{8.1}$$

where α is the polarization angle, and ranges between $-1/2$ and 1. C_M ranges between 0 and 1, so that $C = C_M C_\alpha$ also has values between $-1/2$ and 1. From 3.19 of Chapter 3 we find for Tb

$$C_M = \frac{\langle M^2\rangle - 14}{22}, \tag{8.2}$$

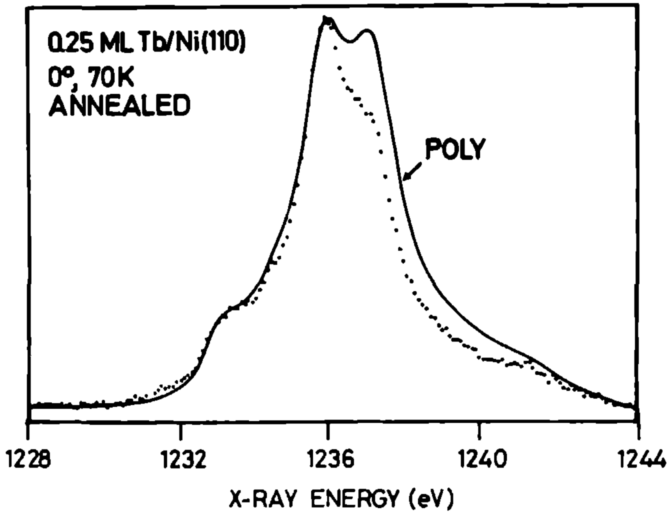

Figure 8.7: Dots: Normal incidence spectrum of 0.25 ML Tb after anealing, measured at 70 K (C = 0.25 ± 0.05). For comparison the spectrum of a polycrystalline film is also drawn (solid line).

where $\langle M^2 \rangle$ is the thermal average of the square of the magnetic quantum number M of the atomic ground-state levels $|JM\rangle$. Since $\langle M^2 \rangle$ in the free-ion model is a (Brillouin-like) function of the reduced temperature $\Theta = kT/g\mu H$ only, the C_M term completely describes the temperature- and field-dependence of the linear magnetic dichroism[135].

By fitting the measured spectra with the atomic predictions it is possible to obtain experimental values for C. This is demonstrated in Fig. 8.8 where we compare the experimental spectra of Fig. 8.6 with the best theoretical simulations, obtaining C values of 0.18 and -0.25 respectively.

The C values obtained in the same way for a number of normal incidence spectra of annealed overlayers of different thicknesses are plotted in Fig. 8.9 as a function of temperature. From this graph the above observed increase of the dichroism effect with decreasing thickness is apparent. Also seen that the variation with temperature is stronger for the thinner layers. Postponing a full discussion of this graph until later, we remark here that even for the thinnest layer, 0.25 ML, the increase of C upon cooling is about 3 times smaller that expected for a free-ion in a constant magnetic field. Since the

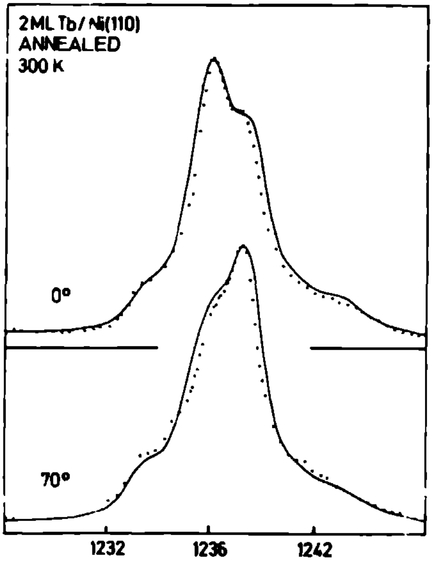

Figure 8.8: Dots: spectra as in Fig. 8.6. Solid line: theoretical fits with dichroism parameters $C = 0.18$ (0°) and $C = -0.25$ (70°).

Ni substrate magnetization is nearly constant[13], increasing from 95% of the saturation magnetization to 97% at 70 K, this indicates a deviation from a free-ion-like behaviour.

The spectra shown in Fig. 8.8 represent the extrema of the dichroism effect found in an angular scan in which the polarization angle α was varied from $-40°$ to $80°$. The C values obtained from fits to these spectra are plotted in Fig. 8.10. The angular dependence is seen to be symmetric around normal incidence, while the extreme values are comparable in absolute value. For comparison the free-ion behaviour is also drawn, with C_M choosen to normalize the C_α curve at $\alpha = 0$ (see eq. (8.1)). The second curve gives the expected behaviour on the basis of a two-domain model discussed in section 8.5.1.

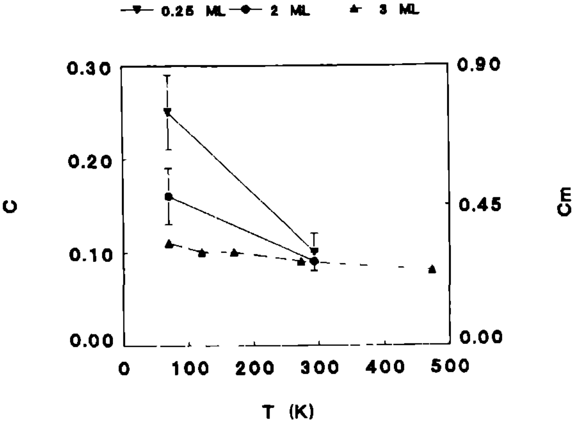

Figure 8.9: Temperature dependence of the linear dichroism parameter C for annealed overlayers of different thicknesses. The right-hand scale is arrived at as explained in the discussion.

8.5 Discussion

8.5.1 Free-ion Interpretation: Two-domain Model

In a ferromagnetic material the deformation of the 4f-electron cloud giving rise to the observation of dichroism can be due to magnetic (exchange) or crystal field interactions. In rare earth materials the two can be of comparable magnitude. We will first analyze the data under the assumption crystal fields can be neglected; in the next section we will discuss the possibility of a crystal field origin for the dichroism effects. We will concentrate the discussion on annealed layers, since there the largest effects were observed.

Angular dependence

From the comparison of the measured angular dependence of C with that expected for free magnetized ions (Fig. 8.10), it is evident that the overlayer magnetization is not simply parallel to the direction of the applied magnetic field. This is compatible with the a-posteriori MOKE experiments, which showed the remanence signal of the Ni substrate was near 70% of the saturated value. This indicates that next to the $[1\bar{1}1]$ direction other domains

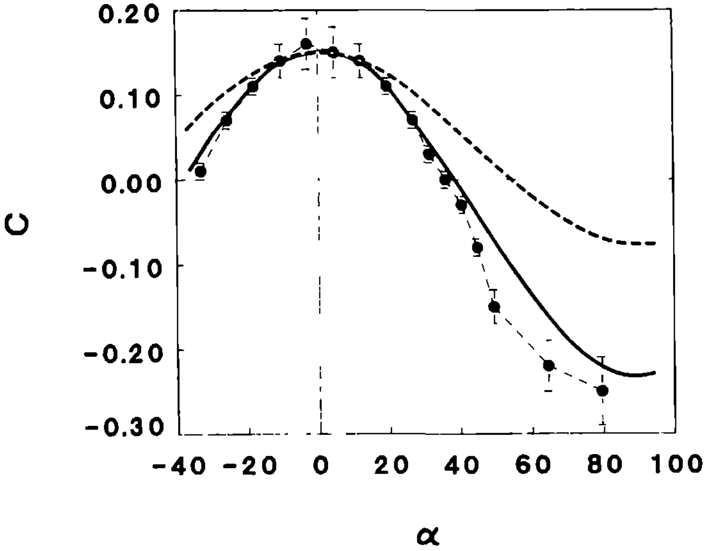

Figure 8.10: Angular dependence of the linear dichroism parameter for an annealed 2 ML Tb film, taken at room temperature. Also shown are the expected behaviour of a ferromagnetic surface layer (dashed line) and a two-domain model discussed in the text (full curve).

are occupied. Since domains pointing out of the surface are energetically unfavorable, we make the assumption that the surface magnetization consisted of domains parallel to the $[1\bar{1}1]$ and $[\bar{1}\bar{1}1]$ directions[192] (see Fig. 8.2), with equal amounts of the surface occupied by the equivalent directions of magnetization (two-domain model).

The angular dependence of the spectrum is then the average of that of the two domains. Using simple trigoniometry we obtain $C_\alpha = \frac{5}{6}\cos^2\alpha - \frac{1}{2}$ for the two-domain model. This angular dependence is also plotted in Fig. 8.10, again normalized on the measured normal-incidence value. This curve is seen to fit the data quite well, especially taking into consideration that the largest experimentally found $|C|$ values may be underestimated because of problems with the fitting procedure[191]. Special importance has the fact that this model predicts correctly the angle at which the effect disappears (37.4°), since this point can be determined by direct comparison to unpolarized spectra, independently from fitting to theoretical curves.

T (K)	C_M	Θ	H (Tesla)
70	0.75 ± 0.15	1.12 ± 0.15	50
300	0.30 ± 0.06	3.30 ± 0.60	80

Table 8.1: C_M values and derived effective temperature Θ and exchange field H of 1/4 ML film assuming a two-domain model, see text.

Thermal dependence

From the angular dependence of the two-domain model we obtain $C(\alpha = 0) = 1/3$, so that at normal-incidence $C = C_M/3$. Assuming the above model is correct, independent of the overlayer thickness, we apply it to the temperature dependence of the normal-incidence spectra of annealed layers, obtaining the C_M scale on the right of Fig. 8.9. Taking the 1/4 ML data as being representative for the interface layer, and using the atomic expression eq. (8.2) for C_M, we obtain values for Θ and the exchange field H as listed in Table 8.1. At 70 K we find $C_M = 0.75 \pm 0.15$, giving $\langle M^2 \rangle = 30.5$. Since the saturation value of $\langle M^2 \rangle$ is 36, this would mean the ions on the interface are highly ordered at this temperature. The ratio $\Theta(70^\circ)/\Theta(300^\circ) = 0.23$ (see Table 8.1), while for a free-ion in a constant field we would expect $\Theta(70^\circ)/\Theta(300^\circ) = 70/300 = 0.33$. Apparently Θ decreases more slowly than expected from the free ion temperature dependence. We interpret this as a deviation of the free ion behaviour due to crystal field effects, although in part it may be due to experimental problems like the uncertainties in the fitting procedure for large C [191], a wrong choice of $C(\alpha = 0)$ or the presence of disordered islands in the surface.

The order of magnitude of the exchange fields obtained from the Θ values (assuming a free-ion $g = 3/2$) is correct for a ferromagnetic system. The decrease with temperature is unlikely to be realistic and underlines the problems mentioned above. Since all Tb–Ni intermetallic compounds have ordering temperatures below 180 K, it is unlikely this exchange field is generated by the ferromagnetism of the surface compound. It is more likely that the exchange field originates from the Ni substrate magnetization.

8.5.2 Crystal field interpretation

Ions on surfaces have highly anisotropic surroundings, which are known to lead to dichroic effects in XAS and EXAFS spectra of adsorbates[72, 73]. As an alternative to the exchange splitting interpretation discussed above, we will discuss shortly surface crystalline field effects. For rare earths materials surface effects have been studied theoretically by Peschel and Fulde[178, 183] and Hsieh and Pink[179]. These studies concentrate on the lower coordination at the surface, which for some symmetries can lead to a reduction of the crystal field splitting. The concommitant partial restoration of the orbital momentum may lead to higher moments and higher ordering temperatures at the surface.

These studies also stress that the crystal field potential on the surface will contain axial terms which even may dominate the potential. Such terms, which with the use of Stevens[66, 67] operator-equivalent notation are written as O_l^0, $l = 2 \cdots 6$, split the atomic ground-state of Tb in a series of doublets $|\pm 6\rangle' \cdots |\pm 1\rangle'$ and a singlet $|0\rangle'$. (The primes are used to distinguish the crystal field wavefunctions, which are quantized relative to the surface normal, from the exchange-split functions, which were quantized along the in-planar $[1\bar{1}1]$ axes.) Such axial terms are certainly present for Tb ions absorbed in the rectangular hollows of the Ni(110) surface. From the symmetry of the crystal field alone it is impossible to tell whether the $|\pm 6\rangle'$ doublet or the $|0\rangle'$ level is the ground-state. However, by comparison of simulations of the spectra for each of these two cases we find the singlet ground-state is compatible with the observed peak asymmetry, as will be shown in the next section.

8.6 Comparison

A qualitative comparison of the two-domain model and the $|0\rangle'$ crystal field model is given in Fig. 8.11 Here the experimental room-temperature spectra for $\alpha = 0°$ and $70°$ incidence are plotted together with the simulated curves for the two-domain model and the crystal field singlet ground-state $|0\rangle'$. Both simulations were necessarily done for $T = 0$ K, since the strength of the exchange and crystal fields is not known. The fact that both models have the main intensity on the same side reflects the similarity of the deformation from spherical symmetry of the wavefunctions in both cases: $|0\rangle'$ is elongated along the surface normal, while $|-6\rangle$ is flattened in the direction of the $[1\bar{1}1]$

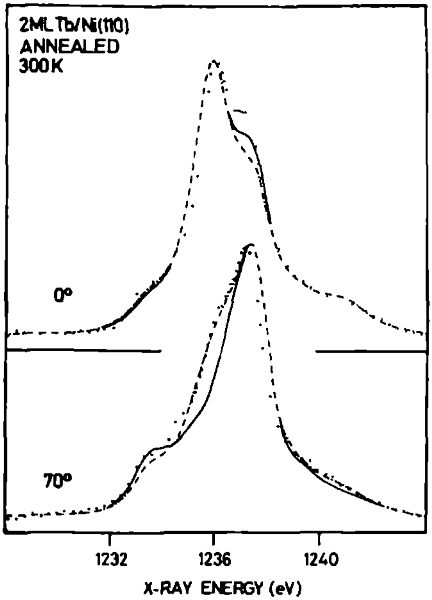

Figure 8.11: Comparison between $T = 0$ K theoretical curves based on the two-domain model (dashed) and the $|0\rangle'$ crystal field (solid curve) ground-state models. Experimental data are the same as in Fig. 8.6.

direction. Thus both have more electron density along the surface normal than along the $[1\bar{1}1]$ direction.

From the figure it is seen that, compared to the $|-6\rangle$ exchange-split ground-state spectrum, the crystal field $|0\rangle'$ ground-state spectrum fits the experiment better at 0°, but worse at 70° degree. We wish to stress the point that the $|0\rangle'$ ground-state spectrum is unlike in shape from any spectrum that can be generated with the linear dichroism parameter C, indicating that in principle it is possible to tell the importance of crystal field splitting from the spectral shape alone.

In both cases the fits are clearly not realistic since they represent $T = 0$ K models, and one has to include contributions to the spectrum from the excited levels in the splitted J manifold. Because these contributions will tend to restore the spherical symmetry of the ion, in general they will decrease the dichroism. Also, the crystal field potential contains other terms $O_l^{m\neq0}$. Such terms will mix the $|M\rangle'$ doublets, which has the same effect as thermal averaging, with the extra feature that it may lead to different angular dependences of the dichroism.

Finally we will discuss some structural aspects. From the dependence of the dichroism on the coverage and the annealing method it is clear the structure of the overlayer system is important. The fact that the dichroism is smaller in the as-deposited layers can be understood from the disordered nature of these layers, which will wash out any macroscopic effects. If the effect were indeed mainly of magnetic origin then the strong magneto-crystalline anisotropy forces of the rare earth would prevent the magnetic alignment of the overlayer moments. In case of a crystal field origin the disordered nature itself would be responsible for the decrease.

8.7 Conclusion

In this study of the Tb/Ni(110) system we show that x-ray dichroism measurements on submonolayer coverages of rare earth metals on ferromagnetic substances provides very useful information on the splitting of the ground state by magnetic and crystal field effects. We found linear dichroic effects exist even at room temperature, indicating the splittings are of the order of several hundred Kelvin. The effects are found to be strongly temperature and thickness dependent and are found to increase upon annealing the overlayers.

The data are analyzed in terms of the thermally dependent population of the exchange-split free-ion ground-state, assuming a two-magnetic-domain model. An alternative interpretation in which the ground-state splitting is due to axial crystalline fields found at the surface is discussed. With the present data no definite choice is possible between the models, although it is felt the necessary lifting of the atomic degeneracy of the substates $|M\rangle$ by axial crystal field components to an extend which gives dichroism at room temperature is unlikely to occur.

Of course, in a ferromagnetic material the splitting may actually be caused by a mixture of crystal field and exchange field interactions. This could be the reason for the observed deviation of the temperature dependence of the dichroism parameter from the free-ion model Brilluoin-like behaviour.

The present results have clearly to be augmented by further measurements. However, these first data on multilayers show the potential of the x-ray dichroism method.

Acknowledgements

We thank the Laboratoire pour l'Utilisation du Rayonnement Electromagnetique (LURE) technical and scientific staff for their friendly support, in particular Dominique Chandesris and Giorgio Rossi. Also we are grateful to L. Schreurs and J. Hermsen for preparing the Ni crystal, and to O. Paul for performing the MOKE measurements. This work was supported in part by the Netherlands Foundation for Chemical Research (SON), the Netherlands Organization for the Advancement of Research (NWO), and the Committee for the European Development of Science and Technology (CODEST) program.

Bibliography

[1] C.G. Barkla. Proc. Roy. Soc. London **77**, 392 (1920).

[2] B.T. Thole, G. van der Laan and G.A. Sawatzky. Phys. Rev. Lett. **55**, 2086 (1985).

[3] I.M. Ternov, V.V. Mikhailin and V.R. Khalilov. *Synchrotron Radiation and its applications.* (Harwood Academic Publishers, 1985).

[4] K.J. Kim. Nucl. Instr. Meth. **219**, 425 (1984).

[5] K.J. Kim. Nucl. Instr. Meth. **222**, 11 (1984).

[6] H. Onuki. Nucl. Instr. Meth. **A246**, 94 (1986).

[7] J. Goulon, P. Elleaume and D. Raoux. Nucl. Instr. Meth. **A254**, 192 (1987).

[8] H. Onuki, N. Saito and T. Saito. Appl. Phys. Lett. **52**, 173 (1988).

[9] S. Yamamoto, H. Kawata, H. Kitamura, M. Ando, N. Sakai and N.Shiotani. Phys. Rev. Lett. **23**, 2672 (1989).

[10] P. Elleaume. Synchr. Rad. News **1**, 21 (1988).

[11] D.M. Mills. Nucl. Instr. Meth. **A266**, 531 (1988).

[12] J.A. Golovchenko, B.M. Kincaid, R.A. Levesque, A.E. Meixner and D.R. Kaplan. Phys. Rev. Lett. **57**, 202 (1986).

[13] C. Kittel. *Introduction to Solid State Physics.* (Wiley, New York, 5th edition, 1976).

[14] K.O. Hodgson, B. Hedman and J.E. Penner-Hahn, Editors. *EXAFS and Near-Edge Phenomena*, volume III. (Springer Verlag, 1984). and references therein.

[15] J.J. Yeh and I. Lindau. Atomic Data and Nuclear Data Tables **32**, 1 (1985).

[16] M.O. Krause. J. Phys. Chem. Rev. Data **8**, 307 (1979).

[17] J.C. Fuggle and S.F. Alvarado. Phys. Rev. A **22**, 1615 (1980).

[18] B.T. Thole and G. van der Laan. Phys. Rev. A **38**, 1943 (1988).

[19] M. Grioni, J.B. Goedkoop. R. Schoorl, F.M.F de Groot, J.C. Fuggle, F.Schäfers, E.E.Koch, G.Rossi, J-M.Esteva and R.C. Karnatak. Phys. Rev. B **39**, 4886 (1989).

[20] E. Merzbacher. *Quantum Mechanics.* (John Wiley & Sons, New York, 2th edition, 1970).

[21] W. Speier, J.C. Fuggle, P. Durham, R. Zeller, R.J. Blake and P. Sterne. J. Phys. C **21**, 2621 (1988).

[22] W. Speier. Ph.D. thesis, University of Köln, 1987.

[23] R. Zeller. Z. Phys. B (1989). to be published.

[24] J.F. van Acker *et al.* . to be published.

[25] P.J.W. Weijs *et al.* . to be published.

[26] J. Zaanen, G.A. Sawatzky, J. Fink, W. Speier and J.C. Fuggle. Phys. Rev. B **32**, 4905 (1985).

[27] J. Sugar. Phys. Rev. A **6**, 1764 (1972).

[28] B.T. Thole, R.D. Cowan, G.A. Sawatzky, J. Fink and J.C Fuggle. Phys. Rev. B **31**, 6856 (1985).

[29] B.T. Thole, G. van der Laan, J.C.Fuggle, G.A. Sawatzky, R.C. Karnatak and J.-M.Esteva. Phys. Rev. B **32**, 5107 (1985).

[30] P.W. Anderson. Phys. Rev. **124**, 41 (1961).

[31] O. Gunnarsson and K. Schönhammer. Phys. Rev. B **28**, 4315 (1983).

[32] A. Kotani and T. Jo. J. de Physique Coll. **C8**, 915 (1986).

[33] Takeo Jo. J. Phys. Soc. Jpn. **58**, 1452 (1989).

[34] Takeo Jo and Shin Imada. J. Phys. Soc. Jpn. **58**, 1922 (1989).

[35] E.A. Stern, D.E. Sayers and F.W. Lyttle. Phys. Rev. Lett. **37**, 298 (1976).

[36] F.M.F. de Groot *et al.* . to be published.

[37] T.A. Smith, J.E. Penner-Hahn, M.A. Berding, S. Doniach and K.O. Hodgson. J. Am. Chem. Soc. **107**, 5945 (1985).

[38] J. Zaanen, C. Westra and G.A. Sawatzky. Phys. Rev. B **33**, 8060 (1986).

[39] F.A. Cotton. *Chemical Apllications of Group Theory.* (Wiley-Interscience, New York, 1971).

[40] P. Zeeman. *Research in Magneto-Optics.* (MacMillan and Co., London, 1913).

[41] H.A. Lorentz. *Collected Papers.* (M. Nijhoff, The Hague, 1934).

[42] P.J. Stephens. Adv. Chem. Phys. **35**, 197 (1976).

[43] H.J.W.M. Hoekstra. Ph.D. thesis, University of Groningen, 1984.

[44] Y.H. Wong, F.L. Starace, C.D. Pfeifer and W.M. Yen. Phys. Rev. B **9**, 3086 (1974).

[45] J.K. Howard. J. Vac. Sci. Technol. A **4**, 1 (1986).

[46] Proceedings of the Fourth Joint MMM—Intermag Conference, Vancouver, IEEE Trans. on Magn. **24** (1988), and references therein.

[47] J.L. Erskine and E.A. Stern. Phys. Rev. B **12**, 5016 (1975).

[48] J.L. Erskine. Physica **89B**, 83 (1977).

[49] H. Feil and C. Haas. Phys. Rev. Lett. **58**, 65 (1987).

[50] H. Feil. Ph.D. thesis, University of Groningen, 1988.

[51] H. Ebert, P. Strange and B.L. Gyorffy. Z. Phys. B **73**, 77 (1988).

[52] B.L. Henke, P. Lee, T.J. Tanaka, R.L. Shimabukuro and B.K. Fujikawa. Atomic Data and Nuclear Data Tables **27**, 1 (1982).

[53] A. Hojo, Y.H. Ohtsuki and S. Yanagawa. J. Phys. Soc. Japan **21**, 2082 (1966).

[54] R.W. James. *The Optical Principles of the Diffraction of X-rays.* (G. Bell and Sons, London, 1984).

[55] M. Hart. Phil. Mag. B **38**, 41 (1978).

[56] M. Hart and A.R.D. Rodrigues. Phil. Mag. B **40**, 149 (1979).

[57] D.H. Templeton and L.K. Templeton. Acta Cryst. **A36**, 237 (1979).

[58] D.H. Templeton and L.K. Templeton. Acta Cryst. **A38**, 62 (1982).

[59] D.H. Templeton and L.K. Templeton. Acta Cryst. **A41**. 133 (1985).

[60] M. Blume. J. Appl. Phys. **1985**, 3615 (1985).

[61] D.E. Moncton, D. Gibbs and J. Bohr. Nucl. Instr. Meth. **A246**, 839 (1986).

[62] D. Gibbs, D.R. Harshman, E.D. Isaacs, D B. McWhan, D. Mills and C. Vettier. Phys. Rev. Lett. **61**, 1241 (1988).

[63] M.J. Cooper, D. Laundy, D.A. Cardwell, R.S. Holt D.N. Timms and G. Clark. Phys. Rev. B **34**, 5984 (1986).

[64] D.M. Mills. Phys. Rev. B **36**, 6178 (1987).

[65] A. Brahmia, M.J. Cooper, D.N. Timms, S.P. Collins, P.P. Kane and D. Laundy. J. Phys. **1**, 3879 (1989).

[66] K.W.H. Stevens. Proc. Phys. Soc. **A265**, 209 (1952).

[67] M.T. Hutchings. Solid State Physics **33**, p. 277. (Academic Press, 1964).

[68] F. Allen and C. Bustamente, Editors. *Applications of Circularly Polarized Radiation using Synchrotron and Ordinary Sources.* (Plenum Press, New York, 1984).

[69] F. Antonangeli, M. Piacentini, R. Girlanda, G. Martino and E.S. Giuliano. Phys. Rev. B **32**, 6644 (1985).

[70] T.A. Smith, J.E. Penner-Hahn, K. Hodgson, M.A. Berding and S. Doniach. *EXAFS and Near-Edge Structure*, volume III, p. 58. (Springer Verlag, 1984).

[71] N. Kosugi, T. Yokoyama and H. Kuroda. *EXAFS and Near-Edge Structure*, volume III, p. 55. (Springer Verlag, 1984).

[72] J. Stöhr and R. Jaeger. Phys. Rev. B **26**, 4111 (1982).

[73] P.H. Citrin, J.E. Rowe and P. Eisenberger. Phys. Rev. B **28**, 2299 (1983).

[74] N. Nücker, H. Romberg, X.X. Xi, J. Fink, B. Gegenheimer and Z.X. Zhao. Phys. Rev. B **39**, 6619 (1989).

[75] A. Abragam and B. Bleaney. *Electron Paramagnetic Resonance of Transition Ions.* (Clarendon Press, Oxford, 1970).

[76] E. Keller and E.A. Stern. volume III of *EXFAS and Near-Edge Structure.* 1984).

[77] G. Schütz, W. Wagner, W. Wilhelm, P. Kienle, R. Zeller, R. Frahm and G. Materlik. Phys. Rev. Lett. **58**, 737 (1987).

[78] G. Schütz and R. Wienke. Proc. Int. Conf. on Nucl. Meth. in Magn., to be publ. in Hyp.Int. (1988).

[79] G. Schütz, M. Knülle, R. Wienke, W. Wilhelm, W. Wagner, P. Kienle and R. Frahm. Z. Phys. B **73**, 67 (1988).

[80] H. Ebert, B. Drittler, R.Zeller and G. Schütz. Sol. St. Comm. **69**, 485 (1989).

[81] U. Fano. Phys. Rev. **178**, 131 (1969).

[82] N.B. Delone and M.V. Fedorov. SovPUS **22**, 252 (1979).

[83] G. Schütz, R. Frahm, P. Mautner, R. Wienke, W. Wagner, W. Wilhelm and P. Kienle. Phys. Rev. Lett. **62**, 2620 (1989).

[84] Takeo Jo and Shin Imada. Proc. VUV9 Conf and Phys. Scr. (1989). to be published.

[85] P. Carra and M. Altarelli. to be published.

[86] This thesis, Chapter 3.

[87] J. Sugar. Phys. Rev. B **5**, 1785 (1972).

[88] J. Sugar, W.D. Brewer and G. Kalkowski adn G. Kaindl. Phys. Rev. A **32**, 2242 (1985).

[89] C. Bonelle, R.C. Karnatak and J. Sugar. Phys. Rev. A **9**, 1920 (1974).

[90] C. Bonelle, R.C. Karnatak and N. Spector. J. Phys. B **10**, 795 (1977).

[91] V.F. Demehkin. Sov. Phys.—Solid State **16**, 659 (1974).

[92] S.A. Yavna, V.L. Sukhorukov and V.F. Demehkin. Sov. Phys.—Solid State **26**, 1396 (1984).

[93] G. van der Laan, B.T. Thole, R.C. Karnatak G.A. Sawatzky, J.C.Fuggle, J.-M.Esteva and B.Lengeler. J. Phys. C. **19**, 817 (1986).

[94] J.C. Fuggle, F.U. Hillebrecht, J.M. Esteva, R.C. Karnatak, O. Gunnarsson and K. Schönhammer. Phys. Rev. B **27**, 4637 (1983).

[95] O. Gunnarsson and K. Schönhammer. J. Magn. Magn. Mater. **52**, 141 (1985).

[96] T. Jo and A. Kotani. J. Phys. Soc. Jpn. **55**, 22457 (1986).

[97] J. W. Allen, S.J. Oh, O. Gunnarsson, K. Schönhammer, M.P. Maple, M.S. Torikachvilli and I. Lindau. Adv. Phys. **35**, 275 (1986).

[98] A. Fujimori, K. Terakura, M. Taniguchi, S. Ogawa, S. Suga, M. Matoba and S. Anzai. Phys. Rev. B (1988).

[99] S. Imada and T. Jo. Proc. VUV9 Conf and Phys. Scr. to be published.

[100] J.B. Goedkoop, B.T. Thole, G. van der Laan, G.A. Sawatzky, F.M.F. de Groot and J.C. Fuggle. Phys. Rev. B **37**, 2086 (1988).

[101] R.D. Cowan. *The Theory of Atomic Spectra.* (University of California Press, Berkeley, 1981).

[102] E.U. Condon and G.H. Shortley. *The Theory of Atomic Spectra.* (University Press, Cambridge, 1935).

[103] 3-j symbols are related in a simple way to the more familiar Clebsch-Gordon coefficients. They derive their usefulness from the fact that they take implicitly care of summations over magnetic quantumnumbers.

[104] R.D. Cowan. J. Opt. Soc. America **58**, 808 (1968).

[105] H.W.de Wijn, A.M. van Diepen and K.H.J. Buschow. Phys. Stat. Sol. (b)**76**, 11 (1976).

[106] G. van der Laan, J.C. Fuggle, M.P. van Dijk, A.J. Burggraaf, J.-M. Esteva and R.C. Karnatak. J.Phys.Chem.Solids **47**, 413 (1986).

[107] N.W. Ashcroft and N.D. Mermin. *Solid State Physics.* (Saunders College, Philadelphia, 1976).

[108] M. Rotenberg, R. Bivins, N. Metropolis and J.K. Wootens. *The 3-j and 6-j Symbols.* (Technology Press, Cambridge, 1959).

[109] *Magnetic Properties of Rare Earth Metals.* Edited by R.J. Elliot. (Plenum Press, London, 1972).

[110] C.J. Balhausen. *Introduction to Ligand Field Theory.* (McGraw-Hill Book Company, New York, 1962).

[111] K.A. Gschneider Jr. and L. Eyring. volume 2 of *Handbook of the Physics and Chemistry of Rare Earths.* (North Holland Publishing Company, Amsterdam, 1979).

[112] H.A. Alperin, J.R. Cullen, A.E. Clark and E. Callen. Physica B **86–88**, 767 (1977).

[113] R. Hasegawa. *Glassy Metals: Magnetic, Chemical and Structural Properties.* (CRC Press, Boca Raton, 1983). and references therein.

[114] P. Kruit and F.H. Read. JPE **16**, 313 (1983).

[115] G. Beamson, H.Q. Porter and D.W. Turner. Nature **290**, 556 (1981).

[116] A.R. Mackintosh. Europhys. News **19**, 41 (1988).

[117] J. Feldhaus, F. Schäfers and W. Peatman. **733**, 24 (1986).

[118] M. Lemonnier, O.Collet, C. Depautex, J.-M. Esteva and D. Raoux. Nucl. Instr. Meth. **152**, 109 (1978).

[119] P. Thiry, unpublished.

[120] G. van der Laan and B.T. Thole. Nucl. Instr. Meth. **A263**, 515 (1988).

[121] Z. Hussain, E. Umbach, D.A. Shirley, J. Stöhr and J. Feldhaus. Nucl. Instr. Meth. **195**, 115 (1982).

[122] J. Korecki. Hyperfine Interactions **40**, 89 (1988).

[123] M.P. Seah, W.A. Dench, B. Gale and T.E. Groves. J. Phys. E.: Sci. Instrum. **21**, 351 (1988).

[124] E. Erbil, G.S. Cargill III, R. Frahm and R.F. Böhme. Phys. Rev. B **37**, 2450 (1988).

[125] E.J. McGuire. Phys. Rev. A **5**, 1043 (1972).

[126] M.O. Krause and J.H. Oliver. J.Phys.Chem.Ref.Data **8**, 329 (1979).

[127] M.L. Néel. Comptes Rendus **239**, 8 (1954).

[128] F. Bertaut and F. Forrat. Comptes Rendus Acad. Fr. **242**, 382 (1956).

[129] *Proc. Int. School of Physics E. Fermi*, volume LXX. Edited by A. Paoletti. (North-Holland Publ. Comp., Amsterdam, 1977).

[130] I. Veltrusky and V. Nekvasil. J. Phys. C: Solid St. Phys. **13**, 1685 (1980).

[131] G. Balestrino and S. Geller. J. Magn. Magn. Mat. **49**, 225 (1985).

[132] A. Budkowski, A. Szytula, D. Rodic, R. Duraj, J. Mayer, J. Sciesinski and V. Spasojevic. J. Magn. Magn. Mat. **78**, 226 (1989).

[133] S. Geller, H.J. Williams, R.C. Sherwood, J.P. Remeika and G.P. Espinosa. Phys. Rev. **131**, 1080 (1963).

[134] S. Geller, J.P. Remeika, R.C. Sherwood, H.J. Williams and G.P. Espinosa. Phys. Rev. **137**, A1034 (1965).

[135] G. van der Laan, B.T. Thole, G.A. Sawatzky, J.B. Goedkoop, J.C. Fuggle, J.-M. Esteva, R.C. Karnatak, J.P. Remeika and H.A. Dabkowska. Phys. Rev. B **34**, 6529 (1986).

[136] M.A. Gilleo. volume 2 of *Ferromagnetic Materials*, chapter 1. (North-Holland Publ. Comp., New York, 1980).

[137] R. Pappalardo and D.L. Wood. J. Chem. Phys. **33**, 1734 (1960).

[138] K.E. Wickersheim. Phys. Rev. **122**, 1376 (1961).

[139] W.P. Wolf. Proc. Int. Conf. Magn., 555 (1964).

[140] S. Geller. *Crystal and Static Magnetic Properties of Garnets*, volume LXX of *Proc. Int. School of Physics E. Fermi*, chapter 1. (North-Holland, Amsterdam, 1977).

[141] R.Coehoorn, unpublished.

[142] Proceedings of the Fourth Joint MMM—Intermag Conference, Vancouver, J. Appl. Phys. **64** (1988). and references therein.

[143] K.H.J. Buschow. *Rare Earth Compounds*, volume 1 of *Ferromagnetic Materials*, chapter 4. (North-Holland, New York, 1980).

[144] G. Martens, P. Rabe, G. Tolkiehn and A. Werner. Phys.Stat.Sol.(a) **55**, 105 (1979).

[145] J.M. Esteva, R.C. Karnatak and J.P. Connerade. J. Electr. Spectr. Rel. Phen. **31**, 1 (1983).

[146] G. van der Laan and B.T. Thole. J. Elec. Spec. **46**, 123 (1988).

[147] S.W. Kortboyer, J.B. Goedkoop, F.M.F. de Groot, M. Grioni, J.C. Fuggle and H. Petersen. Nucl. Instr. Meth. **A257**, 435 (1988).

[148] G. van der Laan, J.B. Goedkoop, J.C.Fuggle, J. Verhoeven M.P. Bruijn, M.J. van der Wiel, A.A. MacDowell, J.B.West and I.A.Munro. Nucl. Instr. Meth. **A255**, 592 (1987).

[149] H. Hoekstra et al. unpublished.

[150] J.C. Fuggle, F. Ulrich Hillebrecht, R. Zeller, Z. Zolnierek and P.A. Bennet. Phys. Rev. B **27**, 2145 (1982).

[151] B. Johansson and N. Martenson. Phys. Rev. B **21**, 4427 (1980).

[152] J. Fink, B. Scheerer Th. Müller-Heinzerling, W. Speier, F.U. Hillebrecht, J.C.Fuggle, J.Zaanen and G.A. Sawatzky. Phys. Rev. B **32**, 4899 (1985).

[153] R.M. Nix, R.W. Judd and R.M. Lambert. Surf. Sci. **202**, 59 (1988).

[154] R.M. Nix, R.W. Judd and R.M. Lambert. Surf. Sci. **203**, 307 (1988).

[155] R.M. Nix, R.W. Judd and R.M. Lambert. Surf. Sci. **215**, L316 (1989).

[156] J.N. Andersen, J. Onsgaard, A. Nilson, B. Eriksson, E. Zdansky and N. Martenson. Surf. Sci. **189/190**, 399 (1987).

[157] J.N. Andersen, J. Onsgaard, A. Nilson, B. Eriksson and N. Martenson. Surf. Sci. **202**, 183 (1988).

[158] I. Chorkendorff, J. Onsgaard, J. Schmidt-May and R. Nyholm. Surf. Sci. **160**, 587 (1985).

[159] I. Chorkendorff, J. Kofoed and J. Onsgaard. Surf. Sci. **152/153**, 749 (1985).

[160] J.N. Andersen, I. Chorkendorff, J. Onsgaard, J. Ghijsen, R.L. Johnson and F. Grey. Phys. Rev. B **37**, 4809 (1988).

[161] A. Nilsson, B. Eriksson, N. Maertensson, J.N. Andersen and J. Onsgaard. Phys. Rev. B **38**, 10357 (1988).

[162] R.M. Nix and R.M. Lambert. Surf. Sci. **186**, 163 (198).

[163] G.K. Wertheim, J.H. Wernick and G. Grecelius. Phys. Rev. B **18**, 875 (1978).

[164] D. Mauri and M. Landolt. Phys. Rev. Lett. **47**, 1322 (1981).

[165] A. Cerri, D. Mauri and M. Landolt. Phys. Rev. B **27**, 6526 (1983).

[166] M. Landolt, R. Allenspach and M. Taborelli. Surf. Sci. **178**, 311 (1986).

[167] C. Carbone and E. Kisker. Phys. Rev. B **36**, 1280 (1987).

[168] G. Busch, M. Campagna and H. Siegmann. *Electrons and Spectroscopy* Editted by D. Shirley (1972).

[169] R. Raue, H. Hopster and R. Clauberg. Phys. Rev. Lett. **50**, 1623 (1983).

[170] D. Weller, S.F. Alvarado, W. Gudat, K. Schröder and M. Campagna. Phys. Rev. Lett. **54**, 1555 (1985).

[171] D. Weller and S.F. Alvarado. J. Appl. Phys. **59**, 2908 (1986).

[172] C. Rau and H. Kuffner. J. Magn. Magn. Mat. **54/57**, 767 (1986).

[173] C. Rau, E. Umlauf and H. Kuffner. Nucl. Instr. and Meth. **B13**, 594 (1986).

[174] C. Rau and M. Robert. Phys. Rev. Lett. **58**, 2714 (1987).

[175] J. Sticht and J. Kübler. Sol. St. Commun. **53**, 529 (1985).

[176] B.C.H. Krutzen and F. Springelkamp. to be published.

[177] C. Rau and G. Xing. J. Vac. Sci. Technol. A **7**, 1889 (1989).

[178] I. Peschel and P. Fulde. Z. Phys. **259**, 145 (1973).

[179] Y.Y. Hsie and D.A. Pink. J. Phys. Chem. Solids **35**, 1481 (1974).

[180] S. Zajac. Physica B **86–88**, 51 (1977).

[181] R.E. Camley. Phys. Rev. B. **35**, 3608 (1987).

[182] D.L. Mills Phys. Rev. B. **39**, 12306 (1989).

[183] P. Fulde. *Crystal Fields*, volume 2 of *Handbook of the Physics and Chemistry of Rare Earths*, chapter 17. (North Holland Publishing Company, Amsterdam, 1979).

[184] S. Blügel. Ph.D. thesis, T.H. Aachen, 1988.

[185] S. Blügel, H. Akai, R. Zeller and P.H. Dederichs. Phys. Rev. B **35**, 3271 (1987).

[186] This thesis, Chapter 7.

[187] This thesis, Chapter 5.

[188] This thesis, Chapter 5.1.

[189] G. Rossi. Surf. Sci. Rep. **7**, 1 (1987).

[190] The spectra of Fig. 8.3 and 8.4 have been obtained with a slightly wider monochromator entrance slit, and hence have a lower experimental resolution compared to the spectra described in the rest of the paper.

[191] This thesis, Chapter 6.

[192] Since C_M depends only on $\langle M^2 \rangle$, the spectrum is not sensitive to the sign of the magnetization, so $[1\bar{1}1]$ and $[\hbar 11 \hbar 1]$ directions are equivalent for our purposes.

Abstract

Synchrotron radiation research is a rapidly growing branche of science. This is the result of the unique properties of synchrotron radiation, specifically its high degree of collimation, intensity and degree of polarization. The growth in the availability of synchrotron radiation has caused a breakthrough in x-ray spectroscopy that is comparable to the impact of the laser in the visible range.

The polarization characteristics of synchrotron radiation have up to know not been used extensively. Indeed, no clear idea of the magnitude of polarization effects in solids existed. Recently a number of pilot studies have proved that also in the x-ray range a whole scala of polarization effects exists that offer a spate of new spectroscopical, but also crystalographical experimental techniques.

The theme of this thesis is the investigation of the strong polarization dependende, or *dichroism*, that occur in the x-ray absorption spectra of rare earth materials. The rare earth elements distingiush themselves from the other elements through the behaviour of the 4f electrons which form the valence shell. This shell lies deep inside the atom, with the result that influences from the surrounding solid are well screened off by the outer electrons, so that even in the solid the 4f shell behaves very much like a in free atom or ion, and is almost completely spherically symmetric.

Perturbations from the solid environment however always disturb this symmetry to some extend, with the result that the absorption spectrum becomes dependent on the mutual orientation of the polarization vector of the radiation and the ion.

Earlier the existence of a strong magnetic x-ray dichroism (MXD) in the 3d→4f transitions of rare earths. In this thesis this work is extended, to a small degree theoretically but mainly experimentally.

Polarization dependent experiments with x-rays have some advantages over their visible range counterparts. The greater penetration length of x-rays allow one to investigate non-transparent materials. Also one can use

the electrons excited from the investigated material. The so-called *electron yield* methods for x-ray absorption measurements are to some extend surface sensitive. In combination with x-ray dichroism it is therefore possible to investigate magnetic and crystal field effects of submonolayer films.

In this thesis MXD is used in experiments on a bulk sample, terbium iron garnet, and on rare earth overlayers on a ferromagnetic surface, Ni(110). The results of the latter study show unequivocally the potential of the MXD technique.

The second theme of the thesis concerns experimental developments in soft x-ray spectroscopy. A description is given of a double crystal monochromator beamline that was constructed by our group at LURE, France. Results of the use of an organic crystal — multilayer combination in such a monochromator is described. Also a method is described for the characterization of the resolution of soft x-ray monochromators.

Finally a contribution to the characterization of the electron yield technique in the soft x-ray range is given.

Samenvatting

Synchrotronstraling onderzoek is een sterk groeiende tak van de natuurkunde. Dit is het gevolg van de unieke eigenschappen van synchrotronstraling, met name de gerichtheid van de bundel, die vergelijkbaar is met die van een laser, de intensiteit, en de hoge polarizatie graad. Het beschikbaar komen van een röntgen stralings bron met deze eigenschappen heeft een doorbraak teweeg gebracht in de röntgen spectroscopy die vergelijkbaar is met de komst van lasers in het zichtbare deel van het spectrum.

De polarizatie karakteristieken van synchrotron straling zijn echter tot nu toe nauwlijks benut, en er bestond weinig inzicht in de grootte van polarizatie effecten in het röntgen gebied. Inmiddels heeft een reeks van explorerende studies aangetoond dat ook in in dit gebied een scala van polarizatie effecten bestaat, die tal van nieuwe spectroscopische en ook kristallografische mogelijkheden bieden.

Het thema van dit proefschrift betreft het onderzoek van de sterke polarizatie afhankelijkheid, ofwel *dichroisme*, die optreedt in de röntgen absorptielijnen van zeldzame aard materialen. De zeldzame aard elementen onderscheiden zich van de overige elementen doordat de 4f electronen die de valentie schil vormen diep in het atoom liggen. Als gevolg daarvan worden de 4f electronen vrijwel geheel afgeschermd van de invloed van de omringende atomen, zodat ze zich zelfs in een vaste stof nagenoeg gedragen als de electronen in een vrij atoom, en een vrijwel bolsymmetrische ladingsverdeling hebben.

Verstoringen van buiten het atoom kunnen die bolsymmetry vervormen. Dit heeft tot resultaat dat het absorptie spectrum afhankelijk wordt van de onderlinge orientatie van het vervormde atoom en de polarizatie vector van de straling.

Eerder werd het bestaan voorspeld van een sterk magnetisch röntgen dichroisme (MXD) in de 3d→4f overgangen van zeldzame aarden. In dit proefschrift wordt gedeeltelijk theoretisch maar vooral experimenteel voortgebouwd op deze voorspellingen.

Polarizatie afhankelijke experimenten met röntgen straling hebben een aantal voordelen ten opzichte van zichtbaar licht experimenten. De grote penetratie van röntgen straling maakt het mogelijk niet-transparante materialen te onderzoeken. Ook kan gebruik gemaakt worden van de electronen die door de röntgen straling uit het onderzochte materiaal worden vrijgemaakt. De *electron yield* methoden voor röntgen spectroscopie zijn in zekere mate oppervlakte gevoelig. In combinatie met röntgen dichroisme is het daardoor mogelijk magnetische en kristalveld effecten te onderzoeken van sub-monolaag dikte films.

In dit proefschrift wordt MXD gebruikt in experimenten aan een bulkmateriaal, terbium ijzer granaat, en aan zeldzame aard overlagen op een ferromagnetisch oppervlak, Ni(110). De resultaten van het laatste experiment tonen duidelijk de mogelijkheden die de MXD techniek biedt voor de karakterizatie van de vaste stof effecten in zulke systemen.

Het tweede thema van het proefschrift behelst experimentele ontwikkelingen op het gebied van zachte röntgen monochromatoren. Er word een beschrijving gegeven van een dubbel-kristal monochromator die door onze groep werd opgebouwd in LURE, Frankrijk, en er worden resultaten beschreven over het gebruik van een nieuw type monochromator, waarbij een stralingsgevoelig organisch kristal wordt beschermd door een metallische multilaag spiegel. Verder wordt een methode beschreven voor de karakterisering van de resolutie van dergelijke monochromatoren.

Tenslotte wordt een bijdrage geleverd tot de kwantificatie de electron yield techniek in het zachte röntgen gebied.

Publications

The material in this thesis is in part published in the following papers:

G. van der Laan, B.T. Thole, G.A. Sawatzky, J.B. Goedkoop, J.C. Fuggle,
J-M. Esteva, R.C. Karnatak, J.P. Remeika and H.A. Dabkowska,
Experimental proof of Magnetic X-ray Dichroism,
Phys. Rev. B**34**, 6529 (1986).

M.P. Bruijn, J. Verhoeven, M.J. van der Wiel, G. van der Laan,
J.B. Goedkoop, J C. Fuggle and A.A. MacDowell,
Characterization of multilayers using 200 900 eV synchrotron radiation,
Nucl. Instr. Meth. A**253**, 135 (1986).

G. van der Laan, J.B. Goedkoop, J.C. Fuggle, M.P. Bruijn, J. Verhoeven,
M.J. van der Wiel, A.A. MacDowell, J.B. West and I.H. Munro,
Soft x-ray monochromatization using a multilayer-single crystal combination,
Nucl. Instr. Meth. A**255** 592 (1987).

G. van der Laan, J.B. Goedkoop, A.A. MacDowell,
A high resolution soft x-ray monochromator for synchrotron radiation based on a multilayer/crystal combination,
J. Phys. E**20** 1496 (1987).

H. van Brug, M.J. van der Wiel, R. van der Pol, J. Verhoeven,
G. van der Laan and J.B. Goedkoop,
Reflection extended x-ray absorption fine-structure measurements on Ni/C and Ni_xSi_y/C
multilayered reflection coatings,
J. Vac. Sci. Technol. A**6** 2182 (1988).

M. Grioni, F. Schäfers, J.B. Goedkoop, J.C. Fuggle, J.L. Wood and
H. van Brug,
Tests of multilayers based soft x-ray monochromators for synchrotron radiation,
J. Phys. C**9** 91 (1987).

M. Grioni, J.C. Fuggle, P.J.W. Weijs, J.B. Goedkoop, G. Rossi, F. Schäfers, J. Fink and N. Nücker,
High energy spectroscopies of Cu compounds including the new superconductors,
J. Phys. C**9** 1189 (1987).

J.B. Goedkoop, B.T. Thole, G. van der Laan, G.A. Sawatzky, F.M.F. de Groot and J.C. Fuggle,
Calculations of magnetic x-ray dichroism in the 3d absorption spectra of rare earth compounds,
Phys. Rev. B**37** 2086 (1988).

J.B. Goedkoop, J.C. Fuggle, B.T. Thole, G. van der Laan and G.A. Sawatzky,
Circularly polarization filters in the soft x-ray range,
Nucl. Instr. Meth. A**273**, 429 (1988).

J.B. Goedkoop, J.C. Fuggle, B.T. Thole, G. van der Laan and G.A. Sawatzky.
Magnetic x-ray dichroism of rare earth materials,
J. Appl. Phys. **64** 5595 (1988).

M. Grioni, J.B. Goedkoop, R. Schoorl, F.M.F. de Groot, J.C. Fuggle, F. Schäfers, E.E. Koch, G. Rossi, J.-M. Esteva and R.C. Karnatak
Studies of copper valancies with Cu L_3 x-ray absorption spectroscopy,
Phys. Rev. Bbf 39 1541 (1988).

S.W. Kortboyer, J.B. Goedkoop, F.M.F. de Groot, M. Grioni, J.C. Fuggle and H. Petersen,
Experimental resolution in soft x-ray monochromators,
Nucl. Instr. Meth. A**257** 435 (1988).

Chapters 7 and 8 will be submitted for publication.

Acknowledgements

It is of course impossible to thank the many people from whom I learned so much during the last four years. Nevertheless an attempt is in place here.

John Fuggle was a bit of a gamble for me from the beginning since I was his first PhD student in Nijmegen. Things turned out quite well, especially on the sides of international contacts, opportunities and wines. Also I learned from him the meaning of basic physical terms like self energy, excited states, order and chaos.

George Sawatzky has been the remote control for this work. From him and his group the theoretical input originated and whenever I turned myself to that Northern source I returned lavished and refreshed.

Marco Grioni deserves a special word. He and his wife Anna formed more than a 'pied a terre' in Paris during the work at the synchrotron, giving me an altogether new definition of the word hospitality. Also I am indebted to Marco for teaching me much about surface sience and the attitude a synchrotron worker should have: you can always go on.

Furthermore I thank:

Gerrit van der Laan who acted as my mentor for the first part of this work and introduced me to the technique of x-ray absorption.

Wolfgang Speier for the pleasure of working with him during the 'Silicides Project'.

My colleagues, Hans van Acker, Harry Borsje, Pieter Weijs, Frank de Groot, Ronald Kappert and Wiesiek Szweryn, for discussions, practical assistance and taking turns in driving apparatus to Paris.

Chris Timmer and the Electronics department for the enjoyable cooperation during the design and realisation of the monochromator steering electronics.

The LURE staff for their support of the experiment and for making me feel very much at home at LURE during the long stays there.

The administration departments of the Nijmegen and Groningen universities for their patience in dealing with the extra paperwork an international research project brings about.

Finally, all other persons who have contributed to the realization of this work.

Curriculum Vitae

Ik ben geboren op 28 februari 1959 in Oslo, Noorwegen. Mijn scholing tot en met het eind-examen Atheneum-B in juni 1977 heb ik genoten in Bergen, NH, en Alkmaar.

In datzelfde jaar ben ik begonnen met de studie experimentele natuurkunde aan de Rijksuniversiteit Utrecht. Na het behalen van het kandidaats-examen met bijvak Scheikunde in juni 1981 heb ik bij de vakgroep Vaste Stof Fysica van de RUU gewerkt aan de opbouw van een Fabry-Perot interferrometer opstelling. Daarna heb ik een jaar onderzoek gedaan bij het Rijksinstituut voor Volksgezondheid en Milieuhygiëne naar de lichtabsorptie door atmosferisch stof (aerosolen), voor de meting waarvan een gecombineerde lange-weg transmissie/verstrooiings opstelling werd opgebouwd.

Het doctoraal-examen Experimentele Natuurkunde met bijvakken Vaste Stof Fysica en Informatica werd afgelegd in juni 1985.

De afgelopen vier jaar heb ik onder leiding van Prof.Dr. J.C. Fuggle en Prof. Dr. G.A. Sawatzky gewerkt als wetenschappelijk medewerker op een door de Stichting Scheikundig Onderzoek der Materie gefinancieerd röntgen absorptie onderzoeksproject. Ten behoeve van dit project verbleef ik in het totaal ongeveer een jaar bij synchrotron-straling centra in Engeland, Duitsland en Frankrijk. Van de tijdens die verblijven behaalde onderzoeksresultaten word in dit proefschrift verslag gedaan.